2019

Investigation of the Flow Field and Associated Heat Transfer within an Asymmetrical Leading Edge Jet Impingement Array

Jorge Torres
University of Central Florida

INVESTIGATION OF THE FLOW FIELD AND ASSOCIATED HEAT TRANSFER WITHIN AN ASYMMETRICIAL LEADING EDGE JET IMPINGEMENT ARRAY

by

JORGE S. TORRES
BS Aerospace Engineering, University of Central Florida, 2017

A thesis submitted in partial fulfillment of the requirements
for the degree of Master's of Science in Aerospace Engineering
in the Department of Mechanical and Aerospace Engineering,
in the College of Engineering and Computer Science
at the University of Central Florida
Orlando, Florida

Summer Term
2019

ABSTRACT

This thesis investigates the turbulent flow features present in asymmetrical leading edge jet impingement and their effects from a fluid and heat transfer prospective using both numerical and experimental techniques. The jet-centerline plane flow field was quantified experimentally through the non-intrusive experimental method of Particle Image Velocimetry (PIV), while an area average heat transfer was acquired via a traditional copper block method. The numerical element served to investigate how well the Reynolds Averaged Navier-Stokes (RANS) k-ω SST turbulence model predicts the flow field and heat transfer within the leading edge and further investigate the results outside of the experimental scope.

Two different geometries, varied by H/d, were investigated at various Reynolds numbers ranging from 20,000 to 80,000. The geometry consisted of an array of 9 identical jets impinging on a leading edge of diameter D/d = 2, with an asymmetrical sidewall configuration to better represent the pressure side (PS) and suction side (SS) of a turbine blade.

Several vortices were identified within the flow field of the leading edge geometry. These vortices were larger for the H/d = 4 configuration but did not contribute to any increased or decreased heat transfer compared to that of the H/d = 2.7 configuration. The most influential aspect to both the flow field and heat transfer was the change in crossflow velocity between the two geometries. The smaller cross sectional area of the H/d = 2.7 configuration saw an increase in crossflow velocity and jet bending, tending to also decrease the heat transfer. The numerical results also reflected these results and in both area averaged heat transfer and localized heat transfer contour plots.

ACKNOWLEDGEMENTS

I would like to thank Dr. Kapat for giving me the opportunity to continue my academics under his advisement and mentoring. The amount of knowledge and experience I've acquired during my time in graduate school and the Siemens Energy Center (SEC) is both immeasurable and irreplaceable.

I'm forever grateful towards the SEC where I was able to conduct my research, and everyone there that helped me along the way. One key individual being Dr. Fernandez, who's been there through the whole journey and has helped at every turn. From helping out with hands on tasks, to teaching me the fundamentals of PIV and CFD, he was always there to help further my fundamental knowledge. Also, I would like to thank Dr. Rodriguez in the SEC who I received further guidance from throughout my research.

All of my fellow lab mates throughout the years who have made my time here the best it possibly could have been. The original IHT team when I first joined: Justin Hodges, Husam Zawati, Andrea Osorio. A special thanks to Andrea for sitting next to me all these years and putting up with all of my questions. Shinjan Ghosh and Alok Shah for their help and friendship. The Wednesday lunch crew: Akim Khlyapov, Patrick Tran, and Husam. And everyone else in the SEC I didn't mention previously: Luisana Calderon, Michael Elmore, Marcel Otto, Gaurav Gupta, Andres Curbelo, Akshay Khadse

Lastly I would like to thank my parents. For the unconditional support they've given me my whole life. Always pushing me to be the best version of myself, even when I wanted to take the easy way out and quit. I wouldn't be the person I am today without them.

TABLE OF CONTENTS

LIST OF FIGURES

LIST OF TABLES

LIST OF EQUATIONS

NOMENCLATURE

A: Area
C_p: Specific heat at constant pressure
D: Diameter of leading edge
E: Power
H Distance from orifice to stagnation point
M: Mach number
N: Number of samples
Nu: Nusselt number
P: Pressure
Pr: Prandlt number
PS: Pressure side
Q: Heat transfer
R Universal gas constant
Re: Reynolds number
S: Arc length
Sk: Stokes number
SS: Suction side
T: Temperature
TKE: Turbulent kinetic energy
U: Uncertainty
V: Velocity magnitude
V_y: Streamwise velocity component
V_z: Axial velocity component
V_{jet}: Mean jet velocity
$\dot{V}$: Volumetric flow rate
$\tilde{V}$: Voltage
Y Distance between jet centers
a: Speed of sound
d: Diameter of jet
d_p: diameter of particulate
h: Heat transfer coefficient
k: turbulent kinetic energy
k_f: Thermal conductivity of the fluid
l: Length of jet hole
$\dot{m}$: Mass flow rate
x: Lateral direction
y: Streamwise direction
z: Axial direction
ΔP: Differential pressure
Θ: Suction side inclination angle
Ω: Resistance

γ	Heat capacity ratio
ε:	Turbulent dissipation energy
η:	Efficiency
μ:	Dynamic viscosity
ϑ:	Kinematic viscosity
ρ:	Density
σ:	standard deviation
ω:	Specific dissipation
$\hat{\omega}$:	Angular velocity

\

CHAPTER 1: INTRODUCTION

1.1 - Gas Turbine Engines

Gas turbine engines have been one of the most crucial inventions of the 20th century. Utilized primarily in power generation and aircraft propulsion, their components allow for potential chemical energy to be extracted and converted to other forms of energy. In land-based power generation turbine engines this chemical energy is converted into electrical energy by rotating a shaft within. Propulsion gas turbine engines expel the hot gas out of the exhaust as kinetic energy.

Gas turbine engines operate through the Brayton cycle. For simplicity purposes the ideal Brayton cycle is considered below in Figure 1. In the first stage of the cycle, air is sucked into the compressor. The air is then compressed (1-2) and then ignited (2-3). In the final stage (3-4) the hot air expands and passes through the turbine section. This final stage is where the energy is converted into mechanical energy, and then electrical energy, in a power generation engine. The amount of energy converted is calculated by [Eq. 1], and the efficiency of the cycle is calculated by [Eq. 2]. The main limiting factor to the efficiency is the turbine inlet temperature, T_3. By increasing this temperature, the efficiency of gas turbine engines has rose significantly over the past few decades.

$$Q_{out} = c_p(T_4 - T_1) \quad [1]$$

$$\eta_{th,brayton} = 1 - \frac{T_4 - T_1}{T_3 - T_2} \quad [2]$$

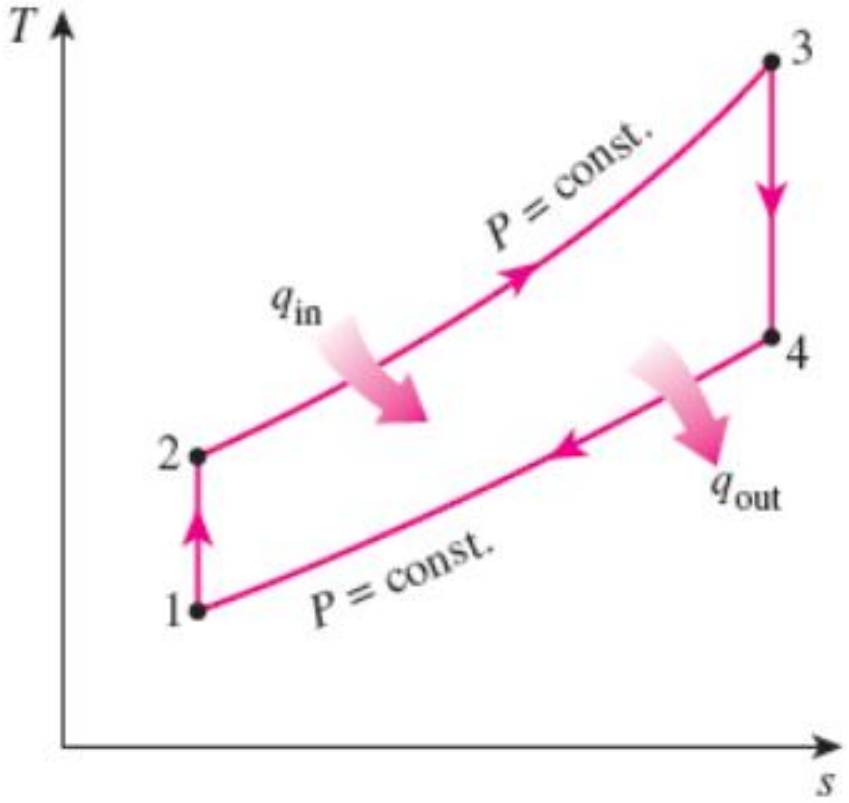

Figure 1: T-s diagram of the ideal Brayton cycle [Cengel, Boles, 2011]

The turbine inlet temperature has increased to the point that it has surpassed the melting temperature and safe operating temperature of the engine component materials. To circumvent this, technological advancements in the material used in the engine such as super alloys, thermal barrier coatings, and ceramic matrix composites have increased the safe operating temperature of the engine. Advanced convective cooling schemes within the engine have also allowed for the safe operating temperatures of the engine to increase. Figure 2 shows a typical diagram of the cooling paths within a turbine blade.

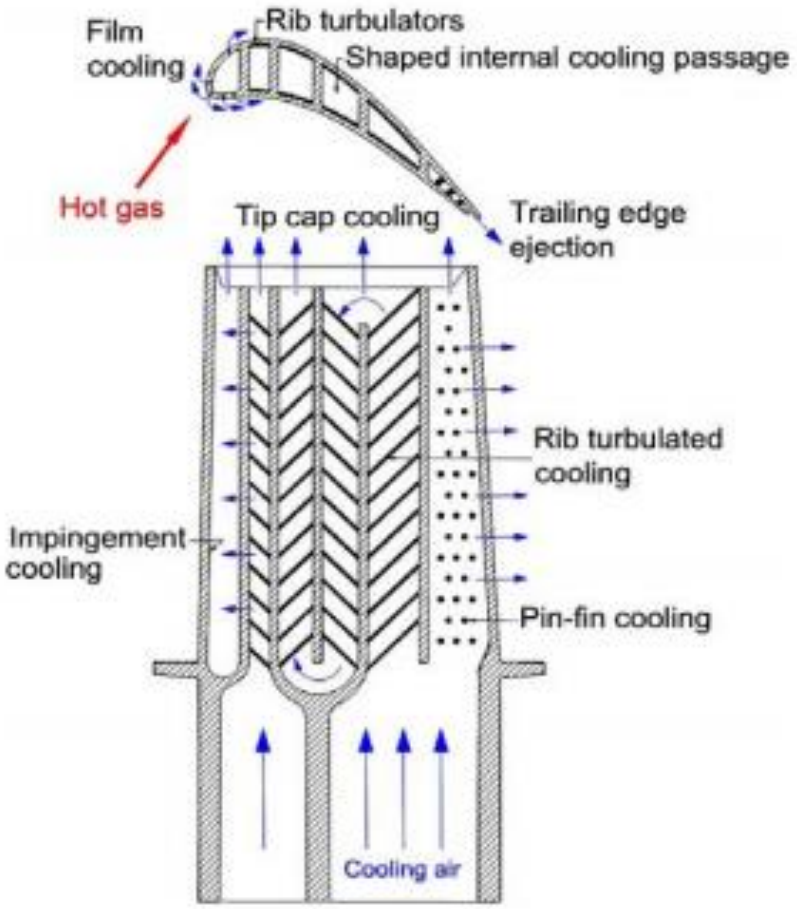

Figure 2: Typical cooling schematic of a gas turbine blade [Han, Wright, 2013]

1.2 - Gas Turbine Cooling

Convection cooling within the gas turbine blade is crucial to keep the blade from reaching its melting temperature. Cold air is taken from the compressor stages of the engine and diverted into the blade. However, there is a trade-off between how much air is diverted and the efficiency of the engine. Years of research in this field has been conducted to maximize heat removal while

minimizing the air required. Because of this, specialized cooling techniques are used in different areas of the blade.

As seen in Figure 2 above, the diverted air enters through the root of the blade and goes through serpentine passes. These serpentine passes typically have ribs or wedges on the walls to help enhance the heat transfer. The air then goes to either the trailing edge or leading edge of the blade. In the trailing edge of the blade pin fins are used to help support the thinner section of the blade while also increasing the wetted cooling area. Film cooling is used in the leading edge to expel the cooling air out of the blade, in doing so a thin layer of cool air forms between the hot gas and the external wall of the blade. Impingement cooling is used in multiple areas throughout the blade, but is very important in the leading edge due to its ability to remove large heat loads from stagnation point created from the rotating blade.

1.2.1 - Jet Impingement Cooling

Jet impingement cooling has been a staple in gas turbines for the past several decades. By reducing the cross sectional area in which the cooling air is passing via small holes, the velocity increases according to the conservation of mass. The high velocity air then exits the hole orifice as a jet, impinging on a target surface at the stagnation point. This stagnating jet is the premise of the efficient local cooling effect of impingement cooling.

$$\dot{m}_1 = \dot{m}_2 = \rho A V \quad [3]$$

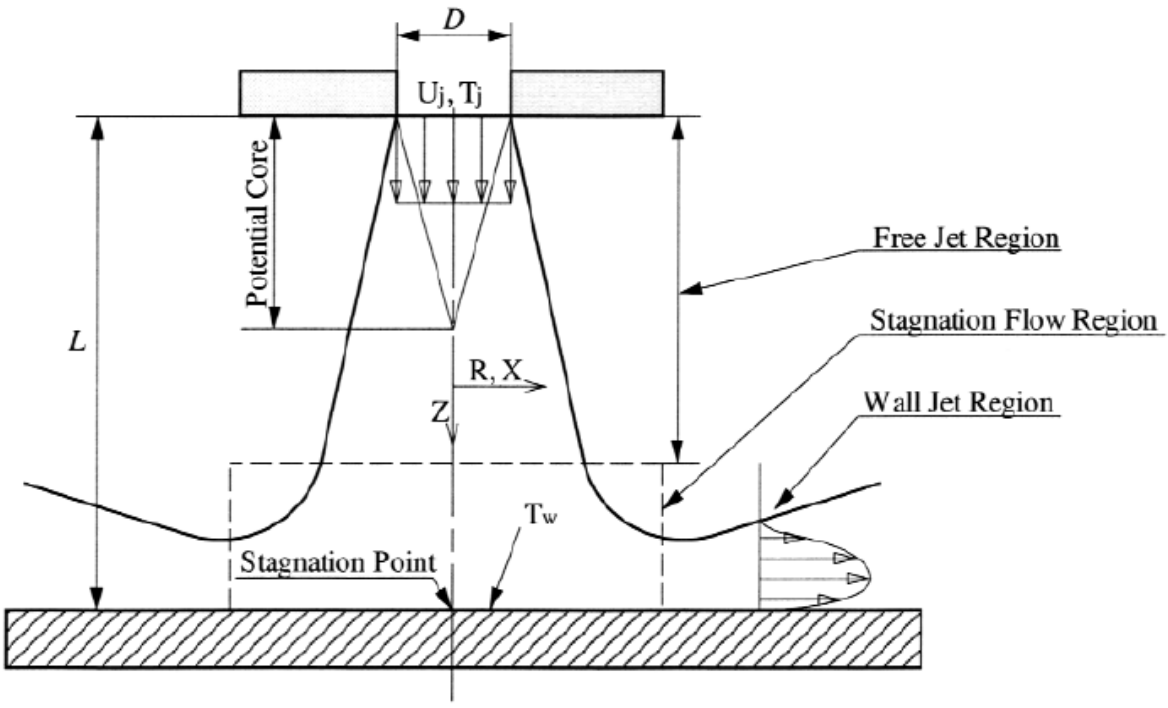

Figure 3: Anatomy of an impinging jet [Han, Goldstein, 2001]

A single impinging jet can be broken up into several distinct sections. Directly after exiting the orifice is the free jet region, consisting of the potential core and the fully developed region. The potential core is defined by where the average velocity of the jet at the orifice is maintained. The width of the potential core gradually diminishes due to a shear layer surrounding the jet. Once the potential core fades, the fully developed region forms and the axial velocity profile of the jet is assumed to have a normal distribution. The stagnation region is defined by the jet velocity decreasing, and radial velocity increasing as the jet approaches the target surface. The stagnation region transitions into the wall jet region consisting of predominantly radial velocity which forms a boundary layer along the target surface.

In the presence of an array of jets, added jet to jet interactions occur. The most prominent being jet bending due to crossflow in a narrow channel. This crossflow is the product of spent flow

from the upstream jets which increases further downstream with each subsequent jet. The amount of bending from the stagnation point increases with crossflow. This causes a detrimental effect to the stagnation point cooling as the impinging jet may fail to reach the target surface.

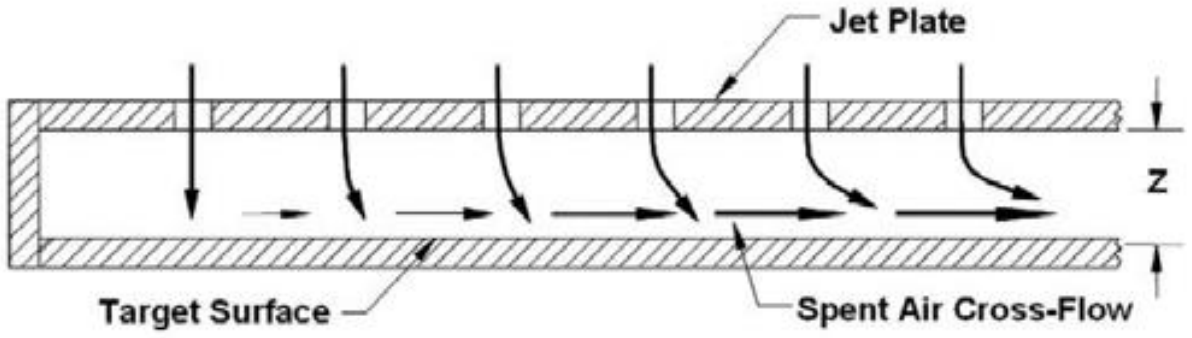

Figure 4: Cross section of inline array of jets in crossflow [Wang et al. 2015]

An impinging jet is defined through its non-dimensional parameters which allow the impinging jet to be scaled accordingly. All of these parameters are non-dimensionalized with respect to the jet hole diameter 'd'. Key geometrical parameters in all jet impingement geometries include the distance from the jet orifice to the stagnation point (H/d), length of the jet hole (l/d), and in an array of jets the jet to jet spacing (Y/d). The flow is characterized and non-dimensionalized by the Reynolds number of the jet [Eq. 4]. The cooling effectiveness of the jet can then be characterized by a correlation for area average Nusselt number as a function of these underlying non-dimensional parameters, such as [Eq. 5] where C, α, and β are constants dependent on the geometry.

$$Re = \frac{4\dot{m}}{\pi d \mu} \quad [4]$$

$$\mathrm{Nu}\left(\mathrm{Re}, \frac{\mathrm{H}}{\mathrm{d}}\right) = \mathrm{C} * \mathrm{Pr}^{0.33} * \mathrm{Re}^{\alpha} * \left(\frac{\mathrm{H}}{\mathrm{d}}\right)^{\beta} \quad [5]$$

In leading edge jet impingement two new geometrical parameters are introduced. The first being the diameter of the leading edge target surface. This diameter, denoted by 'D', is one of the most central parameters of the geometry of the leading edge and is non-dimensionalized by D/d. The last parameter is the angle at which the side walls sit from the jet centerline. Typically in narrow wall impingement both of the sidewalls are straight, but in leading edge impingement it is very common to find the sidewalls at an angle. This angle is measured from the jet centerline and is denoted by Θ.

1.3 - Computational Fluid Dynamics

Popularized in the 1980's, computational fluid dynamics (CFD) revolutionized the field of fluid dynamics. CFD allowed for numerical predictions of complete fluid domains and is useful when prototyping new designs, optimizing old designs, or when it's unrealistic to conduct a full experimental study.

Most CFD numerical calculations are based off a finite volume method (FVM) to evaluate the fluid flow field. By subdividing the fluid domain into a finite number of smaller control

volumes, or cells in a mesh, the discretized forms of the continuum transport equations can be applied at each control volume.

$$\frac{d}{dt}(\rho\chi\phi V)_0 + \sum_f[\rho\phi(v \cdot a - G)]_f = \sum_f(\Gamma\nabla\phi \cdot a)_f + (S_\phi V)_0 \quad [6]$$

While the FVM in conjunction with the transport equations allow for a majority of basic flow properties to be solved, the complexity in CFD comes when modelling turbulence. Turbulence is a natural phenomenon that is chaotic and highly irregular, making it hard to model deterministically. Because of this there are multiple turbulence models, all of which fulfill a different role.

The most common turbulence models are Reynolds Averaged Navier Stokes (RANS) models. These models tend to be robust with a relatively cheap computational cost. By applying Reynolds decomposition to the traditional Navier Stokes equations the new RANS equations are formed. The Reynolds decomposition process adds two new extra terms into the RANS equations: Reynolds stress and turbulent heat flux. Due to these new terms, the RANS equations lack closure. Modern techniques to achieve closure define additional variable characteristics of turbulent flows such as turbulent kinetic energy ‘k’, turbulent dissipation energy ‘ε’, specific dissipation ‘ω’, and other quantities. These quantities used in conjunction with one another lead to the popular turbulence models such as k-ε and k-ω.

1.4 - Particle Image Velocimetry

Particle image velocimetry is a method to investigate the fluid flow field akin to other non-intrusive techniques such as laser doppler velocimetry. The use of PIV became popular over similar methods due to its ability to collect data over an entire plane rather than a single point. This technique has a wide range of uses from experimental studies in wind tunnels, biomedical research, and to validate numerical results. PIV can be conducted in any optical medium ranging from gas to water.

The methods of PIV have evolved with time and technology to allow for more intense investigations to be done. At its base, steady PIV captures the in-plane flow statistics of the laser sheet; with the addition of a second camera Stereo PIV can capture the 3rd out-of-plane flow statistics component. These flow statistics are then averaged over time to spatially resolve the mean flow field in investigation. With the development of high frame rate cameras and continuous pulse lasers unsteady PIV became available. Unsteady PIV allows for the statistics of the flow field to be both spatially and temporally resolved and give a further insight into the flow's acceleration, fluid field development, and turbulence which was previously unobtainable with steady PIV.

CHAPTER 2: LITERATURE REVIEW

There are a multitude of cooling schemes employed in gas turbine blades. Pin fin cooling is employed in the trailing edge of the turbine blade, impingement cooling and serpentine passages are used all throughout the blade, and finally impingement and film cooling can be found in the leading edge. Han & Goldstein (2001) and Wright & Han (2013) each review in detail the different cooling schemes which can be found within a turbine blade.

2.1 - Leading Edge Cooling Review

Chupp et al (1969) were the first to form a correlation on leading edge impingement by varying the Reynolds number, H/d, D/d, and Y/d. In this study, they found that the Nusselt number increases with Reynolds number and H/d, but decreases in the presence of a larger leading edge radius. In the same year, Metzger, Yamashita, and Jenkins (1969) studied the effect of H/d and Y/d without crossflow and their data matched that of Chupp et al. Bunker and Metzger (1990) looked at the effect of D/d, H/d, and Y/d and leading edge sharpness on local heat transfer with and without film cooling. Adding on to what was previously known, their studies found that higher heat transfer occurs at a lower leading-edge sharpness.

Taslim et al (2001, 2003, 2009. 2011, 2013) studied leading edge impingement in the presence of crossflow extensively. In 2001 and 2003, Taslim et al studied the effects of surface roughness, and ribs. It was concluded from these studies that the increase in heat transfer due surface roughness and/or surface ribs was mainly due to the increase in wetted surface area. Taslim

et al (2009, 2011, & 2013) further studied leading edge impingement and the effect of extreme crossflow, racetrack holes, and different flow configurations. In all five of these studies it was noted that the crossflow produced by the upstream jets has a detrimental effect on the stagnation heat transfer of the downstream jets. This crossflow also increases the heat transfer on the side walls. Yang, Ren, Jiang, Ligrani (2014) identified the large effects that the Kelvin-Helmholtz vortices had on the heat transfer. Jordan, Writes, Crites (2012 & 2016) conducted local heat transfer experiments to find the effect of jet orifice sharpness and racetrack shaped holes, in which it was shown that racetrack holes perform better than circular holes of the same mass flow rate. Brakmann (2017) investigated the local heat transfer occurring in an array of impinging jets on an asymmetrical leading edge using TLC. This study also included film cooling holes and a numerical simulation to compare the experimental results. Low Reynolds numbers were tested along with various crossflow geometries.

2.2 - Flow Measurement/Visualization Review

Hossain, Fernandez, Kapat (2016) conducted an investigation into the flow physics of a narrow wall impingement array using PIV and various numerical models. A detailed look into the individual jet behavior concluded that the upstream jets behave as normal jets while the downstream jets experience increased jet bending due to the crossflow. The numerical investigation that accompanied this study compared the various turbulence models used to the experimental results. In the end the LES model best predicted the flow field at most locations.

Gau and Chung (1991) investigated the turbulent flow structures present in an impinging slot jet onto a convex curved surface and a concave curved surface. Their findings showed that when impinging upon a concave curved surface the width of the slot jet has a large effect on the flow structures. In their study, when the slot width was increased the vortex formation due to mixing with the ambient air occurs earlier when compared with a smaller slot width. While there were vortices structures in the free jet region, there were no three-dimensional vortices structures present at the stagnation point. Coronaro, Fleischer, and Goldstein (1999) characterized the flow structures of an impinging circular jet onto a leading edge surface with smoke flow visualization techniques while varying D/d, H/d and Reynolds number independently. For all test there was a large amount of recirculation due to the geometry of the curved surface that destabilized the jet in the free jet region. As a result of this instability there were diminished vortices in the free jet region and the stagnation point of the jet oscillated in the radial direction along the target surface. The vortices on the surface were effected directly by the curvature of the target surface. As the D/d decreased the radial flow structures became more distinct. It was also noted that the flow structures along the surface in the axial direction oscillated on and off the surface.

A study by Choi et al (1991) quantitatively measured the flow characteristics of an impinging slot jet onto a semi-circular concave surface using laser doppler anemometry. The potential core, jet centerline velocity, and wall jet were characterized for various H/d's. The results showed that the larger H/d's maintained their centerline velocity longer while also developing the wall jets faster than the smaller H/d's. Using PIV to capture the full cross section of a leading edge impinging slot jet, Gilard and Brizzi (2005) found that the jet is semi-stable and the stagnation point oscillates between three positions. This semi-stable oscillation is caused by a 'dead fluid' region near surface of the leading edge where velocities are extremely low. The three positions of

the jet correspond to the center of the curved target surface and two position, one on each side of the curved surface, located radially away from the center of the curved surface. The first jet position creates a symmetrical flow field after impingement in which the flow splits and follows the curved target surface radially in both directions. For the second and third positions, the jet impinges higher radially on the curved surface and a majority of the jet flows along the target surface towards the bottom of the curved surface.

2.3 - CFD Review

Numerical studies have been done to identify which turbulence model produces the most accurate results in accordance with experimental results. Jia, Rokni, and Sunden (2002) compared four different turbulence models of a slot jet impinging on both flat and concave surfaces. In this study, their V2F model outperformed the k-ε model in strain dominated regions, while the k-ε model outperformed in shear dominated regions. A numerical study done by Ibraham et al (2005) used experimental results from Lee et al (1999) to determine which turbulence model works best for a single jet impinging on a concave surface. The k-ε model performed the worst and over predicted heat transfer away from the stagnation point. Liu, Feng, Song (2010) preformed an initial comparison between the k-ω, SST k-ω, RNG k-ε turbulence models, and experimental data (from Bunker and Metzger (1990)) to determine which model to use. Their results backed up that of Ibrahim et al (2005) in which the RNG k-ε model over predicts the heat transfer; the SST k-ω model was found to produce the closest results and used throughout the numerical study. Yang et

al (2014) found that an unsteady SST k-ω model predicted the best results for a leading edge impingement in crossflow over steady and half steady time models.

CHAPTER 3: PROBLEM DEFINITION

In today's society there is a growing demand for cheaper and cleaner energy. While renewable options, such as solar power and wind turbines, have advanced over the past decades they are currently too inefficient to meet the power demand of the world. Gas turbines have been, and remain, the primary method of power generation. Improvements have been made to make gas turbine engines more efficient and cleaner, the most prominent method being increasing the turbine stage inlet temperatures. These higher temperatures surpass the engine component's melting temperature and have required scientific studies and technological advancement to prevent engine failure. New materials such as super alloys and thermal barrier coatings allow the engine components to have higher melting temperatures; while convective cooling schemes inside of the turbine blades help remove heat from the material. One such cooling method is impingement cooling which allows for large localized heat load removal.

Impingement cooling produces many turbulent phenomena and flow structures which effect the cooling efficiency. These phenomena and structures complexity increase as the wetted geometry becomes more complex. A simple single impinging jet has unstable Kelvin-Helmholtz vortices, an array of in-line jets in crossflow may produce jet bending and horseshoe vortices downstream, and Taylor-Gortler vortices may be present due to a jet impinging onto a curved surface. Understanding how changes in these turbulent flow phenomena effect the heat transfer is key to further increasing the cooling efficiency of an impinging jet.

3.1 - Specific Problem

The leading edge of the turbine blade has a higher temperature with respect to the rest of the blade due to the stagnation point. Thus, impingement cooling is critical on the leading edge in order to remove the heat load. The typical geometry of a leading edge consists of an array of in-line jets impinging onto a curved surface in a narrow wall environment. Decades of experimental and numerical studies have been done to increase the cooling efficiency. Popular approaches have been to change geometrical parameters such as jet to jet spacing, radius of curvature, etc.

Although the cooling efficiency has been studied thoroughly, there have been a limited number of experimental studies carried out to understand the flow field within these leading edge cavities. Such information could give insight to how the flow field changes with respect to geometry, and further how the change in the flow field effects the heat transfer efficiency. With this, new geometries can be designed to take advantage of these flow field and associated phenomena to remove larger heat loads from the leading edge.

3.2 - Novelty

In literature, nearly all of the leading edge impingement geometries are symmetrical around the apex of the leading edge curvature. This thesis draws its novelty in that the geometry in question is asymmetrical and closer represents that of a turbine blade leading edge currently in an operational gas turbine. This study also aims to experimentally quantify the flow field within the leading edge with PIV, which is also absent in literature.

3.3 - Approach

Planar PIV is used to visualize and understand the flow field along the jet centerline plane within the leading-edge. The results from this experiment is used to generate in-plane velocity contours. One dimensional slices of the contours along the plane are taken to plot velocity components at various z/d and y/d locations. Through these methods, both qualitative and quantitative conclusions are drawn about the flow field. The underlying characteristics of the flow field and its structures can then be related to the heat transfer.

The conventional method of applying a constant heat flux to a wall was used to obtain an area averaged heat transfer coefficient. Copper blocks along the target surface and side walls were each individually heated by a thin foil heater and their temperature measured with thermocouples. Each jet was given an individual section of copper blocks so that a heat transfer coefficient was found per jet.

Lastly, a numerical CFD simulation using Star-CCM+ supports the previous two experimental results. The simulation models both aspects of the experimental testing and allows for validation and further investigation of the flow field and heat transfer. These further investigations includes but is not limited to: 3D renderings of the flow field which would have either been unobtainable or too rigorous through PIV, velocity components of various planes within the fluid domain, and contours of the local heat transfer occurring on the surface.

CHAPTER 4: PREPARATION

Past experimental studies on leading edge jet impingement have focused only on heat transfer or PIV. The coupling of the two is one of the novelty factor of this study, but is also what adds complications to the overall design process. PIV requires a clear optical surface for the laser and camera; the method of area averaged heat transfer used prevents this optical ability. Thus two different experimental rigs had to be designed for each experimental method. Further, to couple the data from the two experiments it's crucial that the geometry of the two rigs are comparable.

With the overall scope of the project previously explained and a brief introduction into jet impingement, this section will delve further into the design along with steps taken between the initial concept and the final results of the experiments.

4.1 - Parameters in this Study

In this study the main investigation is on the effect of changing the H/d on the flow structures and heat transfer. In order to isolate these effects, the H/d is the only geometrical parameter to change. The dimensional jet diameter is 15mm and is constant for all 9 jets, and the two H/d's tested were H/d = 2.7 and H/d = 4. These were chosen because the former can be compared with that of Brakmann (2017) and the latter is a common H/d found in both literature and in application. The remaining non-dimensional parameters were also chosen to match that of Brakmann (2017) so that a comparison may be made: l/d =2, Y/d = 4, D/d = 2, and $\Theta = 20^{\circ}$. Unlike Brakmann (2017), there are no film cooling holes present in this investigation.

The only independent flow parameter in this study is the Reynolds number and is varied between test cases. Both the average jet velocities and bulk crossflow velocities are dependent on the Reynolds number and increase/decrease accordingly.

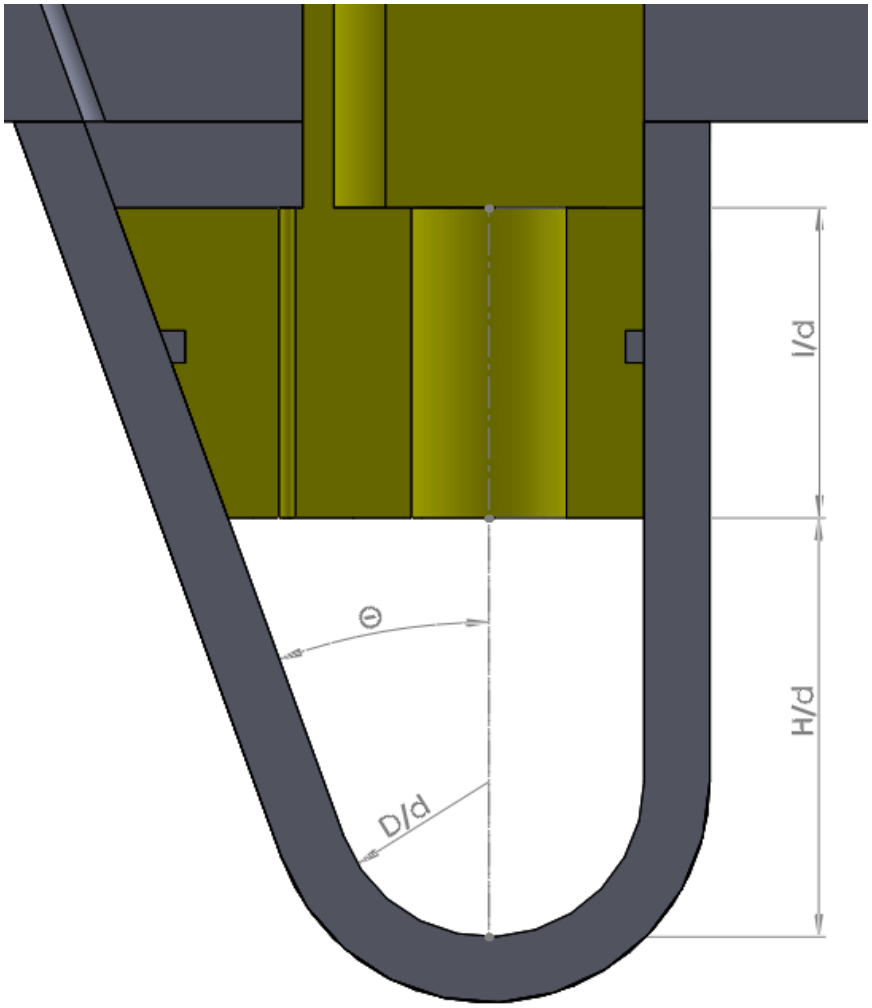

Figure 5: Identification of non-dimensional parameters

4.1.1 - Test Matrix

With the given parameters of this study above, there are a total of 8 different combinations of parameters to be tested. The parameters of each specific test are given in Table 1 below.

Table 1: Independent parameters investigated

H/d	Re	Y/d	D/d	l/d
2.7	20,000	4	2	2
2.7	40,000			
2.7	60,000			
2.7	80,000			
4	20,000			
4	40,000			
4	60,000			
4	80,000			

4.2 - Rig Design

Commercial licensed computer aided design (CAD) software was used to design each rig before manufacturing. This 3D CAD ensured that the separate components of each rig fit together properly, and that the final geometry of the two rigs were equivalent. The design of each rig will be discussed in this section.

Although the rigs were designed for different purposes a majority of the base design of the rigs were shared. The rigs are constrained by the H/d inlay, a top piece that holds the inlay, and the bellmouth inlet. The three of these components align the rig and help compress/seal it. To further constrain the rig, flanges located on the streamwise ends encompassed the outer profile of the test section to prevent outward bowing.

Of all the components of each rig only a single piece was shared between the two, the H/d inlay. This component can be considered the keystone of the rig design. Sharing this component ensures that the jet hole diameter, jet hole length, and overall test section length are the same between both rigs.

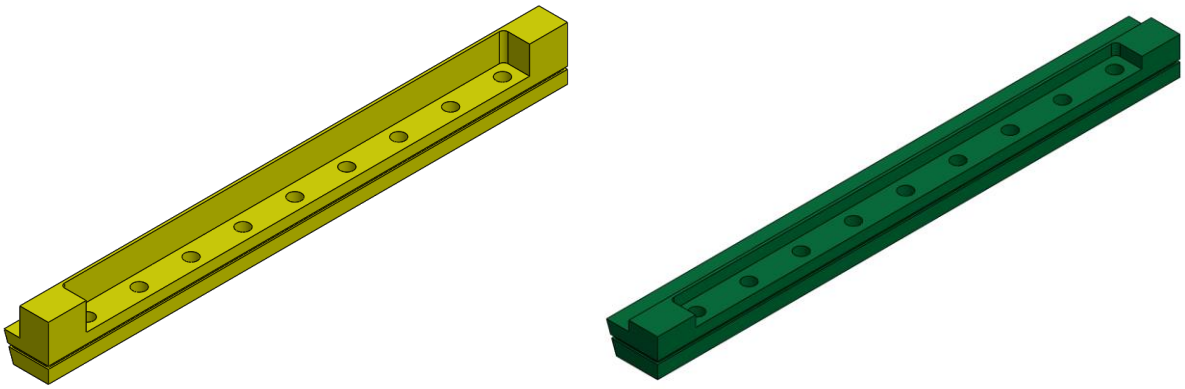

Figure 6: CAD of H/d inlays:
H/d = 2.7 (left) and H/d = 4 (right)

4.2.1 – Heat Transfer Rig

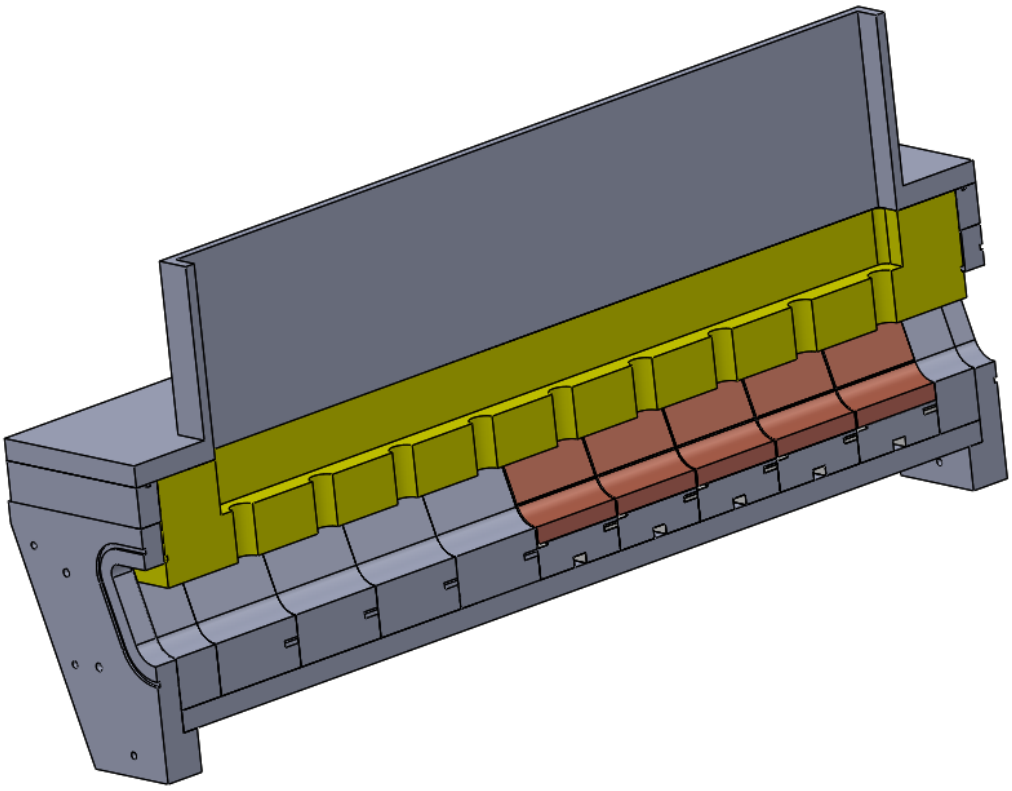

Figure 7: CAD of the heat transfer rig

The heat transfer rig had the more complex design of the two rigs. The target surface was split into 9 distinct spanwise sections, each 60mm long, corresponding with the 9 impinging jets. Each 60mm section was located directly below its respective jet. The 5 most upstream sections contained copper blocks to collect heat transfer data while the 4 most downstream sections were dummy sections made of acrylic. This configuration was chosen because the downstream flow

structures are washed out by the crossflow, leaving the primary area of investigation located at the upstream jets where vortices are present.

Each upstream copper spanwise section was separated into 5 copper blocks (to total 25 blocks in the experiment). These blocks consisted of the curved target surface, two blocks on the suction side, and two blocks on the pressure side. The copper blocks on the walls were split into two sections to accommodate the different target H/d heights. When the H/d = 4 the top most wall blocks contribute to the wetted surface; likewise when the H/d = 2.7 the top most blocks are covered. The dimensions of the copper blocks are found in Table 2 below.

Table 2: Copper block dimension

Copper Block	Wetted Surface Area	Thickness	Biot number
SS Top	0.00116 m^2	0.01 m	$1.16e^{-5}$
SS Bottom	0.00180 m^2	0.01 m	$1.80e^{-5}$
Curved	0.00247 m^2	0.01 m	$3.30e^{-5}$
PS Bottom	0.00138 m^2	0.01 m	$1.38e^{-5}$
PS Top	0.00109 m^2	0.01 m	$1.09e^{-5}$

The backside of the copper blocks (and sides where applicable) were insulated by Rohacell, minimizing any form of heat transfer from occurring other than convection along wetted surface. Rohacell was selected due to its low thermal conductivity of 0.03 W/mK. The copper blocks were also insulated between themselves by thin pieces of ABS plastic.

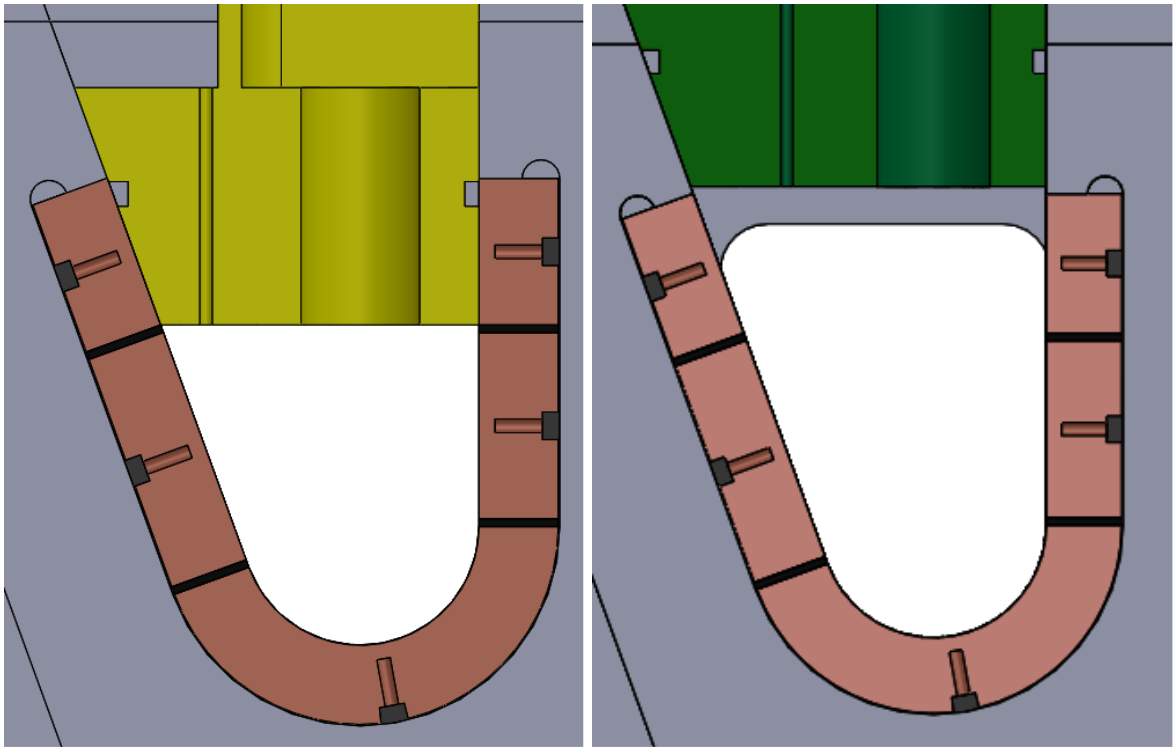

Figure 8: Cross section heat transfer rig at y/d = 0:
H/d = 2/7 (left), H/d = 4 (right)

Each copper block had its own custom sized heater. The heaters were applied to the copper block with a thin piece of double sided kapton tape to electrically isolate the heater and ensure that a good surface contact between the heater and the block was present.

Table 3: Heater properties

Heater	Heater Area	Resistance (room temperature)
SS Top	0.00116 m^2	138 Ω
SS Bottom	0.00180 m^2	40 Ω
Curved	0.00411 m^2	13.6 Ω
PS Bottom	0.00138 m^2	116 Ω
PS Top	0.00109 m^2	150 Ω

4.2.2 - PIV Rig

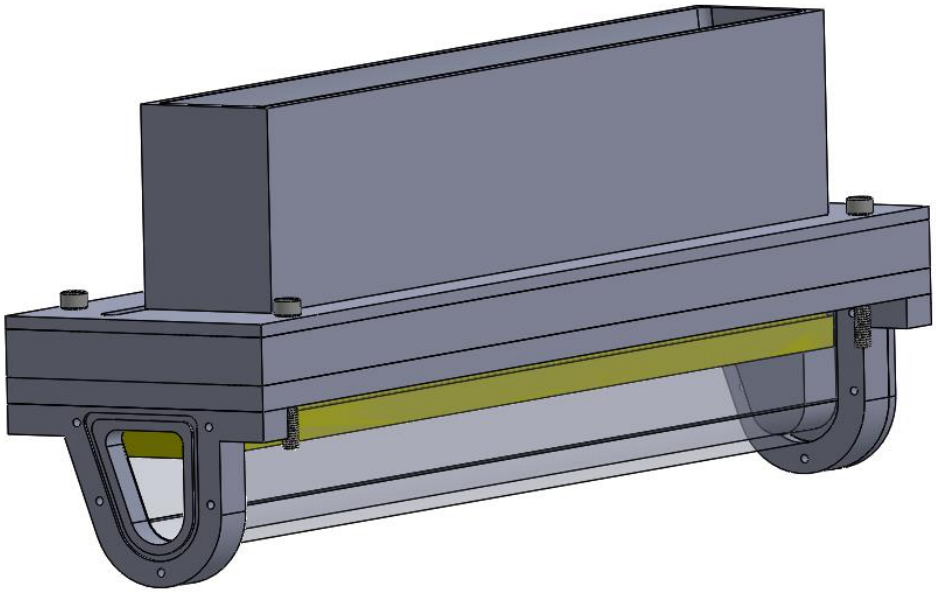

Figure 9: CAD of the PIV rig

The design of the PIV rig was based around the requirement for optical clarity of the target surface. To meet this requirement the target surface was made of one continuous clear acrylic sheet. This was achieved by heat treating the acrylic and then forming it in a mold. The top components and flanges then constrained the clear target surface from bowing.

4.3 - Flow Metering

To run the experiments a 12.5HP Balder Reliance industrial blower, which supplied a constant pressure drop of 35kPa, was used to supply flow through the test section. The pressure drop within the test section is controlled by a bypass valve upstream from the blower. A venturi located between the bypass valve and the test section measures the volumetric flow rate through the test section. The volumetric flow rate is calculated from a pressure differential (ΔP) within the venturi measured with an Omega HHP240 handheld manometer. This ΔP is then input into a calibration curve specific to that venturi, shown in Table 4, to get the volumetric flow rate.

Directly upstream of the venturi is a thermocouple to measure the temperature of the flow. The density of the flow is calculated using the measured temperature along with the current ambient pressure to solve the ideal gas law [Eq. 8]. This density is used to convert the volumetric flow rate to the mass flow rate [Eq. 9], which is then used to directly calculate the final Reynolds number [Eq. 10].

$$\dot{V} = fn(\Delta P) \quad [7]$$

$$\rho = \frac{P}{RT} \quad [8]$$

$$\dot{m} = \dot{V} \cdot \rho \quad [9]$$

$$Re = \frac{4\dot{m}}{\pi d \mu \cdot \#_{jets}} \quad [10]$$

Table 4: Venturis and their corresponding calibration curve

Reynolds Number	Venturi	Calibration Curve
20,000	2-20	$\dot{V} = -9E^{-6}x^2 + 0.0016x + 0.0183$
40,000	2-20	$\dot{V} = -9E^{-6}x^2 + 0.0016x + 0.0183$
60,000	2-65	$\dot{V} = -2E^{-8}x^4 + 4E^{-6}x^3 - 0.0002x^2 + 0.009x + 0.0333$
80,000	2-65	$\dot{V} = -2E^{-8}x^4 + 4E^{-6}x^3 - 0.0002x^2 + 0.009x + 0.0333$

4.3.1 Uncertainty Reynolds Number

To quantify the uncertainty for the experimental Reynolds number, the method of partial derivatives has been conducted. The final equation for Reynolds number [Eq. 10] was broken down to its most basic quantities and the partial derivatives of [Eq. 10] with respect to each base quantity was taken. The uncertainty in the measurement of the base quantities were factored in and [Eq. 11] was used to find the total uncertainty of the experiment. Figure 10 shows the error propagation tree used in the quantification of the total Reynolds number uncertainty.

$$U_\beta = \sqrt{\sum_{j=1}^{n} \left(\frac{\partial \beta}{\partial x_j} U_{x_j} \right)^2} \qquad [11]$$

The final uncertainty value for the Reynolds number was 3.18%. The major contributing factor in this was the mass flow rate, and more specifically the volumetric flow rate taken from the

venturi. The uncertainty associated with the venturi is 2.5%, while the uncertainty associated with the density is 0.38%.

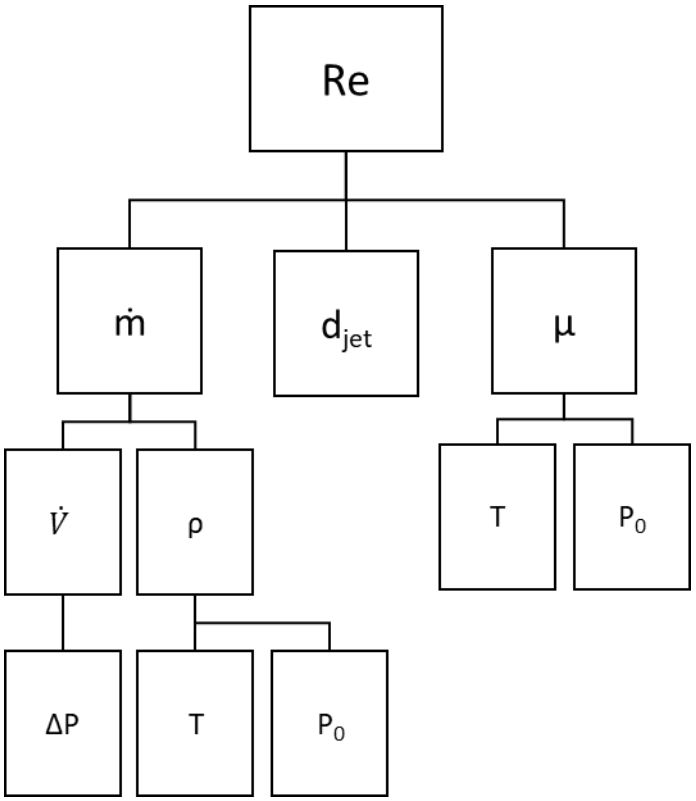

Figure 10: Reynolds number uncertainty propagation tree

4.4 - Pressure Test

The final step before taking experimental data was to ensure that the geometries of the two experimental rigs were similar so that their respective data can be confidently coupled together. To compare the two rigs a brief pressure drop experiment was conducted. A total of 18 pressure taps were placed along the bottom of the H/d inlays to measure the pressure at multiple streamwise points within the leading edge test section.

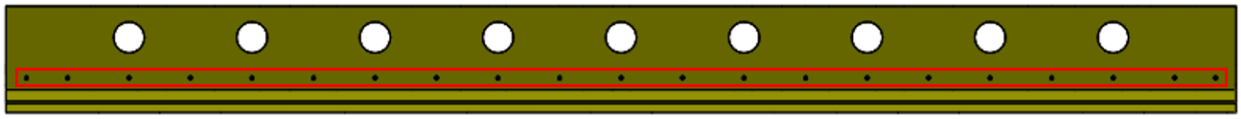

Figure 11: Pressure tap locations along the bottom of the H/d inlay

4.4.1 - Methodology

The diameter of each pressure tap was 1/32” and were placed 0.03m away from each other spanwise along the H/d inlay, and 0.0345m away from the perpendicular wall. The pressure taps alternate on-jet/off-jet to capture the local effects of each jet.

To measure the pressure at all of the points along the H/d inlay a scani valve was used. The scani valve records the pressure at each port as a voltage which is later converted to a pressure via a calibration during post processing. The pressure at each of the 18 points was averaged for a minute to obtain an average pressure value. This was done for each of the 8 test cases for the PIV rig and the heat transfer rig (the heat transfer rig was unheated for these tests to better match the

conditions of the PIV rig). If the geometries of the two rigs are similar then the pressure drops across the channel should match.

The static pressure data was converted to velocity with the use of the isentropic relations [Eq. 13] and Mach number [Eq. 14]. This data was used to validate the experimental velocities found with numerical calculated velocities at each mass flow rate.

$$a = \sqrt{\gamma RT} \quad [12]$$

$$\frac{P}{P_0} = (1 - \frac{\gamma - 1}{2} M^2)^{\frac{-\gamma}{\gamma - 1}} \quad [13]$$

$$V = Ma \quad [14]$$

4.4.2 - Results

To ensure that the data obtained and calculated from the pressure drop tests were correct the velocity data was normalized by the expected average velocity of the jets at the test's respective Reynolds number. If done correctly, the plots should all collapse upon one another. Figure 12 shows the normalized velocity of the PIV pressure data at H/d = 2.7 and H/d = 4 respectively; both of these show the proper collapse expected from normalization and therefore give confidence in the results.

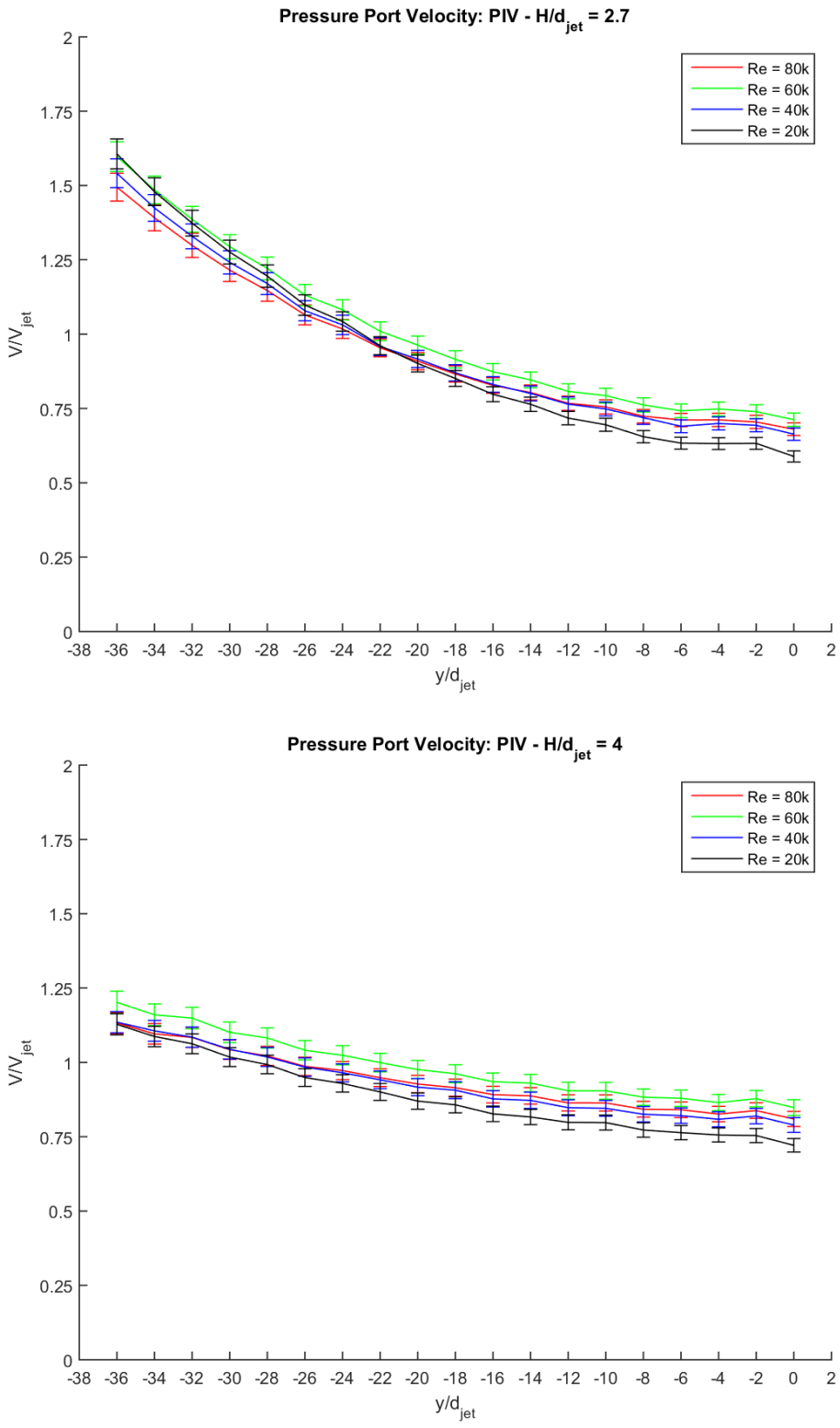

Figure 12: Normalized velocity at static pressure taps in PIV experiments: H/d = 2.7 (top), H/d = 4 (bottom)

These normalized plots also show the overall trend of each geometric configuration. The velocity increases (and pressure decreases) much more rapidly in the H/d= 2.7 configuration compared to the H/d = 4 configuration. This is expected as the cross sectional area is smaller and thus the bulk velocity is higher when the inlet mass flow rate is kept constant at a specific Reynolds number. The extent of this trend is better shown in Figure13 comparing the normalized velocity values of each configuration.

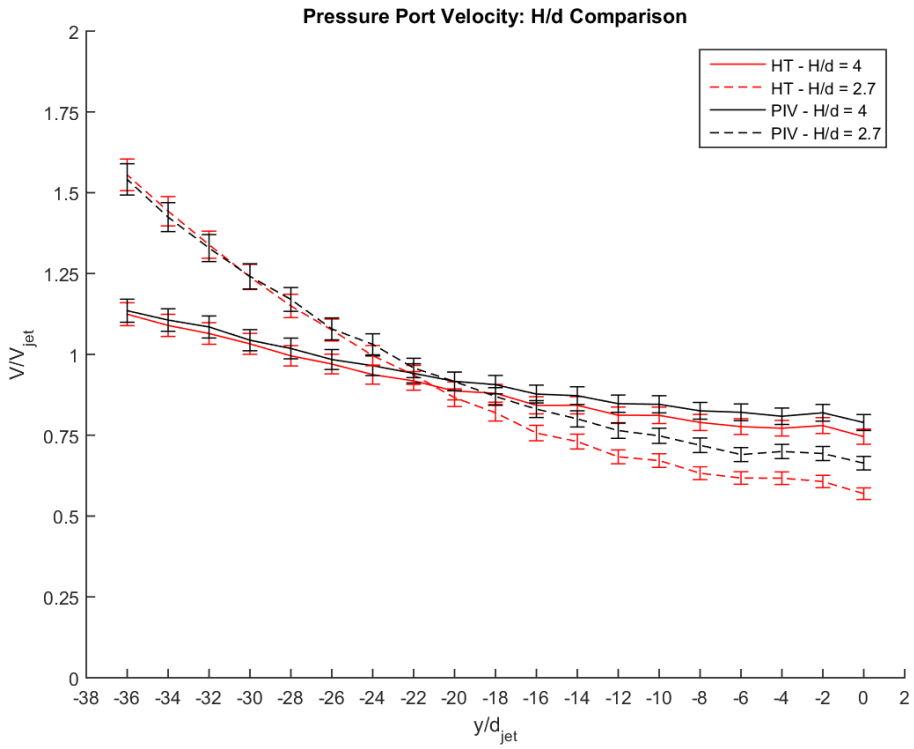

Figure 13: Comparison of normalized velocities between H/d = 4 and H/d = 2.7

Figure 13 also compares the pressure drop data between the PIV rig and the heat transfer rig. At both H/d's there is a slight difference in the upstream section (between y/d = 0 and y/d = -

20). This is attributed to the minor imperfections in the PIV fluid volume geometry caused in the manufacturing stage. Overall the trends and values between the two rigs are comparable and it can be assumed that the flow field within are indistinguishable.

4.4.3 Uncertainty Pressure Drop

The scani valve used to record the pressure drop induces an uncertainty of roughly 3% to the pressure value. There is also a small uncertainty associated with the orifice of the pressure tap on the flow side as quantified in [ASME PTC 19.2 (2010)]. The pitot tubes in this study best match the design in [ASME PTC 19.2 (2010)] that introduces 0.2% uncertainty, causing a total uncertainty in pressure drop of 3.2%

CHAPTER 5: HEAT TRANSFER

In any investigation to increase the efficiency of a gas turbine it's a staple to quantify the heat transfer characteristics. By collecting data on the heat transfer, a relationship between the geometrical parameters and the Nusselt number can be formed. The heat transfer data also reveals which areas of the leading-edge cavity have weaker heat removal.

5.1 - Methodology

To obtain an area average heat transfer coefficient the conventional method of applying a constant heat flux to a wall was used. The heated wall in this experiment consisted of copper blocks, with thin kapton heaters applied to the backside to supply a constant heat flux. Power was supplied to the heaters by variacs, and rheostats allowed for fine control over the exact power supplied to each heater.

Three thermocouples were placed 2mm from the surface of each block to approximate the temperature at the convecting surface. The biot numbers of each block were calculated (using heat transfer coefficient values from preliminary CFD) to ensure that the lumped capacitance model was valid and a constant temperature throughout the block could be assumed.

5.2 - Formulation

A 1D control volume of the copper block, shown in Figure 14, was generated to calculate the heat fluxes present. There are four heat fluxes: a generated heat flux from the heater, the convective heat flux leaving the block due to the impinging jet, a conductive heat flux through the surrounding materials, and lastly a radiative heat flux leaving the block. All of these fluxes must be accounted for and the sum of fluxes equal to zero when calculating the final heat transfer coefficient.

$$Q_{gen} = Q_{cond} + Q_{conv} + Q_{rad} \quad [15]$$

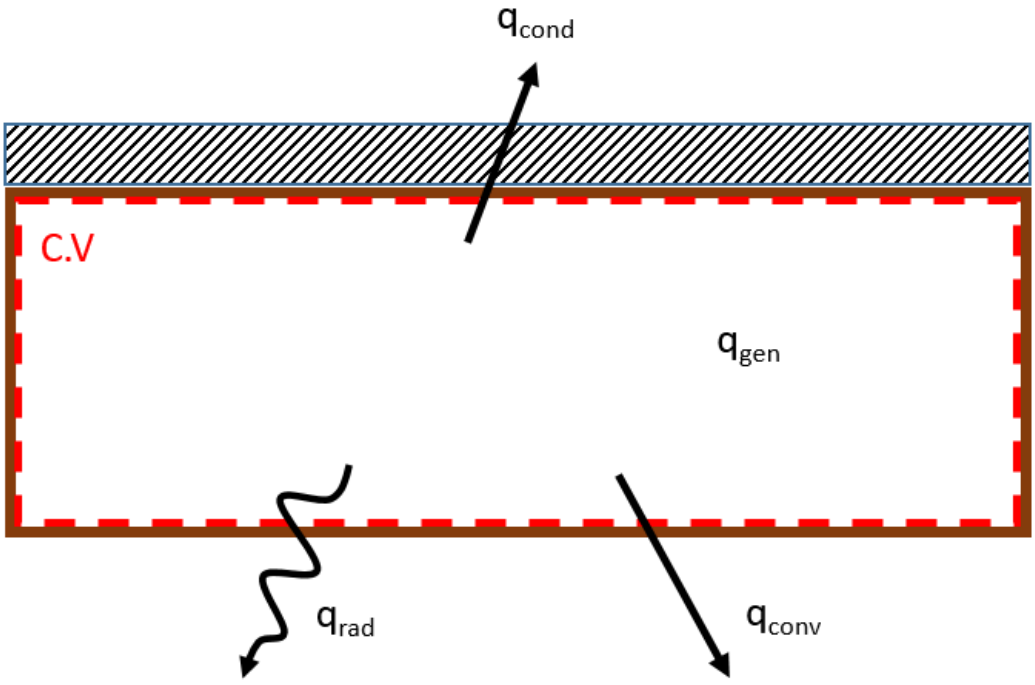

Figure 14: Control volume of the copper block

5.2.1 - Generated Heat Flux

The power being supplied to each heater can be calculated from Kirchhoff's Law [Eq. 16] with the known voltage and resistance of the circuit. With the known power of the heater the generated heat flux can be calculated using [Eq. 17]

$$E = \frac{\tilde{V}^2}{\Omega} \quad [16]$$

$$\mathrm{Q_{gen}} = \frac{\mathrm{E}}{\mathrm{A}} \quad [17]$$

5.2.2 - Conductive and Radiative Heat Fluxes

During the experiment there is a small portion of the generated heat flux that is not convected away into the flow. This portion of the generated heat flux is referred to as the heat leak (Q_{loss}) and consists of the radiative and conductive heat fluxes present. A preliminary heat leak experiment is conducted to determine the heat loss during the main experiments. [Eq. 15] can then be rearranged with [Eq. 19] substituted in to solve for the convective heat flux [Eq. 20].

$$Q_{loss} = \frac{E_{heatleak}}{A} \quad [18]$$

$$\mathrm{Q_{loss}} = \mathrm{Q_{cond}} + \mathrm{Q_{rad}} \quad [19]$$

$$\mathrm{Q_{conv}} = \mathrm{Q_{gen}} - \mathrm{Q_{loss}} \quad [20]$$

These heat leak tests are conducted for each H/d configuration. To eliminate any convective heat fluxes and ensure that the only present heat fluxes were radiative and conductive, the test section was filled with fiberglass insulation. Three tests were run per geometry at 40K, 50K, and 60K to create a linear trend between temperature and power, or in this case Q_{loss}. This linear trend equation was then used to interpolate the heat leak present at any temperature while testing.

5.2.3 - Convective Heat Flux

The heat transfer coefficient can be found by rearranging Newton's Law of cooling [Eq. 21] and using the known convective heat flux from [Eq. 20]; the heat transfer coefficient can then be non-dimensionalized using [Eq.22] to get Nusselt number. Inserting [Eq. 21] into [Eq. 22] yields the final equation used for non-dimensional Nusselt number [Eq. 23].

$$h = \frac{Q_{conv}}{A*\Delta T} \quad [21]$$

$$\mathrm{Nu} = \frac{\mathrm{h}*\mathrm{d_{jet}}}{\mathrm{k_f}} \quad [22]$$

$$\mathrm{Nu} = \frac{\mathrm{Q_{conv}}*\mathrm{d_{jet}}}{\mathrm{A}*\Delta\mathrm{T}*\mathrm{k_f}} \quad [23]$$

5.3 - Data Acquisition

All of the data was recorded using a Fluke data acquisition (DAQ) hardware and its accompanying software. The combination of this software and DAQ allow for all of the voltages and temperatures to be recorded simultaneous in real time. The DAQ itself samples at a frequency of 60 Hz and has an uncertainty of '0.004x + 0.25' for both the voltage and resistance.

The heaters are wired in parallel with the DAQ so that the voltage can be recorded while the test is running. A quick disconnect built into the circuitry allows for the heaters to be isolated from one another while still being in parallel with the DAQ so that the resistances of the heaters can be recorded. A simplified wiring diagram is shown in Figure 15.

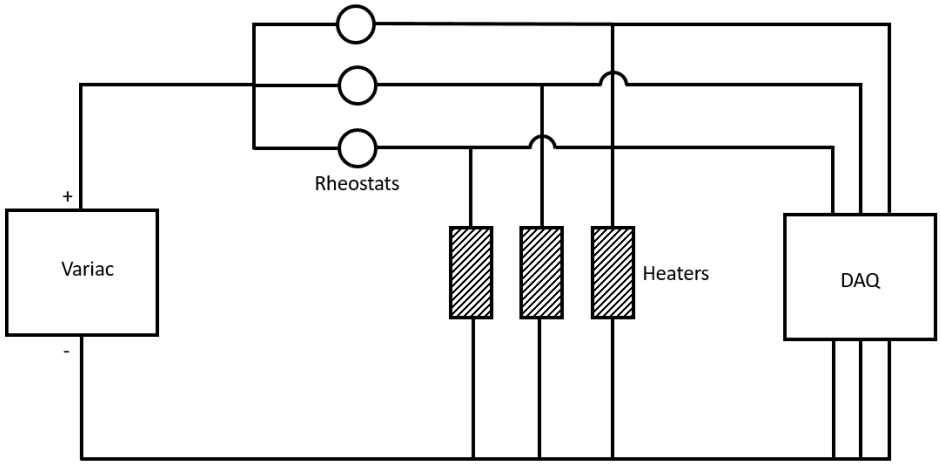

Figure 15: Simplified wiring diagram

T-type omega thermocouples were used to record the temperatures within the copper blocks and the temperature of the air within the rig. These thermocouples have a response time of 0.3s and an uncertainty of 1K.

5.4 - Testing Procedure

Before testing begins, a tare is applied using an RTD to ensure all the thermocouples have the same reference temperature. After the tare is complete the flow is turned on and adjusted until the target Reynolds number is reached. Power is supplied to the individual heaters so that the temperature of their respective copper blocks are 30K above the temperature of the jet, which is measured by two thermocouples located in the inlet plenum. Each copper block temperature is monitor and their heater voltage is adjusted accordingly until all 25 blocks have reached an isothermal steady state of within 0.6K of each other at the desired temperature. Once the blocks

reach steady state, the temperature and voltage of the copper blocks are recorded and averaged for 15 minutes. Meanwhile the Reynolds number is calculated one last time. After the temperature and voltages finish recording, the parallel circuit is broken at a quick disconnect and the resistances of each heater are taken.

5.5 - Uncertainty in Area Average Nusselt Number

The uncertainty for the experimental area average Nusselt number tests was quantified using the method of partial derivatives as before with Reynolds number. The final equation for Nusselt number [Eq. 23] was broken down to its most basic components and the uncertainty calculated accordingly. Figure 16 shows the uncertainty propagation tree used in the quantification of the total Nusselt number uncertainty.

The final uncertainty value for the Nusselt number was 8.64%. The major contributing factor in this was the ΔT between the copper block and the inlet, as each thermocouple has a base uncertainty of 1K. As this error propagates it results in an uncertainty in the dT of 6.34%. The second largest contribution of uncertainty comes from the Q_{conv} term and accounts for 1.97% uncertainty. These uncertainty values fall in line with those regularly seen in literature.

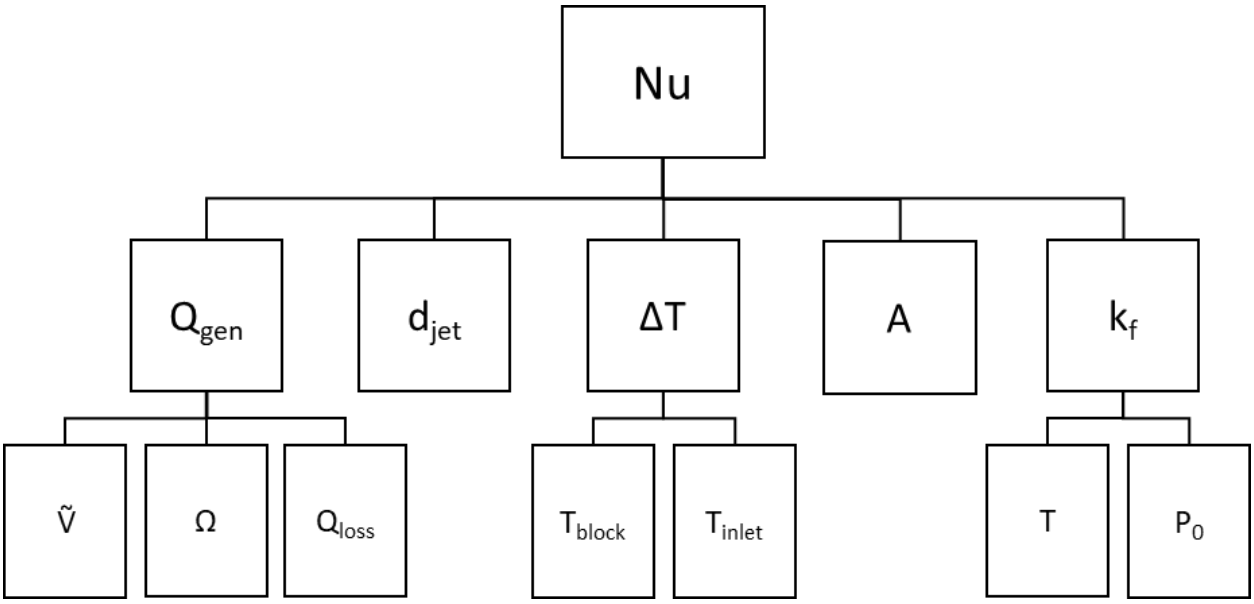

Figure 16: Nusselt number uncertainty propagation tree

CHAPTER 6: PARTICLE IMAGE VELOCIMETRY

The fundamentals of all convection driven heat transfer are derived from the interactions within the fluid flow. It's imperative to quantify these interactions to better understand how they affect localized heat transfer within the leading edge of a turbine blade. This section will discuss the methodology used to investigate the fluid flow field to identify vortices and flow structures.

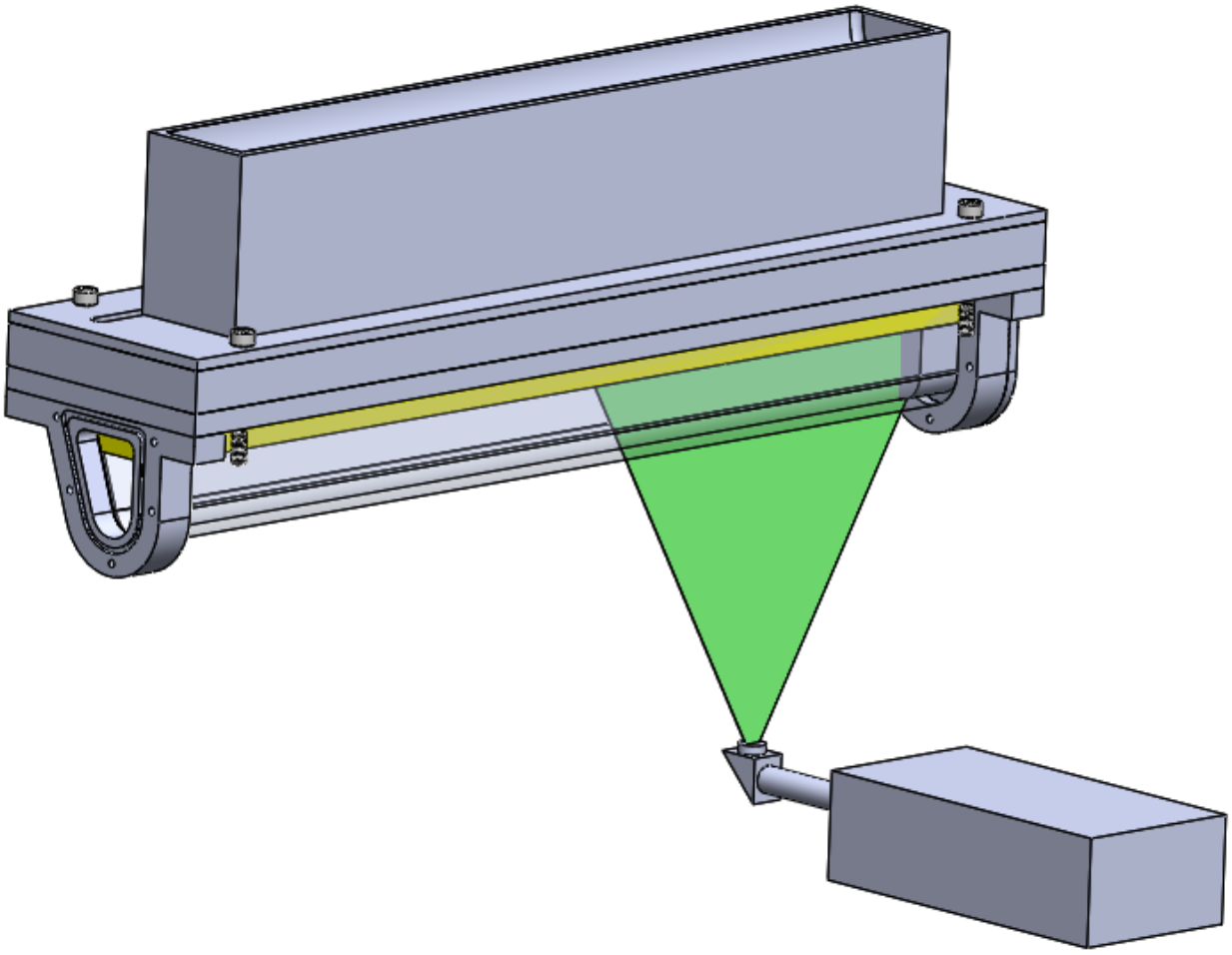

Figure 17: CAD of the PIV set up configuration

6.1 - Methodology

The basis of most imaging velocity measurements rely on a spherical object within the flow with a Stokes number [Eq. 24] less than one. Should this Stokes number be satisfied, the particle is assumed to follow Stokes Law. This universal notion states that the inertial forces of the particle are much weaker than the viscous forces of the fluid, and thus, the particle will follow the path of the fluid.

$$Sk = \sqrt{\frac{\widehat{\omega}}{\vartheta}} d_p \qquad [24]$$

In PIV the flow is seeded with a particulate of Stokes number less than one, and illuminated by a laser plane. The suspended particulate reflects the laser into a camera positioned orthogonal to the laser plane. Image pairs taken in small time steps, in the order of microseconds, allow the movement of the particulate to be tracked with a cross correlation.

The frame size of each picture was chosen to ensure a particle size of 2-3 pixels. This particle-pixel size was chosen to reduce peak locking errors. The camera frame is then split into different interrogation windows. The window size was chosen based on the seeding density within the flow; a target of 8-10 particles per window was used. A window overlap of 75% was also utilized due to the high particle density. The particle displacements within each image pair are overlaid within their windows allowing a cross-correlation to be used to calculate a displacement vector for each window. This displacement vector can be used to find both velocity vectors and 2D TKE values.

$$V = \frac{\Delta x}{\Delta t} \quad [25]$$

$$2D\ TKE = \frac{1}{2}\langle {V_y}'^2 + {V_z}'^2 \rangle \quad [26]$$

The cross correlation compares the position of the particles in an image pair and attempts to match the particles as best possible. When the dot product of these two values are maximum it is assumed that the same particle is being examined. To ensure the proper vector is found the cross correlation is conducted over the interrogation windows comprised of multiple particles, thus matching multiple particles between image pairs. Figure 18 shows how the cross correlation works. A vector field, as shown in Figure 19, is then generated and imposed onto the original image.

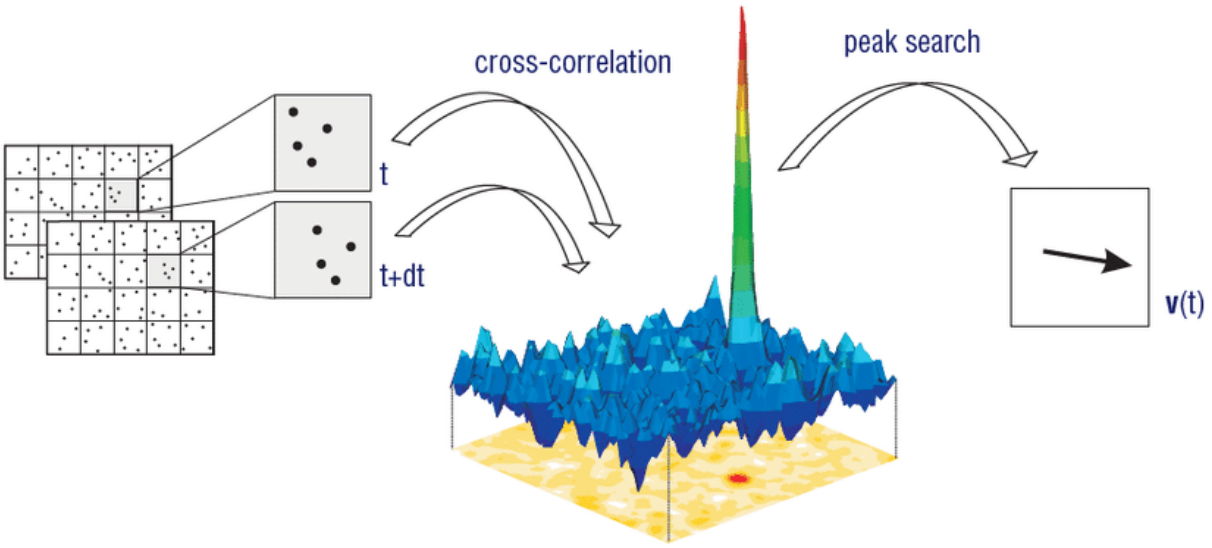

Figure 18: Cross-correlation technique typically used in PIV [Wieneke, 2017]

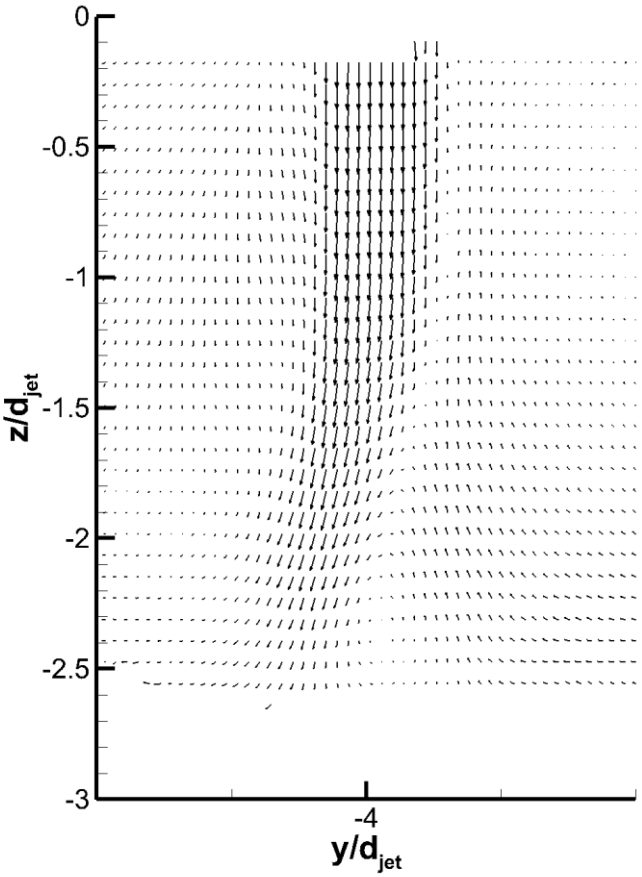

Figure 19: Vector field of mean flow field

Due to the geometry of the experiment, additional steps had to be taken to ensure high quality results. The nature of the curved target surface caused ambient refractions of the laser to impede the data collection. A florescent filter was used in conjunction with a 532nm bandpass filter on the camera lens to prevent unwanted scattered laser reflections.

Table 5: Laser pulse timing for corresponding Reynolds numbers

Reynolds number	Laser pulse Δt (μs)
20,000	59.5
40,000	29.8
60,000	19.9
80,000	14.6

6.2 - Data Acquisition

The data was recorded in the Andor Software and post processed using LaVision Davis 8.3.1 while the laser pulse timing was controlled through LabView VI. The hardware consisted of a Quantel Evergeen Dual Pulsed 200mJ laser and an Andor Zyla 5.5 megapixel camera. The laser used a neodymium-doped yttrium aluminum garnet (nd:YAG) crystal to generate a laser sheet of wavelength 532nm. A laser sheet thickness of ~1mm was achieved by using variable beam optics in parallel with the laser. The camera had a fixed focal length of 55mm.

6.3 - Testing Procedure

The laser was placed underneath the rig and leveled to the table, the laser plane was set identical to the mid-jet plane. The camera was placed orthogonally away from the laser plane. A calibration grid was placed into the rig on the laser plane and the camera was calibrated to the specific spot it was in; once calibrated the camera was not moved between tests.

To begin the test the flow was then turned on and adjusted to the desired Reynolds number. The laser pulse time step was set according to the Reynolds number. The flow was then seeded with olive oil particulate of an average particle diameter between 0.5-1.5 μm using a TSI Laskin-type particle generator and shower head diffuser. Data was recorded in the Andor Software for roughly 2000 image pairs. After each test the inside of the rig was cleaned with a microfiber rag to ensure the optical clarity of the acrylic was preserved for each test.

6.4 - Uncertainty PIV

The uncertainty associated with PIV is difficult to quantify as the results are dependent of a multitude of factors. Various uncertainties are induced from factors such as: image size, particle image density, out of plane motion, peak locking, large gradients, calibration error, and many more. Although these uncertainties are difficult to quantify individually, recent methods have been developed to quantify the uncertainty as a whole. One such method by Sciacchitano and Wieneke (2016) does so with the statistics of the flow.

In this experiment the uncertainty of the mean velocity was quantified by the statistical method from Sciacchitano and Wieneke (2016) using [Eq. 27], where N is the number of image pairs taken. This method uses the recorded experimental standard deviation of the velocity of each interrogation window within the frame, giving a spatially resolved uncertainty. The average uncertainty within the experimental flow field was found to be ~3%.

$$U_V = \frac{\sigma_V}{\sqrt{N}} \qquad [27]$$

CHAPTER 7: COMPUTATIONAL EFFORTS

With today's technology and the availability of commercial CFD software the addition of a numerical study to compare with experimental results is computationally feasible with the resources available. For this study, the commercial CFD software Star CCM+ was utilized. The geometry of the assembled test section generated in SolidWorks was imported into Star CCM+ as the fluid domain for the simulation.

7.1 - Numerical Set Up

7.1.1 - Mesh

The mesh is the foundation of the numerical simulation. The StarCCM+ mesher generates discretized cells to represent the computational domain. These cells are then used by the physics solver to provide a numerical solution. In order to get the best numerical solution it is critical to have a high quality mesh that can capture the localized physics properly.

To begin a surface remesher was used within Star CCM+ to ensure that a high quality surface mesh is generated for the imported CAD, as a low quality surface mesh may improperly model the geometry of the fluid volume. The quality of the surface mesh also has a large effect on the quality of the volume mesh, as the volume mesh is extrapolated from the initial surface mesh.

A polyhedral volume mesher is used for the fluid domain. This mesher generates arbitrary 3D polyhedral shapes to fill in the fluid domain. The length, shape, and size of each polyhedral

cell vary from cell to cell but on average a cell has 14 faces. The polyhedral volume mesher is used because of it is robustness and accuracy in complex geometries compared to the other meshers.

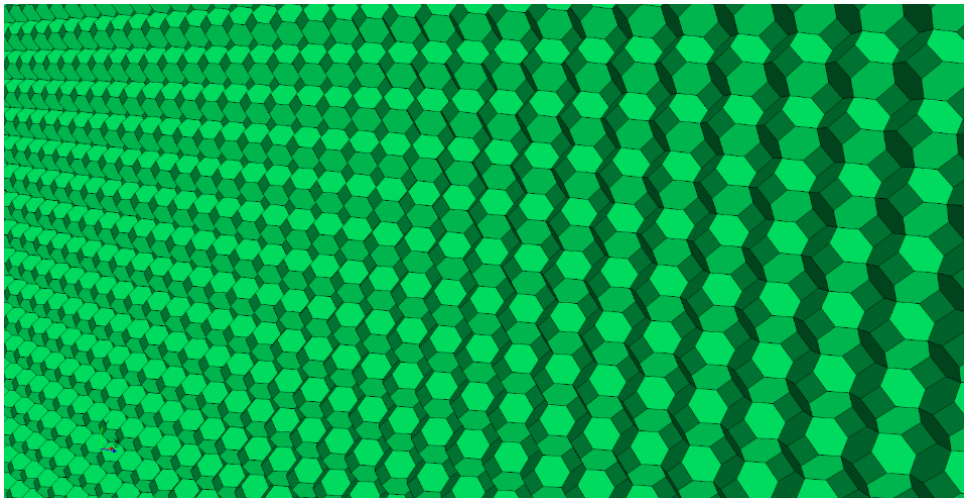

Figure 20: Polyhedral cell Surface

The prism layer mesher is selected in conjunction with the polyhedral mesher to resolve the near wall flow. This mesher generates thin orthogonal prismatic cells next to a surface that gradually grow in size. To generate the prism layers the overall thickness and number of layers were specified per wall. In areas with large gradients, such as the heat transfer surface and jet holes, it is important that more prism layers are present to obtain a more accurate solution of the boundary layer.

Lastly, volumetric controls were applied to specific regions of the test section. This allows for a finer mesh in areas of interest within the jet, while also allowing areas of lesser interest to have a coarser mesh reducing computational time. A single volumetric control was applied to the entirety of the leading-edge cavity to reduce the base cell size where the flow is expected to be more turbulent. Nine volumetric controls were placed under each jet with an even further reduced

base size from the first control. These were created to accurately capture the flow of the jet, its shear layer, and the effects at the stagnation point.

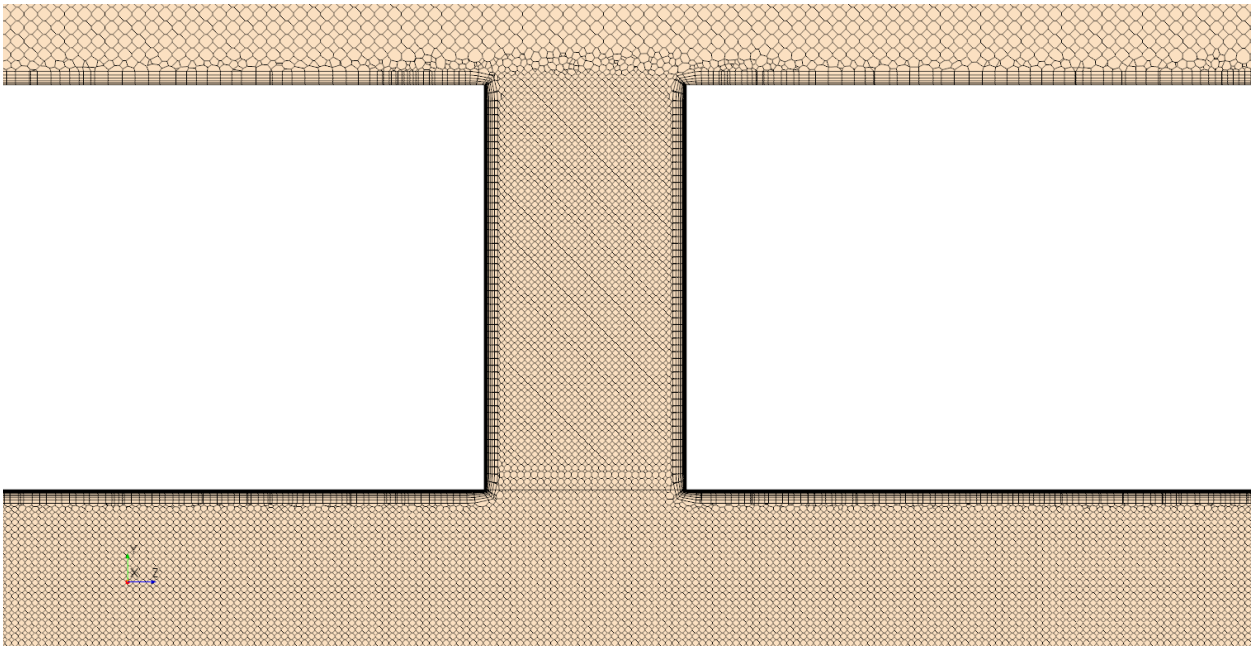

Figure 21: Mid-section plane of mesh and mesh refinement at jets

For flow investigations in near-wall regions it's important that the y+ value is sufficiently small. The wall y+ is a non-dimensional wall distance used to ensure that the cell nearest the wall is within the viscous sub layer region. It is general industry practice to have the wall y+ < 2 to ensure that the near wall region is properly represented. Figure 22 shows that the wall y+ along the heat transfer surfaces are sufficiently low enough to accurately capture the viscous sub layer.

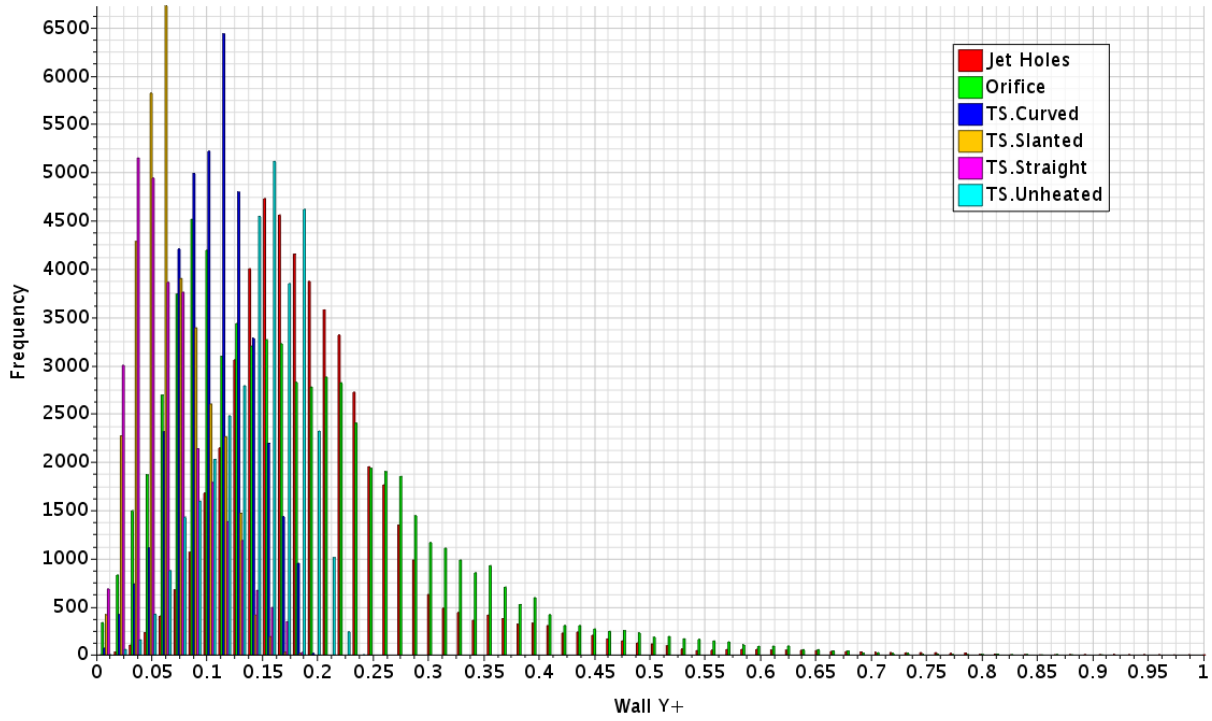

Figure 22: Wall Y+ histogram

7.1.2 - Boundary Conditions

Each surface within the simulation must be defined with a boundary condition. The conditions used in this simulation are an ‘inlet’, ‘outlet’, and ‘wall boundary’. The inlet and outlet boundaries allow fluid to pass through the surface while the wall boundary is an impermeable surface. These wall boundaries are considered adiabatic with a no slip condition unless specified otherwise.

The inlet surface is set to a stagnation inlet boundary condition, in which a constant stagnation pressure is feeding into the test section. This boundary condition was used because the experimental tests occurred in a large room with negligible air flow which could be assumed to be at a stagnation condition. The defined properties at the inlet were the average pressure and temperature which were measured while testing experimentally. These were 101.3 kPa and 300K respectively.

A mass flow rate controlled pressure outlet boundary condition was set at the exit of the test section. A desired mass flow is input, and the pressure is automatically adjusted with each iteration until the desired mass flow rate is achieved. This desired mass flow rate changes from case to case depending on the Reynolds number being tested.

In the simulation the target surface is split into 3 distinct sections: the curved target surface, the suction side wall, and the pressure side wall. While the boundary conditions of these surfaces are a wall boundary, they are not adiabatic. A constant temperature of 330K is applied to the target surfaces giving a ΔT of 30K from the inlet temperature, matching the same ΔT used experimentally.

7.1.3 - Physics Models

This section discusses the different physics models selected within Star CCM+. These physics models dictate the equations used in the numerical calculations within Star CCM+ and it is crucial to use the proper physics models to get accurate results. The overlying physics models are set in 3D space containing a fluid medium. The fluid being modeled is a gas defined with the properties of standard air behaving in a turbulent viscous regime. More physics models are discussed in depth below.

7.1.3.1 - Flow Model

The segregated flow model selected solves the momentum and continuity equations separately for both velocity and pressure. The momentum and continuity equations are then linked through a predictor-corrector approach.

7.1.3.2 - Energy Model

The energy model used was the segregated fluid temperature model. This model was used because it is efficient when combustion is not present. The segregated fluid temperature model solves the energy equation using temperature as the solved variable and computing enthalpy according to the equation of state.

$$\frac{\partial}{\partial t}(\rho E V_0) + \sum_f \{[\rho H(v - v_g) + v_g p + \dot{q}'' - (T \cdot v)] \cdot a\}_f = (f \cdot v + s)V_0 \qquad [28]$$

7.1.3.3 - Equation of State

The equation of state (EOS) model is used to compute the density and density derivatives within the fluid regime of the simulation. The ideal gas EOS was enabled. This model assumes the ideal gas law and calculates density as function of temperature and pressure.

7.1.4 - Turbulence Model

The turbulence model is one of the most important aspects to a computational simulation. If the wrong turbulence model is used the final results may be drastically over-predicted/under-predicted than the experimental values. The turbulence model is responsible for providing closure of the governing equations in turbulent flows.

As discussed earlier, an SST k-ω turbulence model was used. This turbulence model solves the RANS equations, forms of the continuity, momentum, and energy equations decomposed into average and fluctuation components. The SST k-ω turbulence model is a variance of the original k-w model which adds an additional non-conservative cross-diffusion term to better model the far-field.

$$\frac{d}{dt}\int_V \rho k dV + \int_A \rho k\left(v - v_g\right) * da = \int_A (\mu + \sigma_k \mu_t)\nabla k * da + \int_V (\gamma_{eff} G_k - \gamma' \rho \beta^* f_{\beta^*}(\omega k - \omega_0 k_0) + S_k) dV \quad [29]$$

$$\frac{d}{dt}\int_V \rho \omega dV + \int_A \rho \omega\left(v - v_g\right) * da = \int_A (\mu + \sigma_\omega \mu_t)\nabla w * da + \int_V (G_\omega - \rho\beta(\omega^2 - {\omega_0}^2) + D_\omega + S_\omega) dV \quad [30]$$

7.2 – Simulation Convergence

Convergence of the numerical simulation was determined by the convergence of the iterative average of various parameters. An iteration average was used due to the fluctions about a mean of the values within the simulation, such as that seen of Nusselt number in Figure 23. The paramaters studied for convergence consisted of Nusselt number, velocity, temperature, and pressure; these were chosen as they pertain to the main parameters investigated experimentally.

To judge convergence, the area average Nusselt number of the first three copper sections in the experiment were monitores. Figure 24; meanwhile, probes were placed in shear layer of the first four jets to monitor the other parameters. The probes were positioned in the shear layer as this is where the highest variance is located and will take the longest to converge, thus if the shear layer has converged it can be assumed the rest of the flow field has converged.

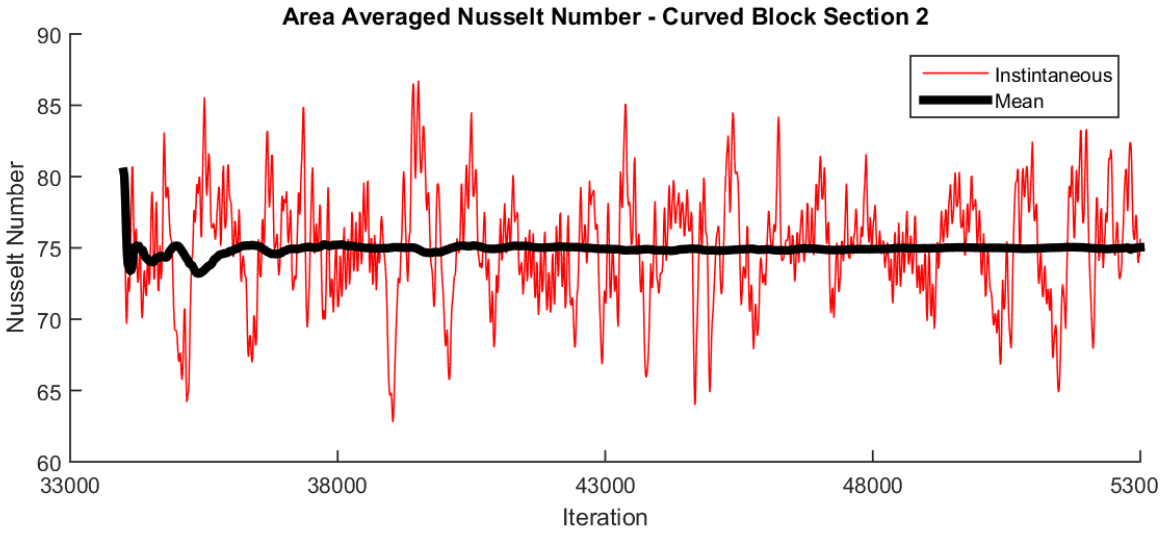

Figure 23: Convergence of mean value vs instantaneous value

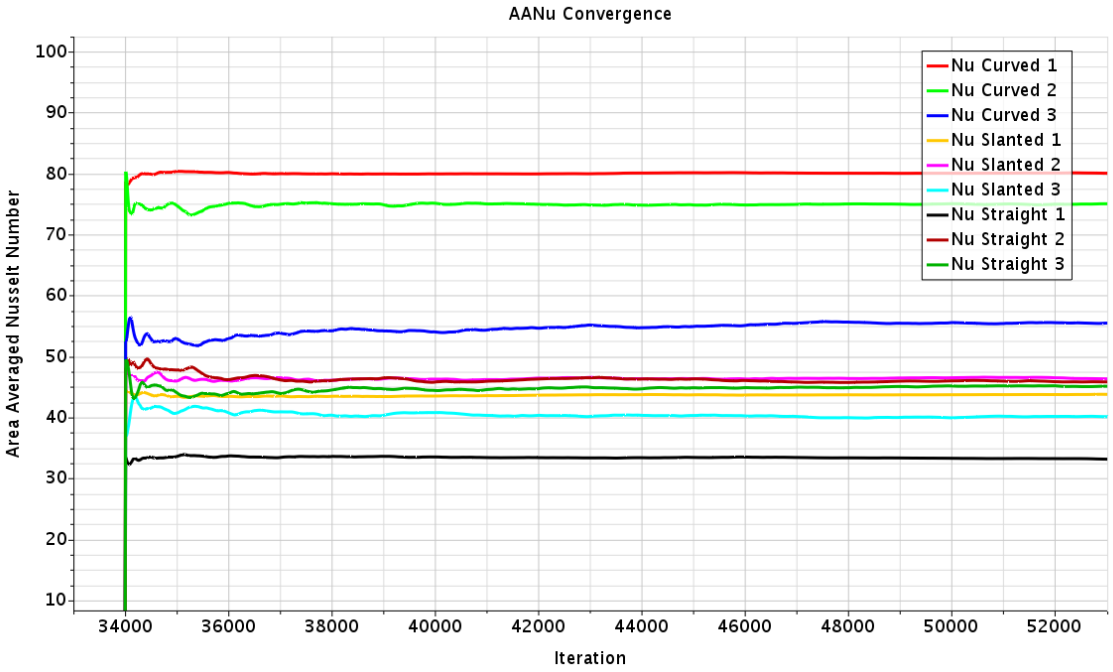

Figure 24: Convergence plot of Re = 20k, H/d – 2.7, area average Nusselt number

7.3 - Mesh Convergence Study

To ensure that the mesh used in this study was sufficient enough to produce an accurate numerical solution a mesh convergence study was conducted. In this study a base mesh was generated and the base size refined through four iterations of meshes. This resulted in four different meshes of varying base size and total cell count, all while having the same boundary conditions and physics models. The simulations were then run and the solutions compared. Should the solutions converge with mesh size then it can be confidently assumed that the mesh used accurately captures the simulation solution. Table 6 below lists the key parameters of the four meshes used.

Table 6: Mesh sizes used in mesh convergence

Mesh Size	Base Size in Test Section
4 million cells	4mm
8.5 million cells	2mm
11.5 million cells	1.25mm
15 million cells	1mm

7.3.1 – Mesh Convergence Results

To determine if the simulations were converged the velocity plots at the 1st jet were looked at. The results are shown in Figure 25 below. There is very little deviation between the meshes, with the maximum difference of <5%. The velocity contours also approach the finest mesh of 15 million cells. Other data points investigated showed similar results. In conclusion, it can be assumed that the 15 million cell mesh is sufficient to capture the accurate solution and thus was used in this study.

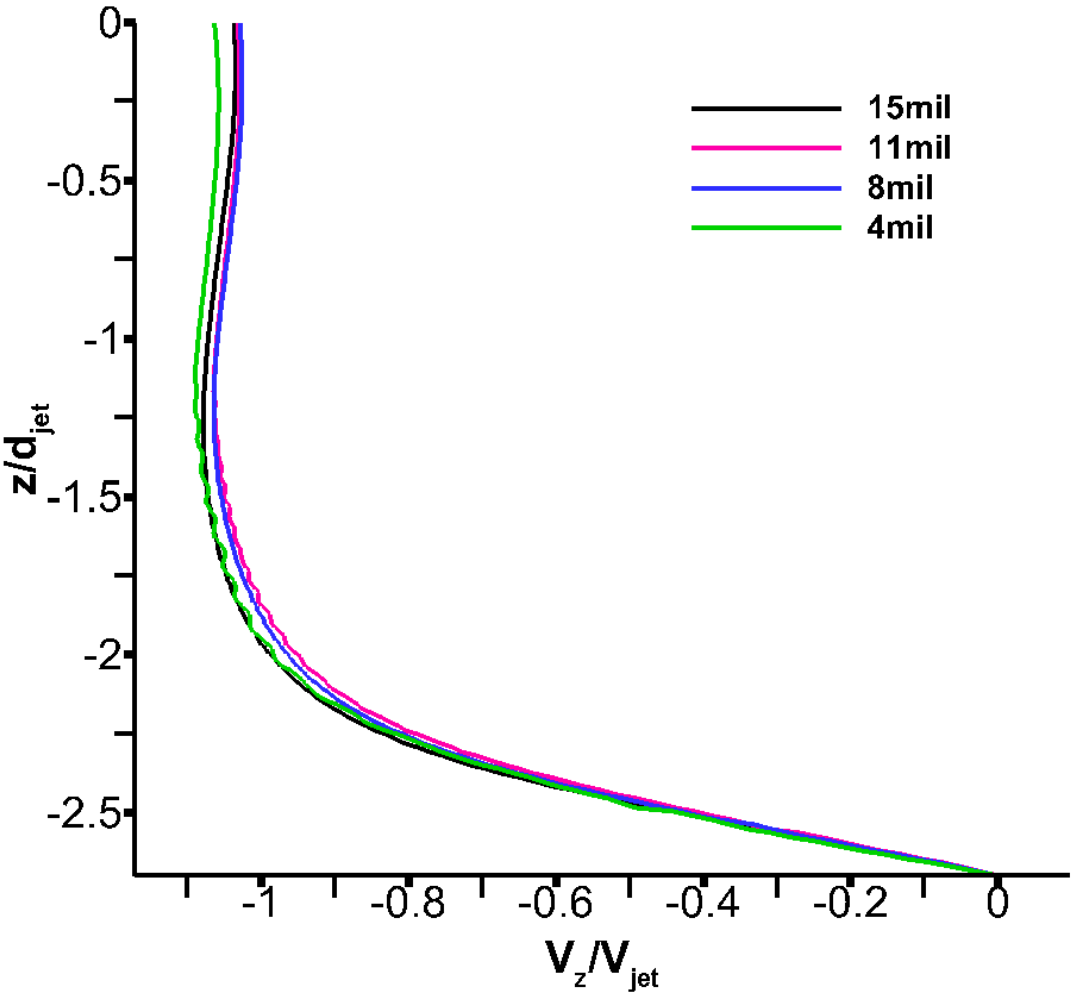

Figure 25: Mesh convergence results: axial velocity at y/d = 0

7.4 - Computational Errors

It is known and expected that the numerical results will not match the experimental results exactly. Examples of this is the tendency for the numerical results to overpredict pressure drop, overpredict stagnation region heat transfer, and underpredict heat transfer in crossflow. These are all well documented in literature. However, upon initial comparison of the computational results there were several extreme disparities found pertaining to the pressure drop and the flow fields.

The pressure drop in the CFD, represented in terms of velocity in Figure 26 below, greatly overpredicted that seen in the experiment. However, the trends of the two are very similar. Likewise, the axial velocity at wall normal distance z/d = 1 are also overpredicted by the CFD in the jet regions. This axial velocity plot in Figure 27 shows that the axial velocity of the jets in the simulation are substantially higher than that of the experiment. Upon further investigation of the numerical results it was discovered that a strong vena contracta effect was happening at the upstream side of the jet hole. This vena contracta is modeled by an isosurface of axial velocity less than zero (axial velocity moving downward in the picture reference frame) in Figure 28.

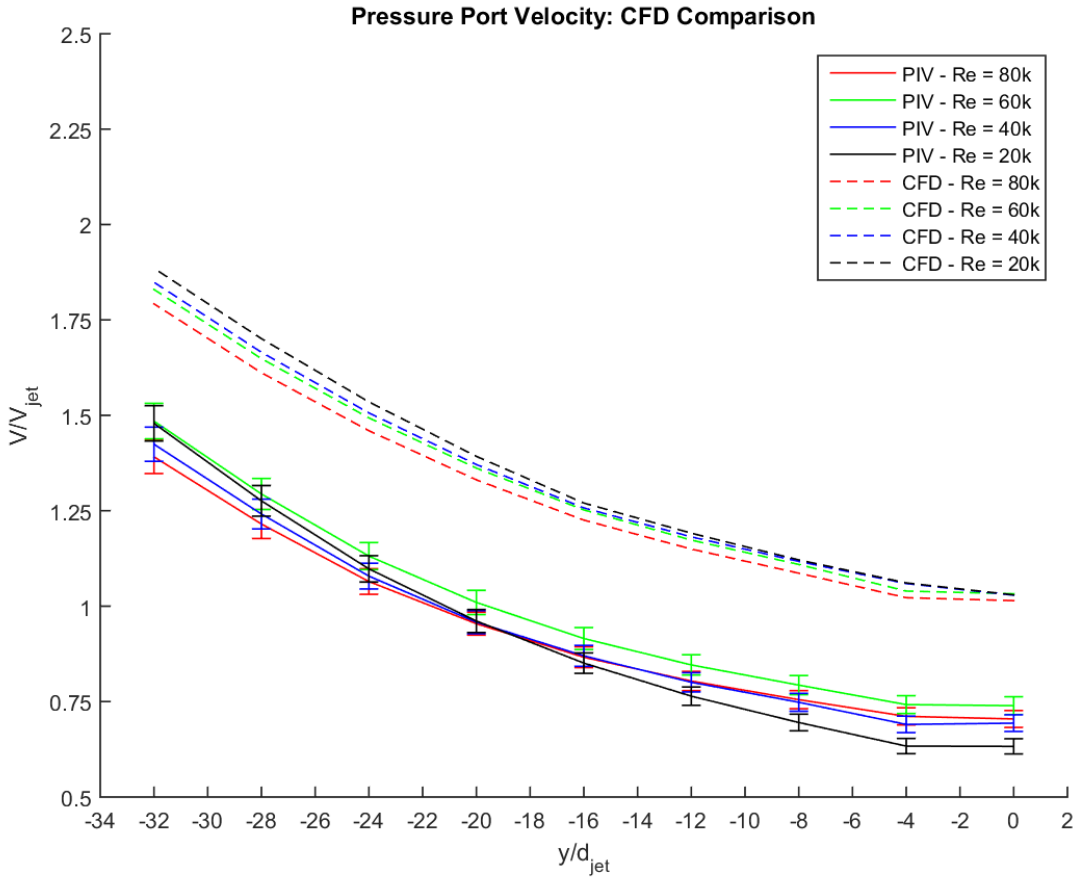

Figure 26: CFD pressure drop comparison

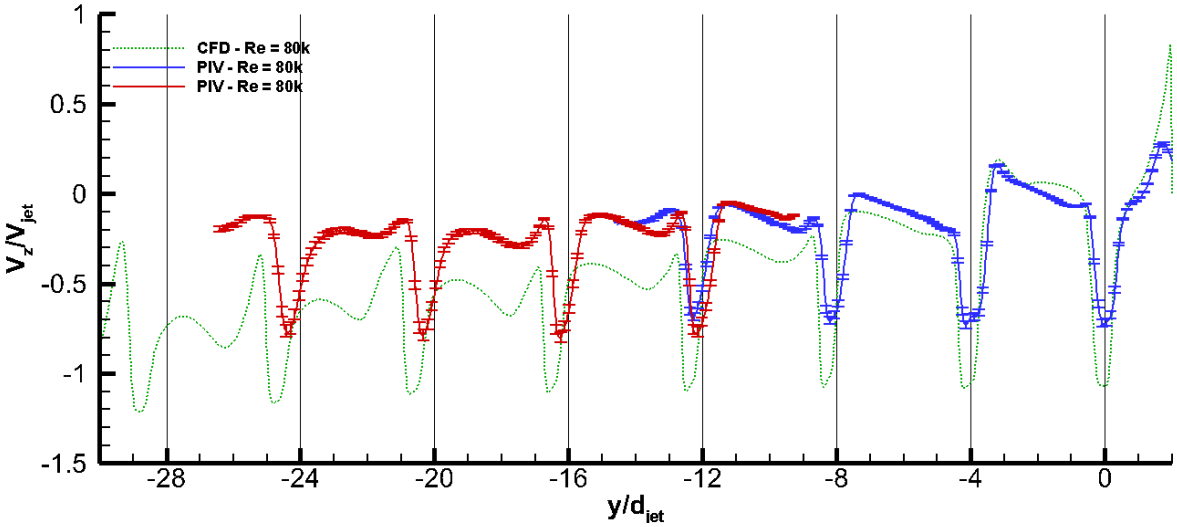

Figure 27: Axial velocity at wall normal distance z/d = 1 for Re = 80k

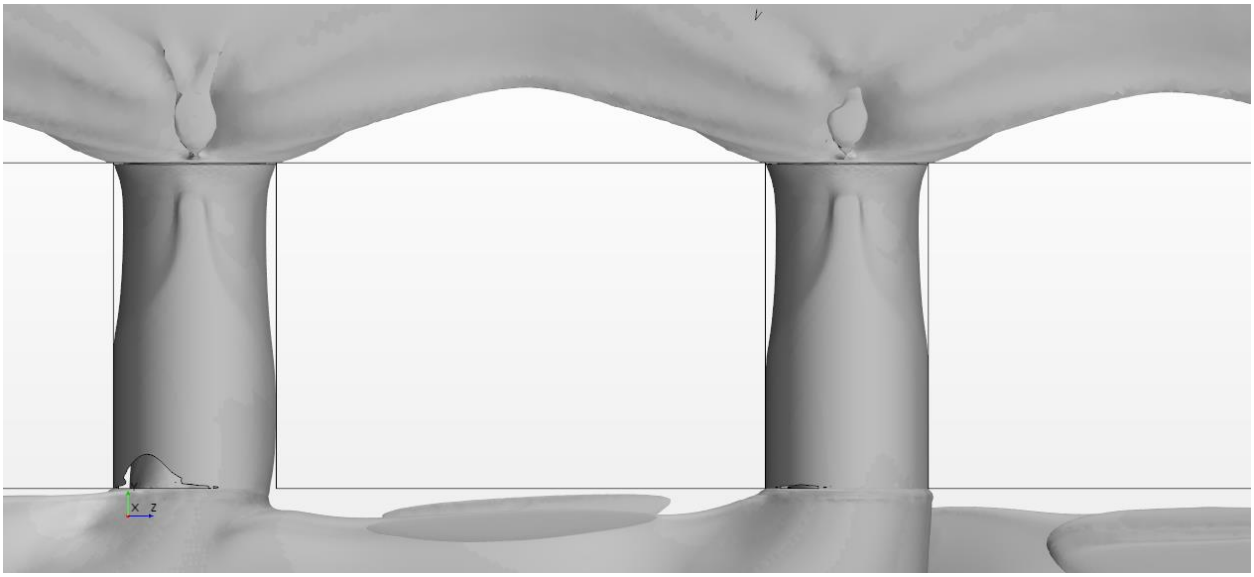

Figure 28: Vena contracta effect within the numerical simulation

This vena contracta effect is caused by the inability for the flow to quickly turn into the jet hole, thus gradually turning and separating from the wall. This separation constricts the flow reducing the effective jet diameter temporarily. This reduction in effective diameter, along with the conservation of mass, causes the velocity to increase. When measured, this vena contracta reduced the effective jet diameter from 15mm to 13mm; using the conservation of mass and assuming a constant density, this ratio of diameters would induce a 33% increase in jet velocity. From the collected data, the CFD is overpredicting the velocity of the jets by roughly 30%-50%.

This effect was extensively studied by Penumadu and Rao (2017). In this study they documented the pressure drop within an array of impinging jets both experimentally and numerically. The experimental pressure drop tests conducted measured the pressure drop due to the jet holes, friction, and the channel. Their numerical test matrix consisted of a comparison between RANS k-ω SST, RANS k-ε, and a laminar model. All three numerical models overpredicted the pressure drop by roughly 50% and this overprediction increased with Reynolds

number. A URANS k-ω SST turbulence model was run to further investigate the flow field. In this unsteady numerical simulation, the majority of the pressure drop was associated with the entrance to the jets and the vena contracta effect occurring there. A semi-analytical approach further backed this up showing that a large majority of the pressure drop within the system occurs within the jet holes.

After discovering this overprediction of the vena contracta effect an extensive testing campaign of numerical simulations were run. This testing campaign included refinement of the mesh near the jet hole entrance, several different turbulence models, and adjusting parameters of the SST k-ω turbulence model. Through all of these there was negligible change in the pressure drop and velocities of the jet.

However, in one model the vena contracta effect was completely removed by modifying the geometry to a bellmouth jet hole orifice instead of a sharp corner orifice. This modification allows the fluid to gradually bend along the curvature of the bellmouth without detaching from the surface. By removing the vena contracta effect completely the axial velocity of the jet was underpredeicted by the simulation; supporting the conclusion that there is a vena contracta effect within the experiment, and this experimental vena contracta effect falls somewhere between the original CFD model and the modified bellmouth model. Although this new modified geometry eliminated the vena contracta effect, the original geometry was used in the simulation to keep constant with the experimental geometry.

CHAPTER 8: RESULTS

This section will discuss the results of the experimental and numerical aspects of this study. It is broken up into two sections: Jet Characteristics and Heat Transfer. The former section quantifies the mean fluid flow field to better understand how the flow behaves within the leading edge; the former then attributes the flow field to explain the heat transfer occuring within the leading edge.

8.1 - Jet Characteristics

In order to attribute the fluid interactions to heat transfer effects the fluid flow field of the impinging jets and the crossflow must be properly identified and characterized. To do so, the potential core, crossflow effects, and flow features are discussed in depth.

In this section the fluid flow field is characterized qualitatively through contours along the jet centerline plane (x/d = 0), and quantitatively by the velocity components along specific slices of the jet centerline plane. Finally, a few of the vortices are investigated in the 3D space of StarCCM+.

8.1.1 - Jet Centerline Plane Contour Plots

The jet centerline plane (x/d = 0) is the location where the PIV laser sheet was positioned for the experimental testing and thus the plane where all of the experimental data is extracted from. This plane captures the center cross section of each jet and the intended stagnation point of each jet in the absence of crossflow. The contours of this plane show the overall velocity profile and a glimpse of the salient flow structures throughout the test section.

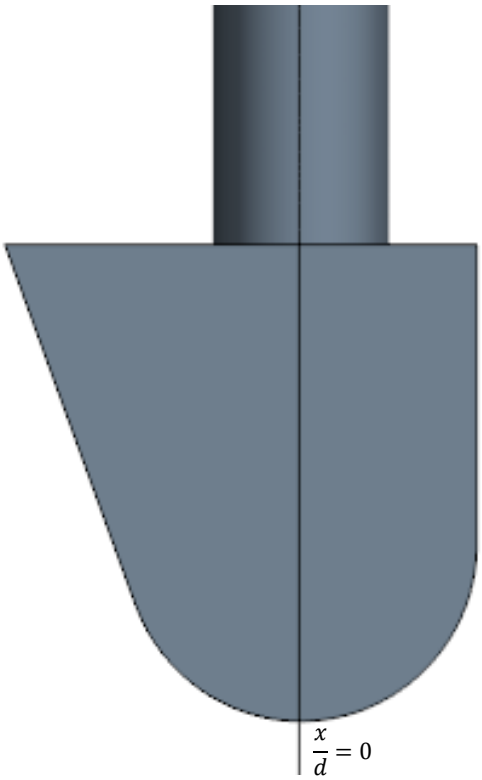

Figure 29: Location of jet centerline in leading edge

The proceeding contour plots are all shown in terms of normalized velocity magnitude [Eq. 32], normalized by the average jet velocity [Eq. 31]. Further, the plots are split into the groups of 'Upstream' and 'Downstream' corresponding to the PIV laser position during the experiment and which jets were captured within the frame of the camera. In this section the 'Upstream' jets correspond to jets 1 through 4 and the 'Downstream' jets correspond to jets 4 through 7. Lastly, there are areas of the plots that are missing near the jet orifice (z/d = 0) and the target surface (either z/d = 2.7 or z/d = 4) due to pooling of the olive oil particulate during testing. This local loss of data is more prevalent in the higher Reynolds number tests.

$$V_{jet} = \frac{\dot{m}}{9\rho A} \quad [31]$$

$$\frac{V}{V_{jet}} \quad [32]$$

Figure 30 below shows the contour plots of the upstream jets in the H/d = 2.7 configuration. There is an inverse relationship between velocity and Reynolds number, being that at the higher Reynolds number the normalized velocity is lower. However, the underlying flow structures are the same throughout all Reynolds numbers. Because of this, the contour plot of a single Reynolds numbers case will be examined qualitatively in this section, however all Reynolds numbers will be examined in future sections. For this section the Reynolds number of 60,000 was chosen to be examined. The full data set of jet centerline contour plots can be found in Figures 70 through 77 in appendix A.

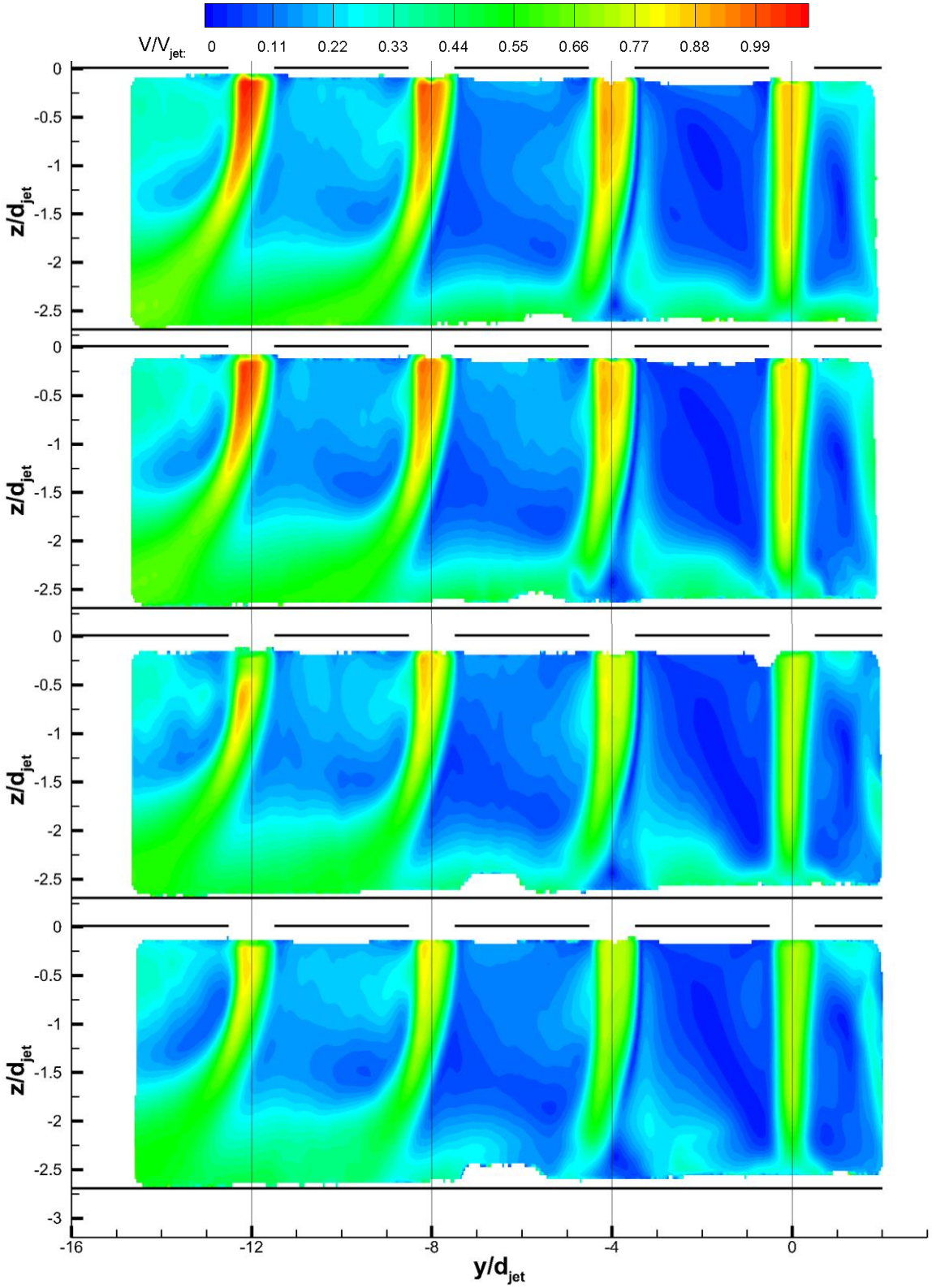

Figure 30: PIV velocity contour plots at H/d = 2.7, -16 < y/d < 2:
Top to bottom: Re = 20k, Re = 40k, Re = 60k, Re = 80k

8.1.1.1 - Upstream Jets

The upstream jets, corresponding to jets 1 through 4, experience the least amount of crossflow effects and jet bending. Therefore the most interesting flow structures form here as they are not washed out by the crossflow. Figures 31 and 32 show the jet centerline velocity contours for the H/d =2.7 and H/d = 4 configurations respectively.

In both configurations the 1st jet extends fully down to the target surface forming a stagnation region low velocity and a wall jet region flow in the spanwise directions. The portion of the wall jet that travels upstream (to y/d = 2) reaches the end wall and creates an upwash along the back wall. The fluid within this upwash is either entrained back into the jet or recirculates into a vortex. This vortex spans the entire height of the channel in each configuration, leading to the H/d = 4 configuration to have a larger vortex. The other wall jet, that moves downstream, reaches the 2nd jet and causes a variety of different interactions.

At the 2nd jet, the spent air from the 1st jet is upwashed along the backside of the jet and then entrained into the jet itself. This entrained fluid along with new fluid from the 2nd jet impinges on the target surface and forms a vortex that is reminiscent of a typical horseshoe vortex that is seen in narrow wall impingement. This vortex is located directly on the jet's spanwise location (y/d = -4) and causes the jet to bend, shifting the stagnation region of the jet downstream. This vortex is stretched over a larger area for the H/d = 4 configuration but jet bending effect is comparable to that in the H/d = 2.7 configuration.

The 3rd and 4th jets begin to have an increasing velocity magnitude, but also have an increasing jet bending effect. In the H/d = 2.7 configuration the jet bending effect is stronger and thus eliminates the stagnation region at the 3rd and 4th jet completely. The H/d = 4 configuration still has a stagnation region present at the 4th jet, although it is extremely weak and shifted

downstream by ~1 y/d. In both configurations the fluid from these jets transition directly into the crossflow and a larger boundary layer along the curved surface begins to form.

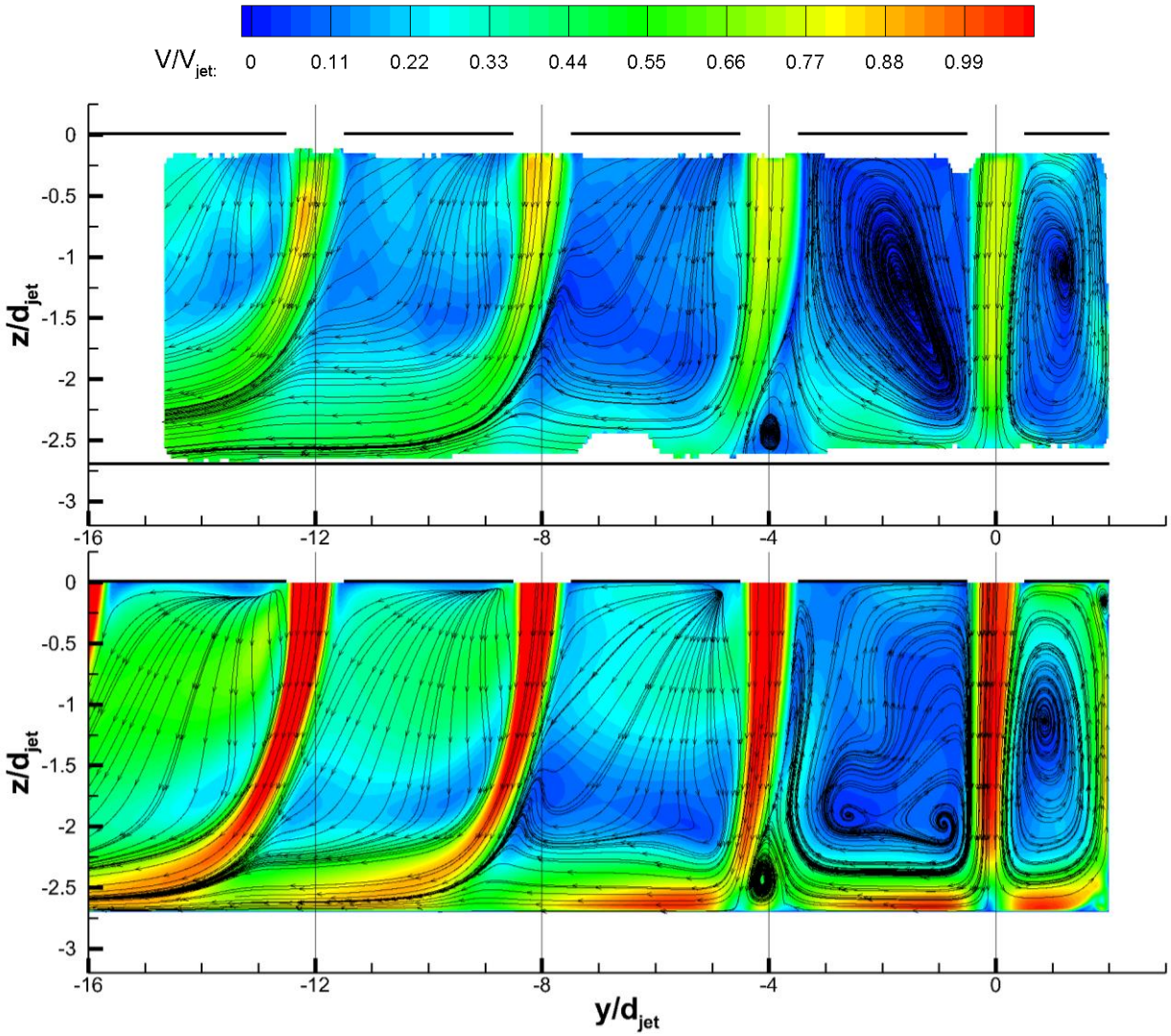

Figure 31: Velocity contour plot of H/d = 2.7, Re = 60k, -16 < y/d < 2
PIV (top), CFD (bottom)

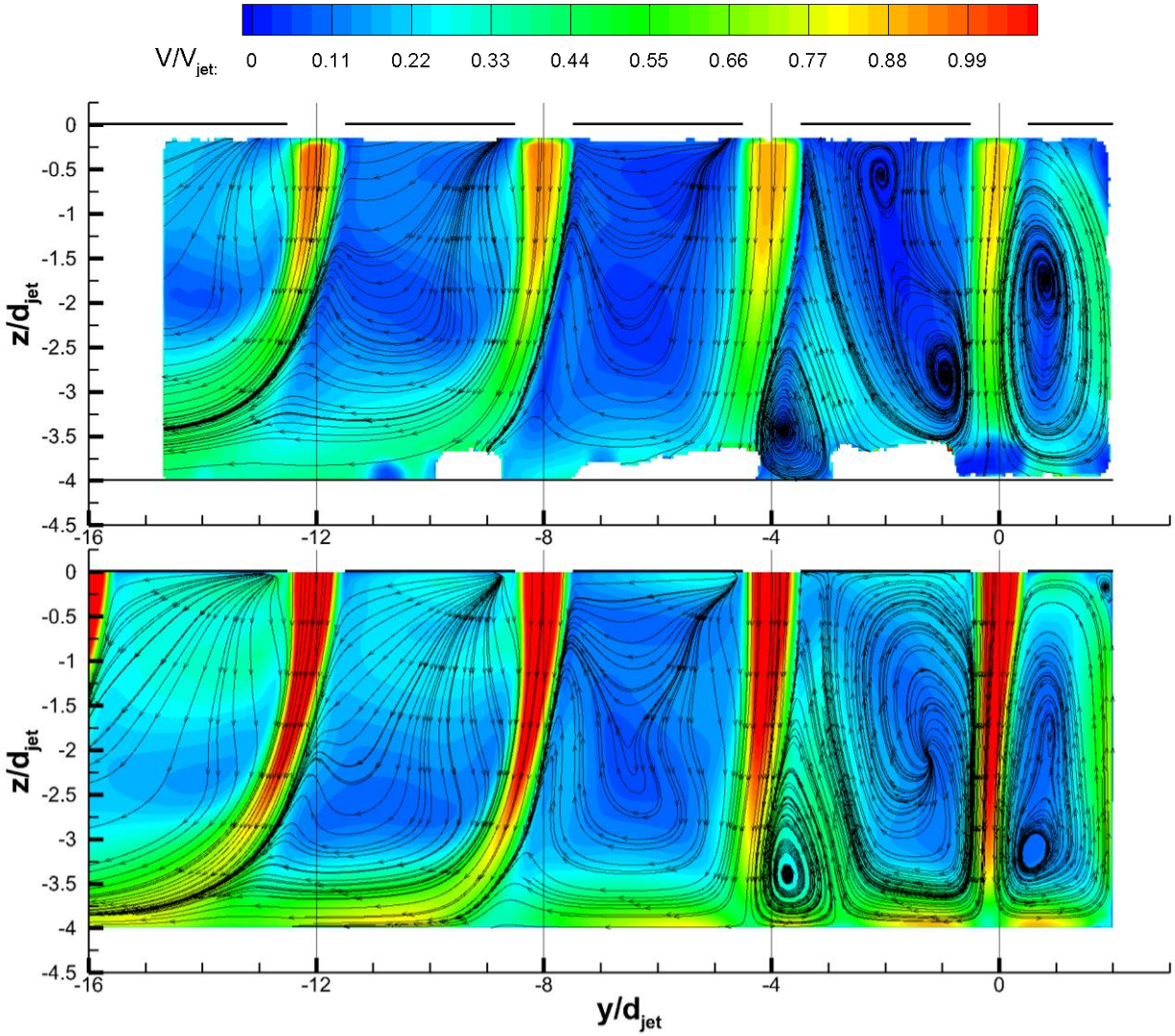

Figure 32: Velocity contour plot of H/d = 4, Re = 60k, -16 < y/d < 2
PIV (top), CFD (bottom)

8.1.1.2 - Downstream Jets

The downstream jets, corresponding to jets 4 through 7, have an increasing potential core velocity due to the lower localized pressure as seen in the pressure drop data. At these y/d locations there are very little flow structures as the fluid is dominated by the crossflow. Figures 33 and 34 show the jet centerline velocity contours for the H/d =2.7 and H/d = 4 configurations respectively.

At the downstream jets the crossflow effects are dominant causing the potential cores to diminish rapidly and the jets to bend. This jet bending due to the increased crossflow has completely eliminated the stagnation region by the 4^{th} jet and the spent fluid from the jet is entrained directly into the crossflow. This increase in the crossflow velocity and jet bending is much faster and apparent in the H/d = 2.7 configuration than the H/d = 4.

The boundary layer flow along the curved surface quickly grows as spent air from each subsequent jet is entrained. By the 5^{th} jet the thickness of this region is ~1 z/d thick. In the experimental results of the H/d = 4 configuration, Figure 34 (top), this boundary layer attaches and detaches itself from the target surface in waves. There is no current explanation for this and further investigation is considered.

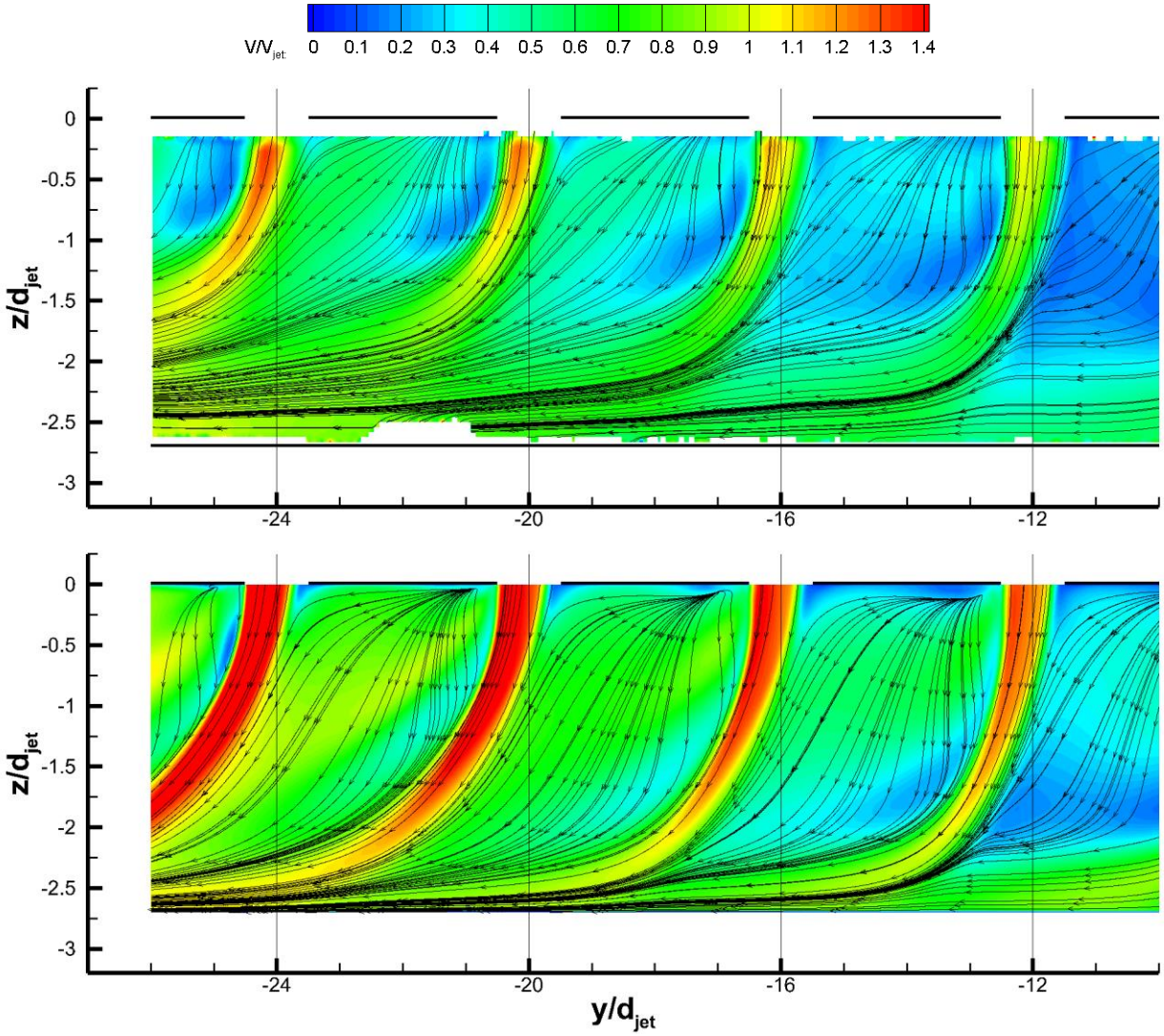

Figure 33: Velocity contour plot of H/d = 2.7, Re = 60k, -26 < y/d < -14: PIV (top), CFD (bottom)

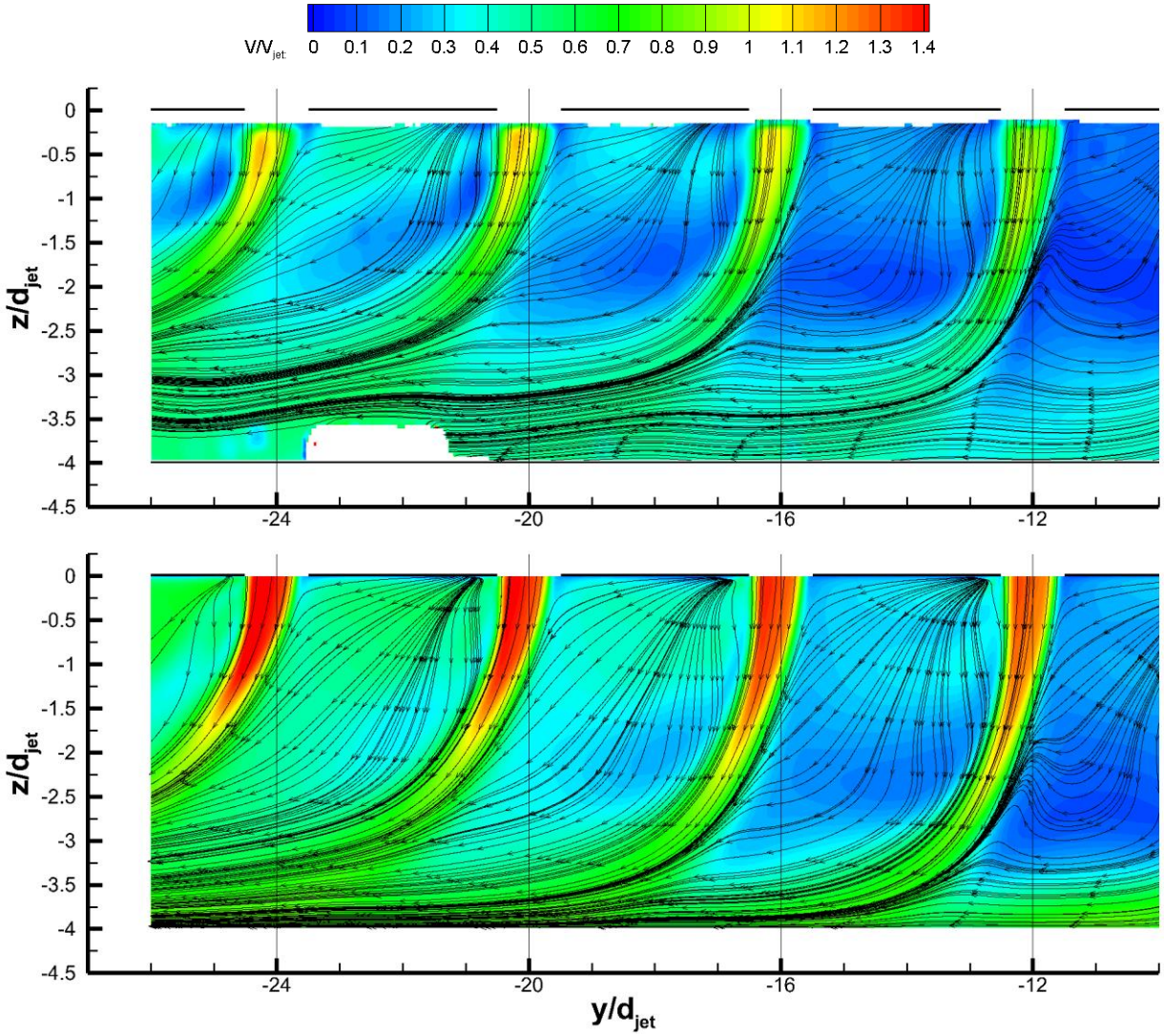

Figure 34: Velocity contour plot of H/d = 4, Re = 60k, -26 < y/d < -14: PIV (top), CFD (bottom)

8.1.2 - Axial Velocity at Different Wall Normal Locations

One of the largest drivers in jet impingement heat transfer is the strength of the potential core of the jet. The overall strength of the potential core is typically characterized by two factors: the width and the velocity. As the jet moves further away from the orifice, instabilities in the shear layer will weaken the potential core causing its width and velocity to decrease.

To identify the potential cores of the jets, the axial velocity was plotted at three different wall normal locations (z/d = 0.5, 1, 1.5) on the jet-centerline plane. Figure 35 below specifies the wall normal locations at which the axial velocities are plotted. In the following plots the axial velocities were normalized by [Eq. 33].

$$\frac{V_z}{V_{jet}} \qquad [\boldsymbol{33}]$$

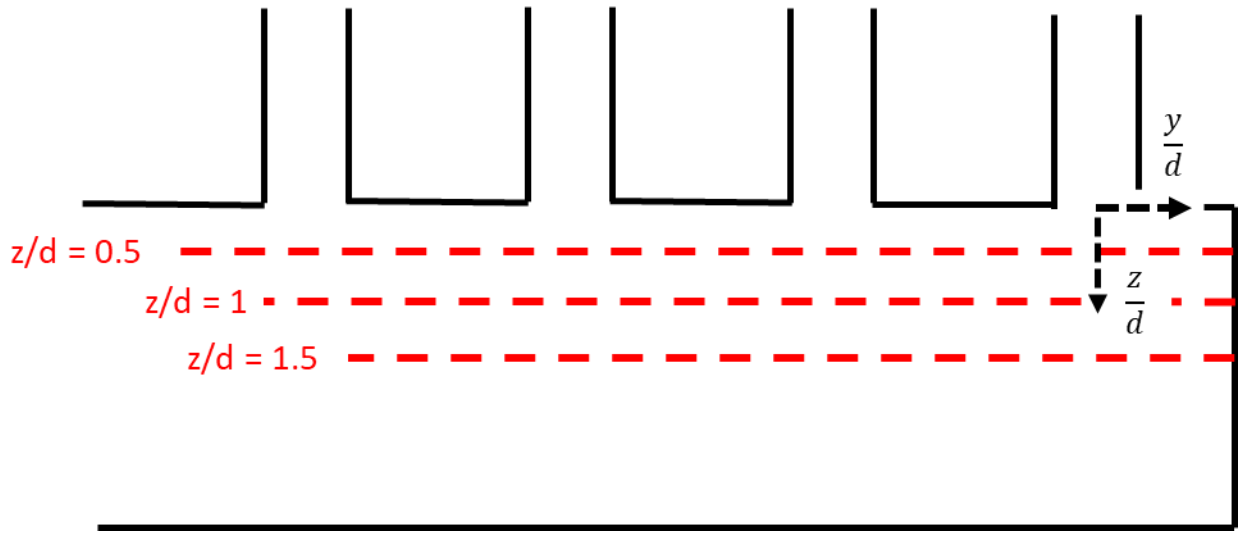

Figure 35: Wall normal locations

To reduce graph clutter the assumption is made that when normalized, all of the test cases are the same, and thus it is sufficient to examine a single Reynolds number case. To validate this assumption the full Reynolds number data sets are compared at wall normal distance z/d = 1 in Figure 36.

In Figure 36, the experimental data collapses when normalized with respect to one another, showing that a single Reynolds number case can be used to describe each geometrical configuration. The numerical results also normalize properly, however overpredicting the experimental results. Further, this normalization was proven to be sufficient at all H/d's, and the full data set of the axial velocities at different wall normal distances can be found in Figures 78 through 80 in appendix A.

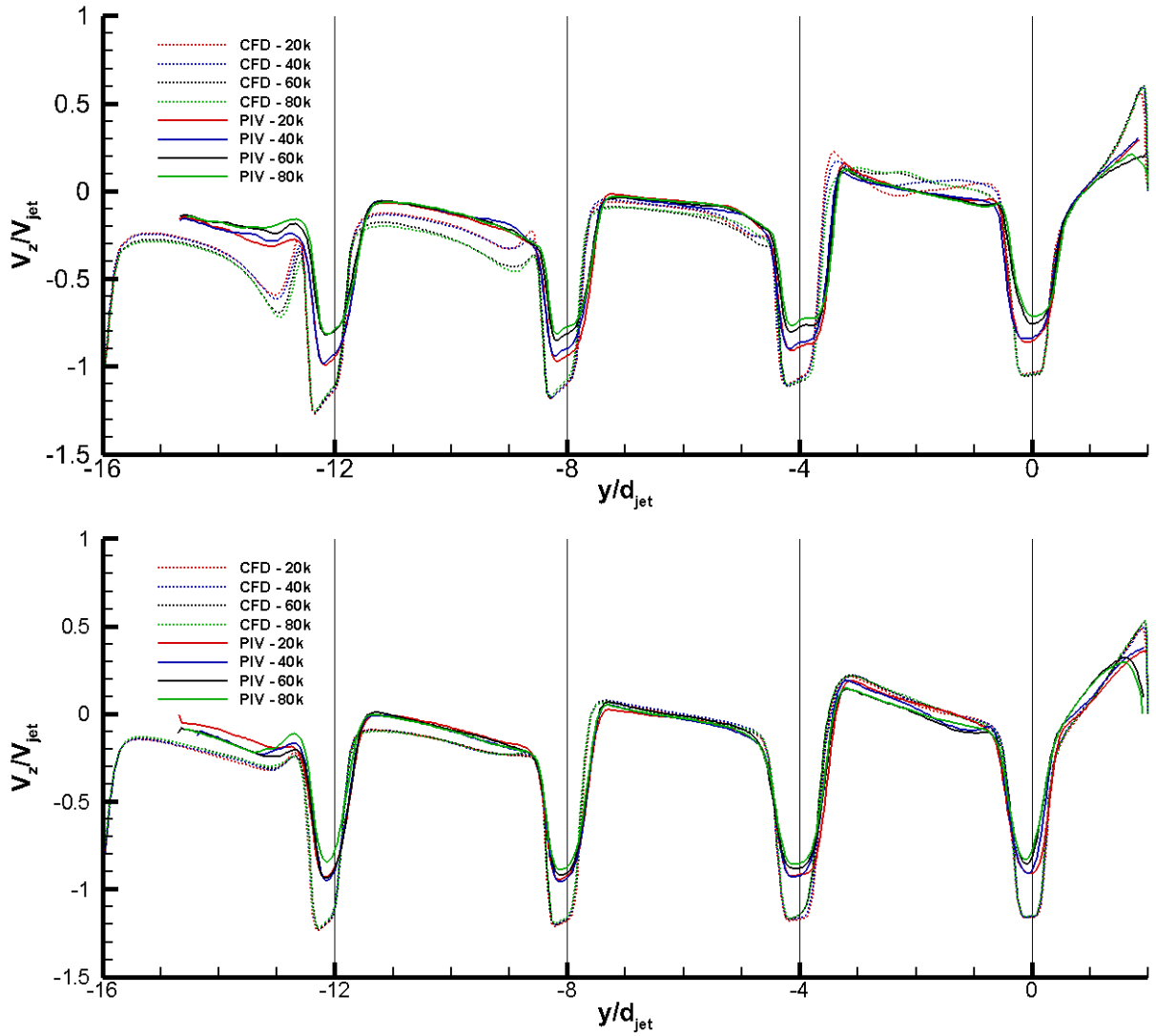

Figure 36: Axial velocity at wall normal location z/d = 1:
H/d = 2.7 (top), H/d = 4 (bottom)

Figures 37 and 38 investigates a single Reynolds number, Re = 60,000, at each of the wall normal distances. Figures 37 (top) and 38 (top) show the experimental data for the H/d = 2.7 and H/d = 4 configurations respectively; Figures 37 (bottom) and 38 (bottom) show the numerical data for the H/d = 2.7 and H/d = 4 configurations respectively.

For the H/d = 2/7 configuration, the axial velocity and potential core of the 1st jet are similar at all of the wall normal distances. This shows that the potential core keeps its strength up until, and past, z/d = 1.5. However, downstream at the 2nd jet the diminishing strength of the potential core can be seen from z/d = 0.5 to z/d = 1.0. At wall normal position z/d = 1.5 the 2nd jet's potential core strength and size has diminished considerably; shown by the lower velocity and the thinner y/d width. These are the aforementioned effects of the shear layer dissipating the kinetic energy of the potential core. There is also a slight shift downstream in the peak of the 2nd jet at this wall normal position. This shift is referring to the spanwise y/d location of highest velocity with respect to the jet centerline. The peak shift signals how far downstream the jet is bending due to the crossflow effects. Directly upstream of the 2nd jet the positive axial velocity associated with the upwash seen in the contour plot is apparent, although there are no velocity components associated with the vortex as it's at a further wall normal distance.

The effects seen at the 2nd jet are further exacerbated at the latter downstream 3rd and 4th jets. For both jets, the weakening of the potential core is faster and more obvious; all the while the peaks shift further downstream showing larger jet bending. At the 3rd jet, y/d = -8, the potential core at wall normal distance z/d = 0.5 has a similar profile to that seen at the previous jets; however the potential core progressively weakens at each following wall normal distance. This more aggressive deterioration of the potential core is due to the larger crossflow at these locations attributing more to the shear forces. This overall weaker potential core and stronger crossflow then

ensues more jet bending. At each subsequent jet these effects become stronger as can be seen from the 4th jet compared to the 3rd jet.

The H/d = 4 configuration follows many of the same trends seen in the H/d = 2.7 configuration. The potential core of the 1st jet is mostly unchanged at wall normal distance z/d = 1.5, and the 2nd jet also has little change in the potential core at wall normal distance z/d = 1.5. The 3rd and 4th jet however do not see the same drastic changes in axial velocity as the previous configuration. These jets behave similar to the 2nd jet and have a slight decrease in potential core strength as the wall normal distance increases.

Overall, for both configurations the numerical results match the trends of the experimental extremely well. Although the velocity is over predicted, the shifts and locations of the peaks are similar. In the H/d = 2.7 configuration, Figure 37, the numerical velocities exhibit a shift that is on the same magnitude of that seen in the experimental results. The same is true for the relationship between the numerical and experimental data of the H/d = 4 configuration; while the velocities were overpredicted, the shift and decrease of potential core strength were proportional.

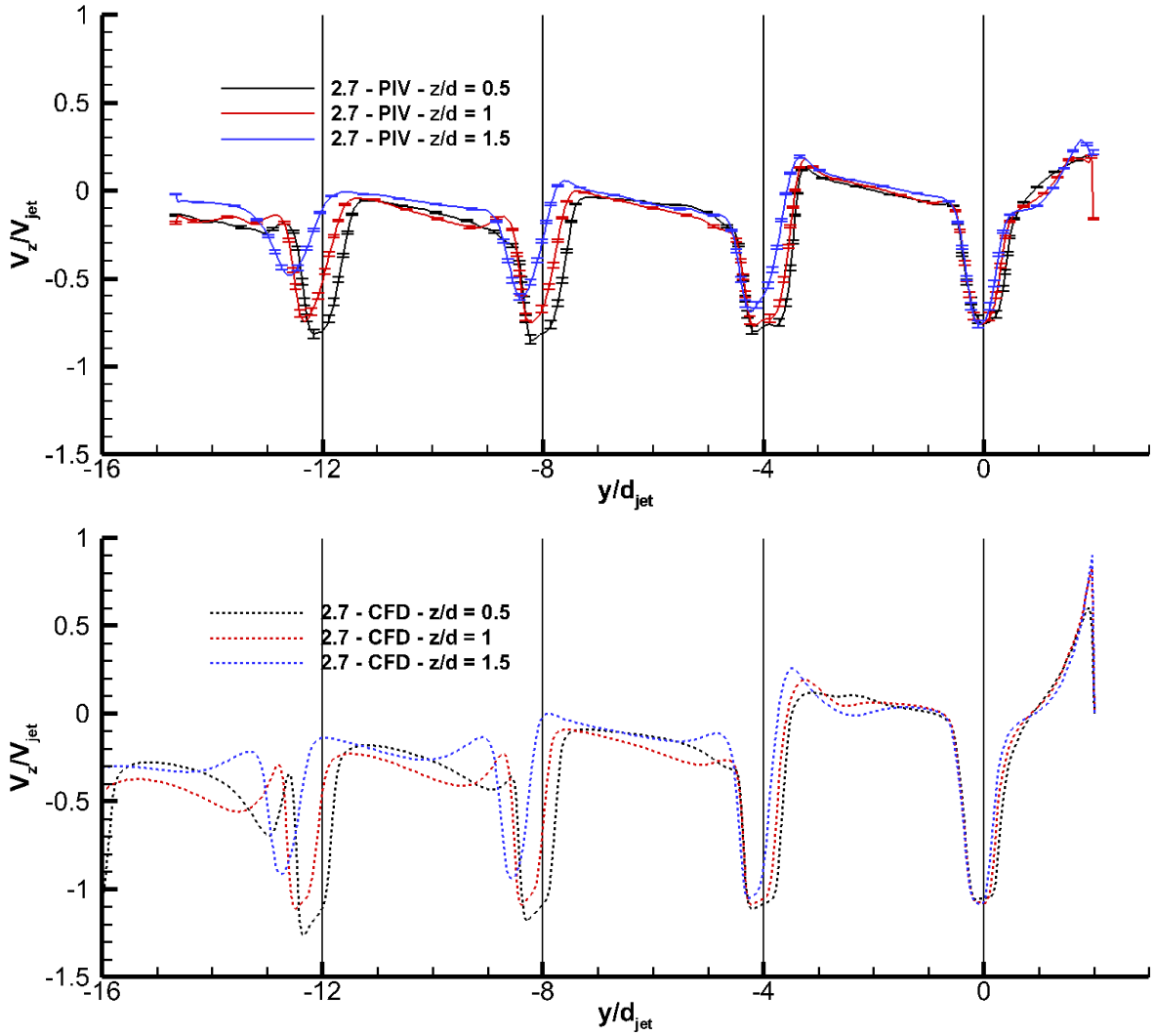

Figure 37: Axial velocity at wall normal locations for H/d = 2.7:
PIV (top), CFD (bottom)

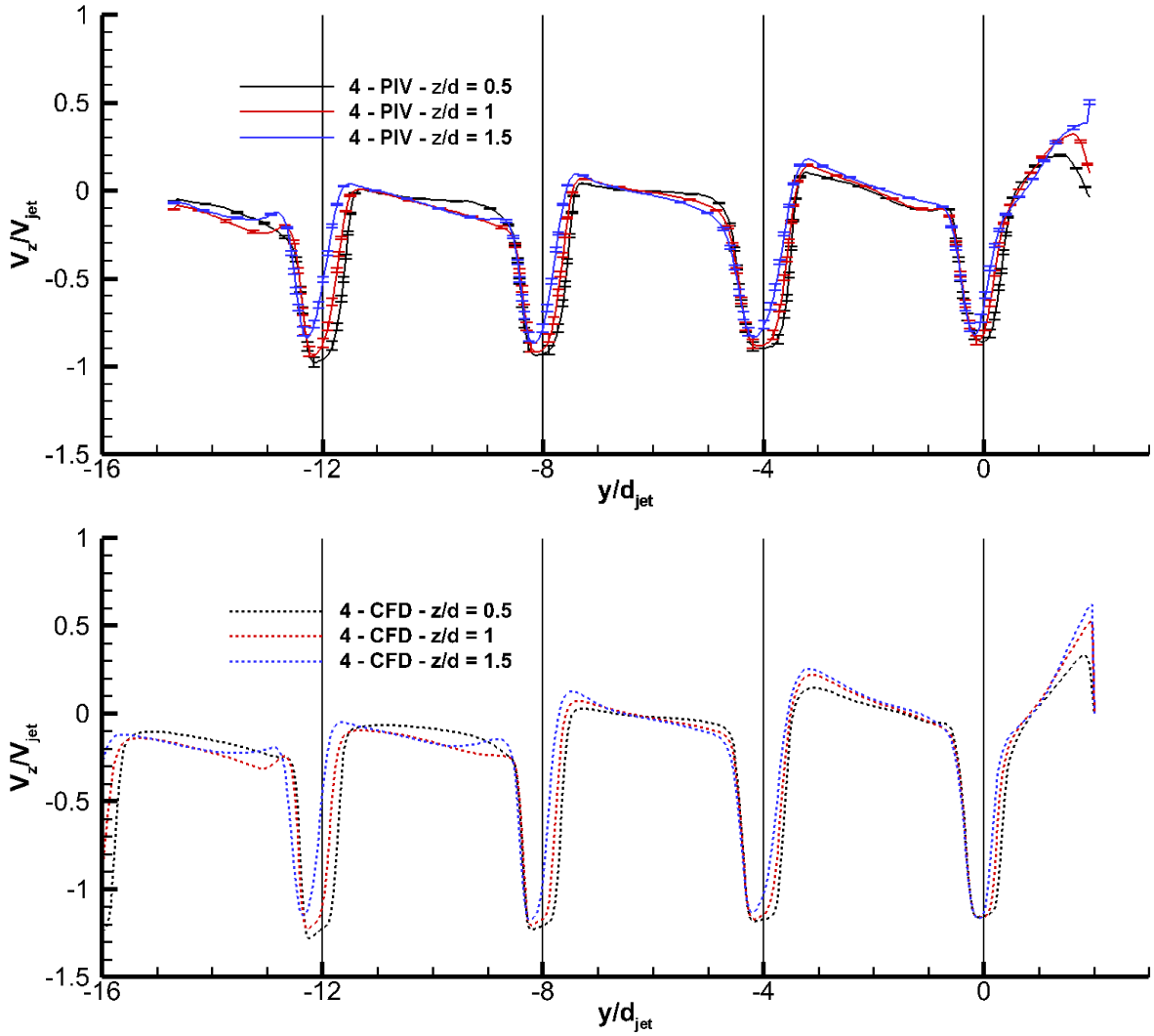

Figure 38: Axial velocity at wall normal locations for H/d = 4:
PIV (top), CFD (bottom)

In Figure 39 the two geometrical configurations are plotted against each other to see the effect of H/d on the axial velocity. Close to the wall at z/d = 0.5, Figure 39 (top), the axial velocities follow identical trends, however the velocity of the H/d = 4 configuration is higher at every jet. At the next wall normal distance, z/d = 1 Figure 39 (middle), the difference in the axial velocities begin to show at the latter jets. The H/d = 2.7 configuration incurs a much larger jet bending effect beginning at the 3rd jet; this is in agreement with the contour plots of Figures 31 and 32. This weaker potential core and larger peak shift is associated with the overall larger bulk velocity present in this configuration. At the last wall normal position, z/d = 1.5 Figure 39 (bottom), the effects of the crossflow and jet bending are even more prevalent at the 3rd and 4th jets. However, the first two jets exhibit little change between what was seen at wall normal distance z/d = 0.5.

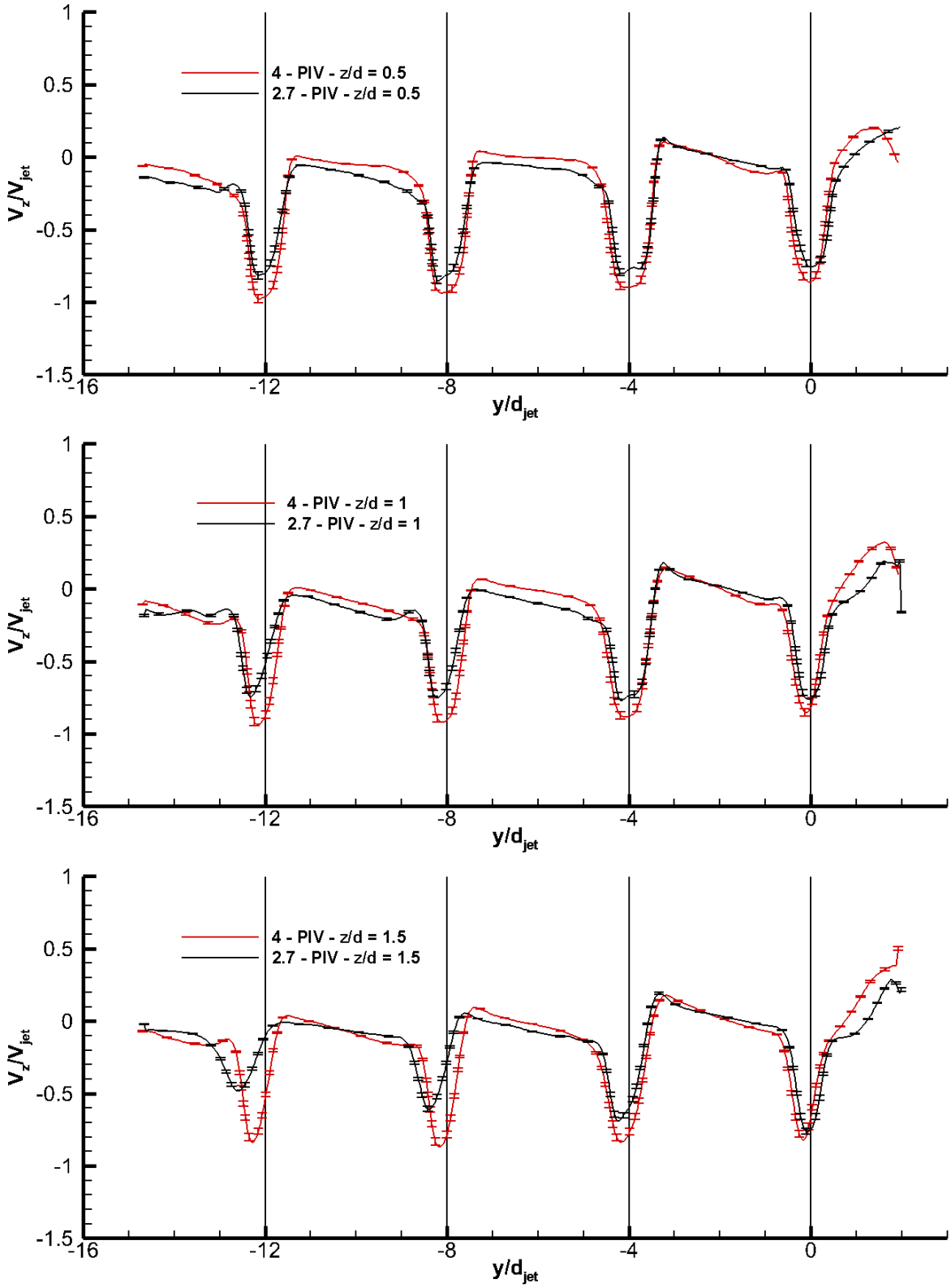

Figure 39: Comparison of axial velocity at wall normal distances for H/d = 2.7 and H/d = 4: z/d = 0.5 (top), z/d = 1 (middle), z/d = 1.5 (bottom)

8.1.3 - Jet Centerline Axial Velocity

To further characterize each individual jet, plotting the axial velocity along the jet centerline helps quantify the entirety of the jet from the orifice to the target surface. Doing so gives context to how far the potential core extends, along with when the jet bends away from the centerline. Figure 40 below shows the locations of the jet centerline location at which the axial velocities are plotted. For this section all of the Reynolds numbers were examined.

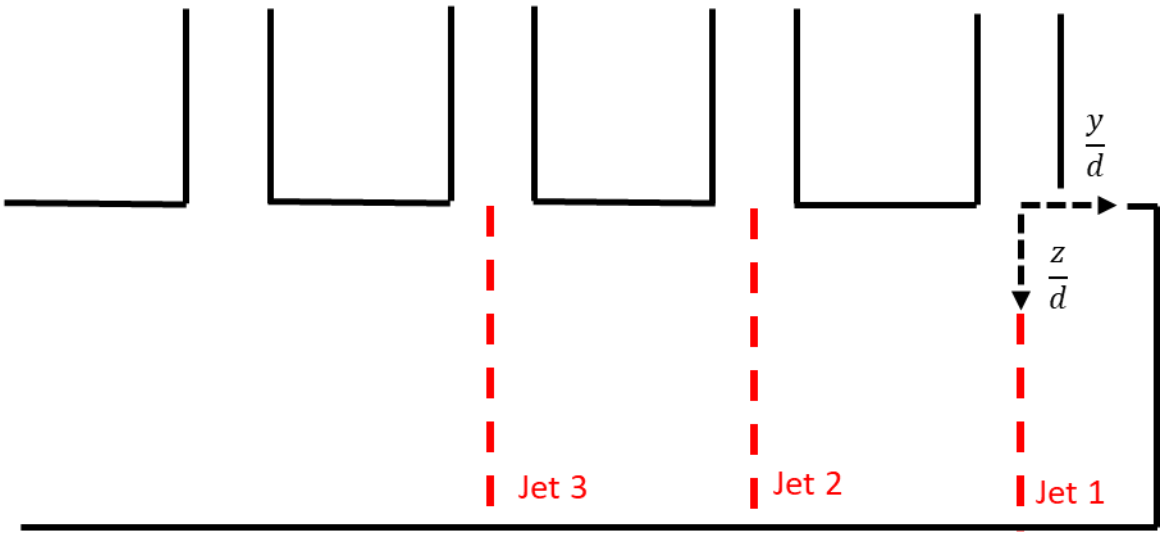

Figure 40: Location of jet centerline plots

Only the axial velocity of the first 3 jet centerlines are investigated. The 4th jet's centerline axial velocity was not investigated as the crossflow begins dominating by the 3rd jet. From what was seen in the velocity contour plots and in the wall normal axial velocity plots an inference of the quickly dissipating potential core at the jet centerline of the 4th jet, and subsequent jets, can be made.

8.1.3.1 - Jet 1

The 1st jet has little, if any crossflow effect and thus has a jet profile similar to a single impinging jet. Figure 41 shows the centerline axial velocity at the 1st jet for geometry H/d = 2.7 and H/d = 4. In the H/d = 2.7 configuration, Figure 41 (top), the potential core is preserved for z/d < 1.5, and then begins to decay linearly due to shear layer. The jet maintains an axial velocity component until the target surface, H/d = 2.7, indicating that the jet impinges at the stagnation point y/d = 0. The jet in the H/d = 4 configuration, Figure 41 (bottom), also preserves its potential core throughout z/d < 1.5. However the rate at which the velocity diminishes after is much slower before stagnating at y/d = 0. Overall both geometries have an axial velocity V_z/V_{jet} = -0.8 at the potential core.

When normalized the experimental plots for the different Reynolds numbers do not collapse as expected, instead they split into two groups, Re = 20,000/40,000 and Re = 60,000/80,000. This was seen in the contour plots of Figure 30, and will be discussed later.

For both geometrical configuration the RANS model struggles to accurately capture the flow field. While the trends are similar, the axial velocity is grossly overpredicted. This is attributed to the vena contracta discussed previously and will be a reoccurring finding throughout all of the jets.

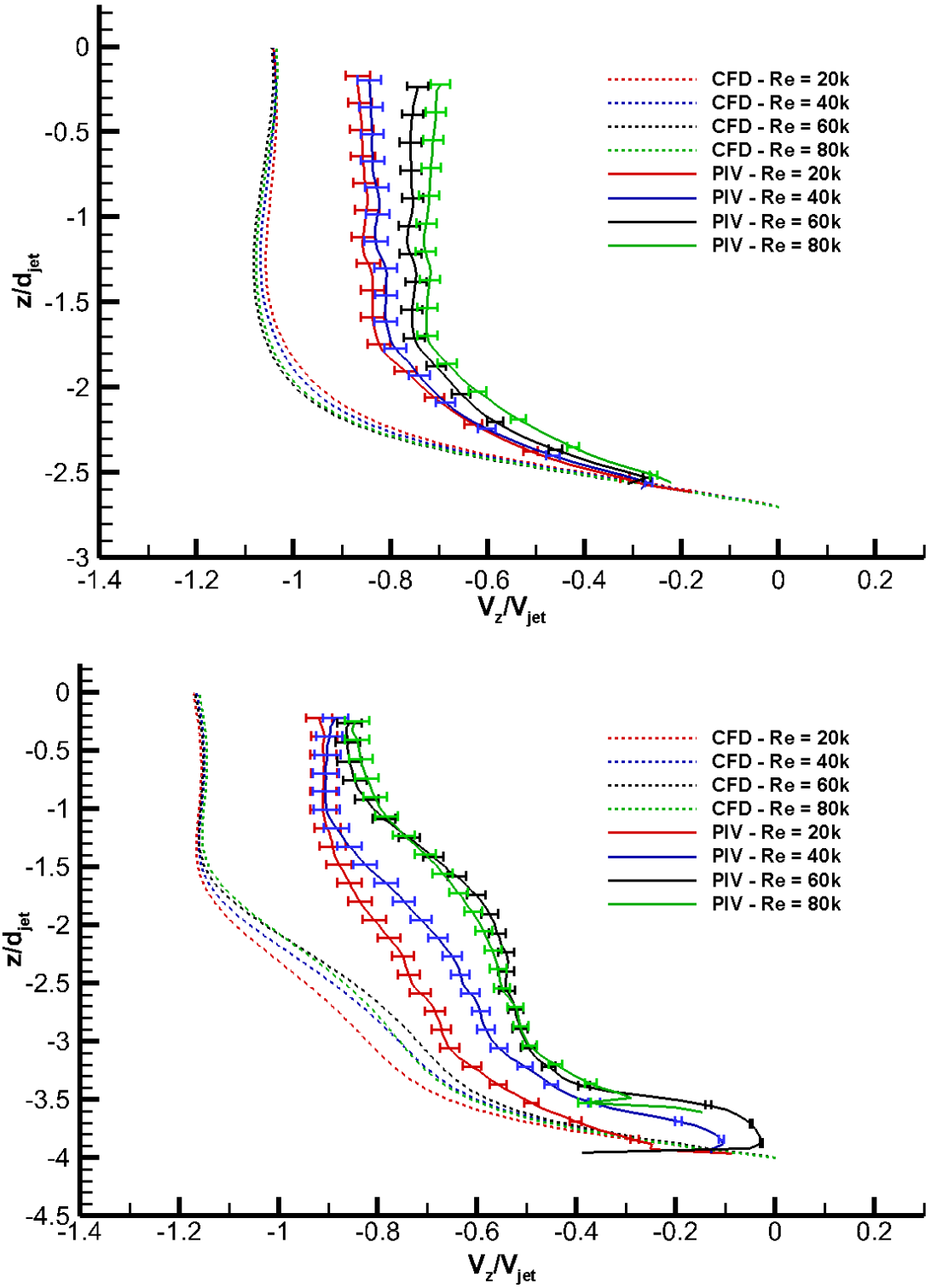

Figure 41: Axial velocity along the jet centerline of jet one (y/d = 0): H/d = 2.7 (top), H/d = 4(bottom)

8.1.3.2 - Jet 2

Figure 42 shows the jet centerline axial velocities for H/d = 2.7 and H/d = 4 at the 2nd jet. The experimental data for both geometries shows that the potential core is fully preserved for z/d < 1 and then diminishes until the stagnation region velocity approaches zero. The decay of the potential core in the H/d = 2.7 configuration is much faster than that of H/d = 4 configuration as seen in the 1st jet. This is due to a mix of the increased crossflow and the shorter distance in which the jet has to decelerate.

Once again the RANS model doesn't accurately capture the flow field of the impinging jet. The velocity is overpredicted at the higher z/d's, and then an upwash is present near the stagnation point in Figure 42 (top). This positive axial velocity is due to the horseshoe type vortex behind the 2nd jet and is not seen in the experimental plot of the axial velocity. In the experiment this vortex was present but the axial location wasn't at y/d = -4 directly below the 2nd jet.

In Figure 41 (top) the experimental data didn't collapse when normalized, and we see that again in Figure 42 (top). However, this time both the experimental and numerical data collapse into two sub groups when normalized. This is possibly due to a different flow field developing at the higher Reynolds numbers than the lower Reynolds numbers.

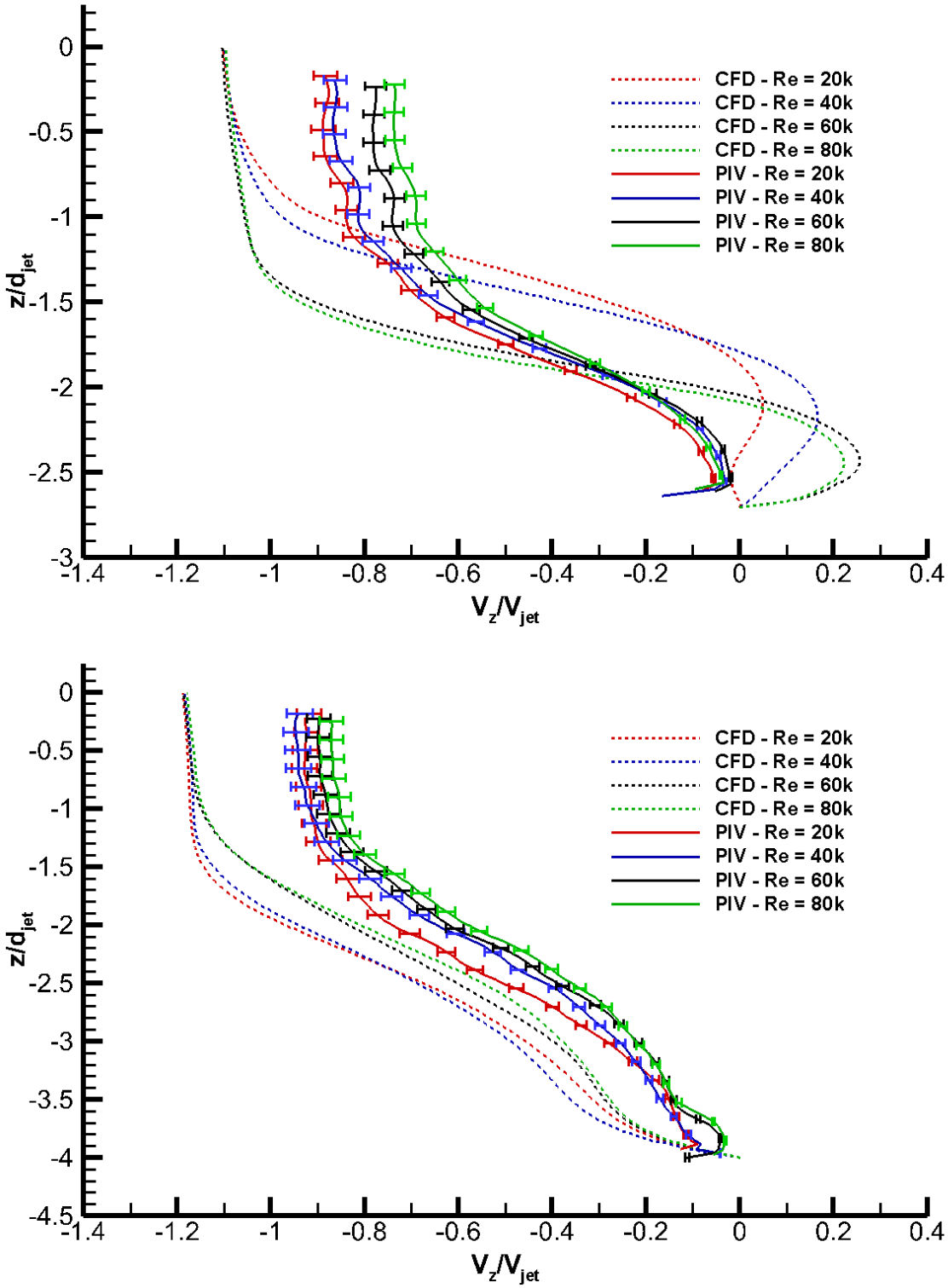

Figure 42: Axial velocity along the jet centerline of jet two (y/d = -4): H/d = 2.7 (top), H/d = 4(bottom)

8.1.3.3 - Jet 3

At the 3rd jet the crossflow has a noticeable effect on the stagnation velocity. This can be seen in Figure 43 (top) where the experimental axial velocity is zero at z/d ≈ 1.8; in Figure 43 (bottom) the experimental axial velocity is zero at z/d ≈ 3. This zero velocity shows that below these z/d locations there is little to no axial velocity and the velocity magnitude is dominated by the streamwise velocity component. This streamwise dominated velocity is an indication that the potential core of the jet is bent and the stagnation region, if there is one, has been shifted downstream. This visible bending in the jet centerline axial velocity supports the jet bending associated with the peak shifts seen at the 3rd jet in the wall normal axial velocity plots previously, Figures 36-39.

For both geometries the trend of numerical data is in good conjunction with that of the experimental data. Once again the RANS model overpredicts the initial jet velocity at z/d = 0, but now with the effect of crossflow it also overpredicts the crossflow. Overall the numerical data matches the experimental data much better in the crossflow dominated regions than in the potential core.

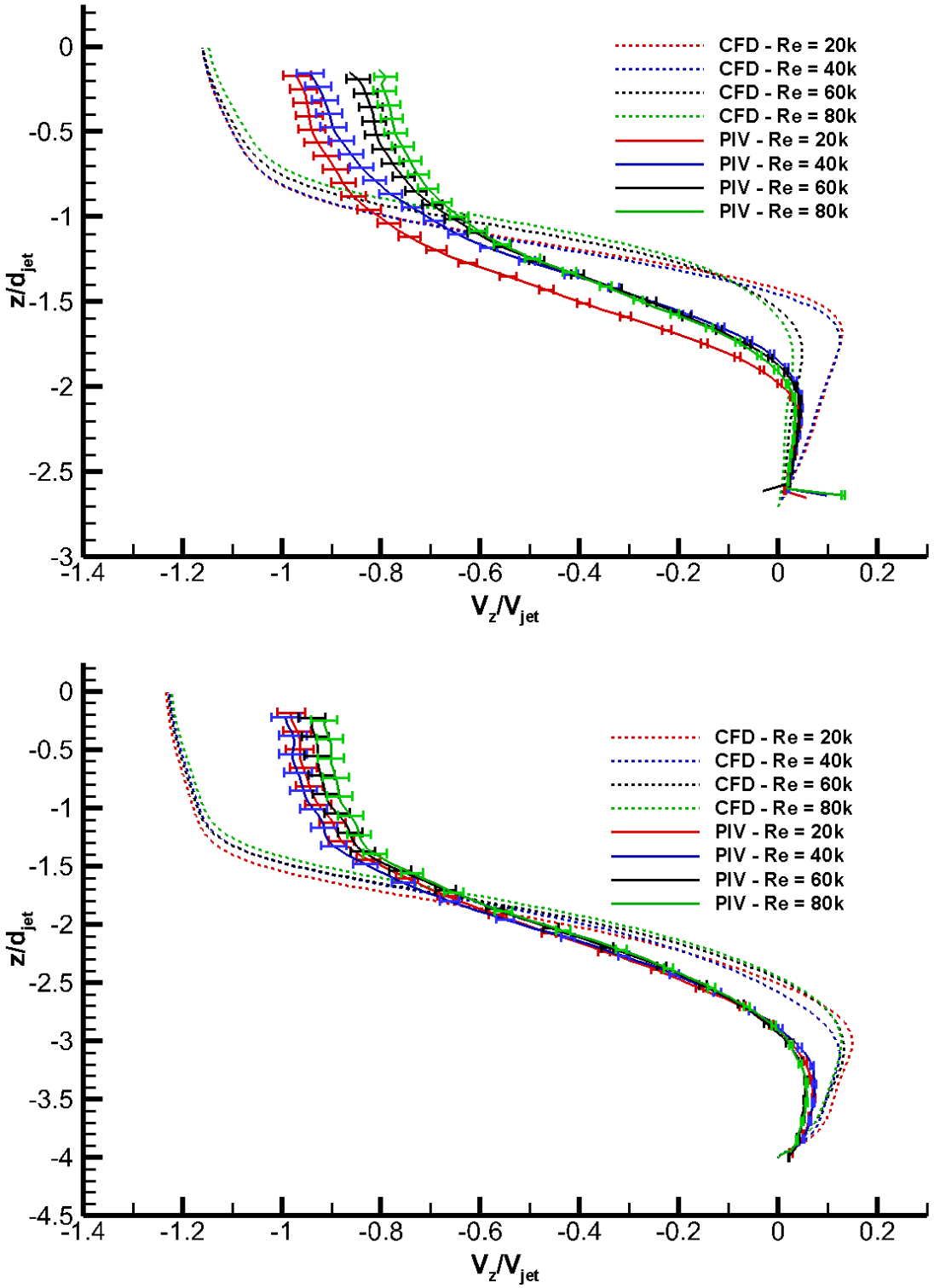

Figure 43: Axial velocity along the jet centerline of jet three (y/d = -8): H/d = 2.7 (top), H/d = 4 (bottom)

8.1.4 - Streamwise Velocity at Different Streamwise Locations

To investigate how the crossflow develops within the test section the streamwise velocity was plotted at several streamwise locations on the jet centerline plane. These plots also give a quantitative look at how the boundary layer flow along the curved target surface builds. The three streamwise locations at which the streamwise velocity is plotted are: y/d = -2, -6, -10. These locations correspond to the streamwise midpoint between jets 1-2, jets 2-3, and jets 3-4 respectively. Figure 44 below shows the streamwise locations at which the velocity is taken. The streamwise velocities were normalized by [Eq. 34].

$$\frac{V_y}{V_{jet}} \qquad [34]$$

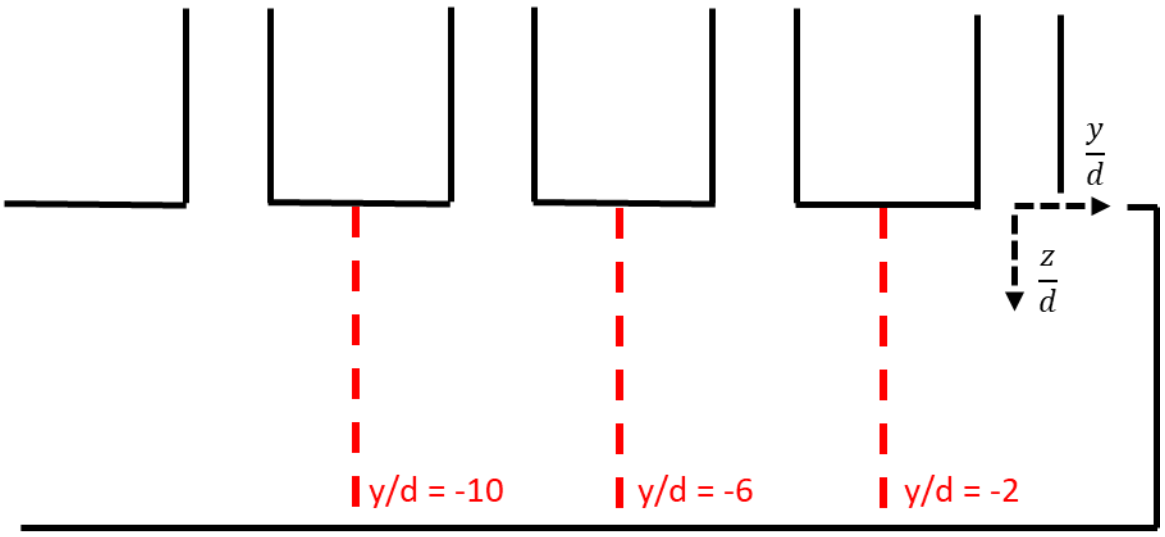

Figure 44: Location of streamwise plots

8.1.4.1 - y/d = -2

Since there is only one jet upstream from y/d = -2 the crossflow at this location is expected to be minimal. From the previous data seen the 1st jet acts as a free impinging jet with no crossflow and thus creates a stagnation region and wall jet regions.

As seen in Figure 45, there is very little streamwise velocity at this streamwise location for the two configurations. In both plots an appreciable streamwise velocity can be seen near the target surface. This velocity is attributed to the wall jet region that is formed after the 1st jet impinges. This wall jet region quickly loses axial velocity as the distance from the target surface increases; losing a majority of its magnitude by roughly ~1 z/d above the target surface in both configurations. Near z/d = 0, the polarity of the velocity shifts. This positive streamwise velocity indicates that the flow is moving upstream at this location. The positive streamwise velocity is caused by the large recirculation between the 1st and 2nd jets which is seen in the contour plots.

At this location the RANS model does a decent job at predicting the streamwise velocity in both configurations. There is a slight overprediction in the wall jet region which is likely due to the overprediction of the axial velocity of the jet as the wall jet region is a direct function of the impinging jet itself. One interesting note is that the numerical results of the H/d = 2.7 configuration fails to converge when normalized.

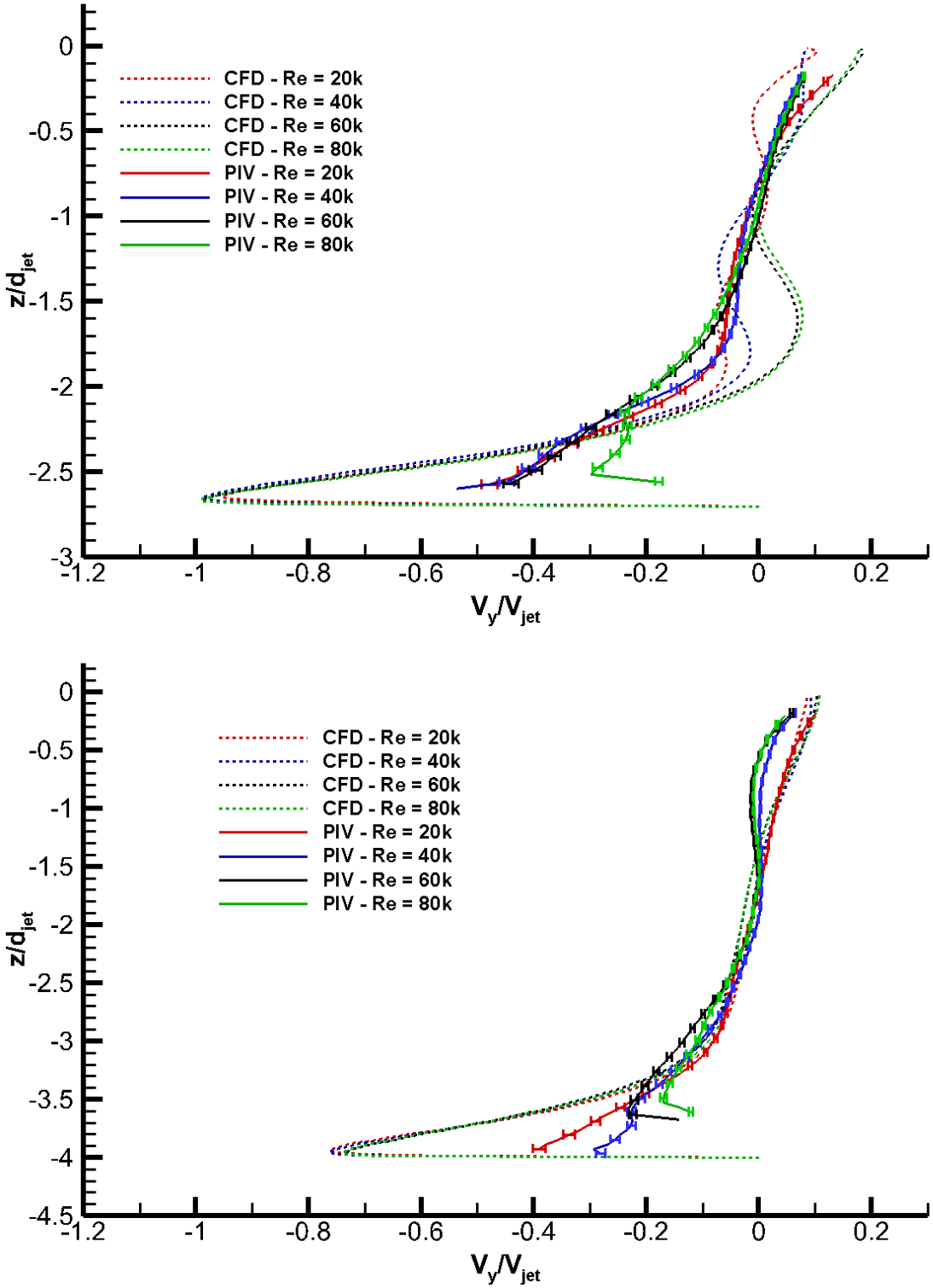

Figure 45: Streamwise velocity at y/d = -2:
H/d = 2.7 (top), H/d = 4 (bottom)

8.1.4.2 - y/d = -6

At streamwise position y/d = -6, located between the 2nd and 3rd jet, the crossflow velocity begins to increase at all z/d locations. At the previous location of y/d = -2 there was no significant streamwise velocity component located ~1 z/d above the target surface, this is not the case at y/d = -6 as there is a weak streamwise velocity component near the jet orifice (z/d = 0).

Figure 46 (top) shows the streamwise velocity component at y/d = -6 for the H/d = 2.7 configuration. The streamwise velocity along the target surface is noticeably stronger. At the previous location the $V_y/V_{jet} \approx 0.4$ while at this streamwise location $V_y/V_{jet} \approx 0.5$. This shows that the fluid region along the curved surface is increasing in velocity. However the thickness of this fluid region along the curved surface remains relatively unchanged.

Figure 46 (bottom) shows the streamwise velocity component at y/d = -6 for the H/d = 4 configuration. Unlike the H/d = 2.7 configuration, the streamwise velocity components remain relatively unchanged. This is supported by the previous data that in this configuration the 2nd jet experiences little to no jet bending as there is less crossflow. In comparison to the H/d = 2.7 configuration the streamwise velocity is slower, which supports the previous claim of the increased bulk velocity in the H/d = 2.7 configuration.

The RANS model at this location predicts free-stream streamwise velocity fairly well. However, it once again fails to capture the boundary layer flow along the target surface.

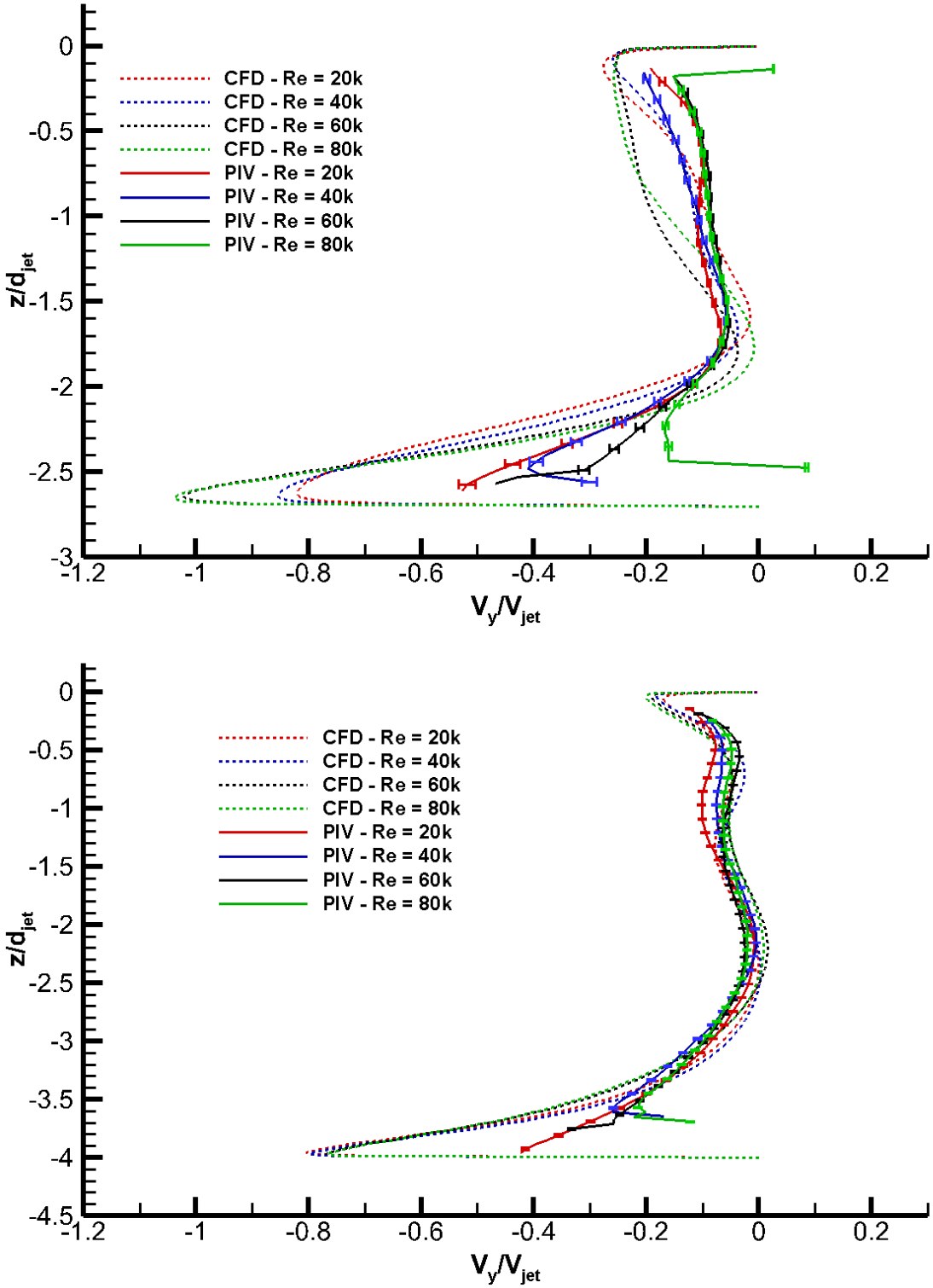

Figure 46: Streamwise velocity at y/d = -6:
H/d = 2.7 (top), H/d = 4 (bottom)

8.1.4.3 - y/d = -10

At steamwise position y/d = -10 the crossflow has begun to build, now consisting of the spent mass from the three upstream jets. This has caused the whole profile of the streamwise velocity to change. The overall streamwise velocity is faster, the wall fluid region has begun to increase in thickness, and wall normal distances where the streamwise velocity was negligible at previous streamwise locations now have a large streamwise velocity component.

Figure 47 (top) shows the streamwise velocity component at y/d = -10 for the H/d = 2.7 configuration. Compared to the previous streamwise position the wall surface fluid is faster and thicker. The $V_y/V_{jet} \approx 0.6$ showing a continuing increase in cross flow velocity. More interestingly is the growing thickness of this wall fluid region. The wall fluid region extends ~0.8 z/d above the target surface, whereas at previous streamwise locations it didn't extend more than ~0.4 z/d. The crossflow also has an appreciable velocity up until ~1.5 z/d above the target surface.

The H/d = 4 configuration (Figure 47 (bottom)) doesn't see a large velocity increase in the wall jet fluid compared to the previous streamwise location, but the thickness of this fluid region does increase. The overall thickness for this wall fluid region has increased to a thickness of ~1 z/d off the target surface, while an appreciable streamwise velocity component is present up until ~2 z/d off the target surface.

By the streamwise location y/d = -10 the flow begins to become dominated by the crossflow for both configurations. At each subsequent streamwise location a stronger streamwise velocity was seen at both the target surface and along the jet orifice. Overall the streamwise velocities of the H/d = 2.7 configuration increased considerably faster than those of the H/d = 4 configuration, supporting the increased jet bending effects in the H/d = 2.7 configuration seen in the previous sections. Should more streamwise locations be examined it would be expected that the boundary

layer at the target surface continues to increase in both velocity and thickness, and the overall streamwise velocity component at all wall normal distances increases.

The trends seen in the experimental PIV results are also seen in the RANS model even though it once again overpredicts the near wall flow. There is little change in the max streamwise velocity of the numerical results at this location compared to the previous, but there is a large increase in the thickness of the wall jet region. This consistent overprediction by RANS model has been seen at all streamwise locations, further showing that the RANS model is incapable of properly modeling the complex fluid interactions within the leading edge impingement array.

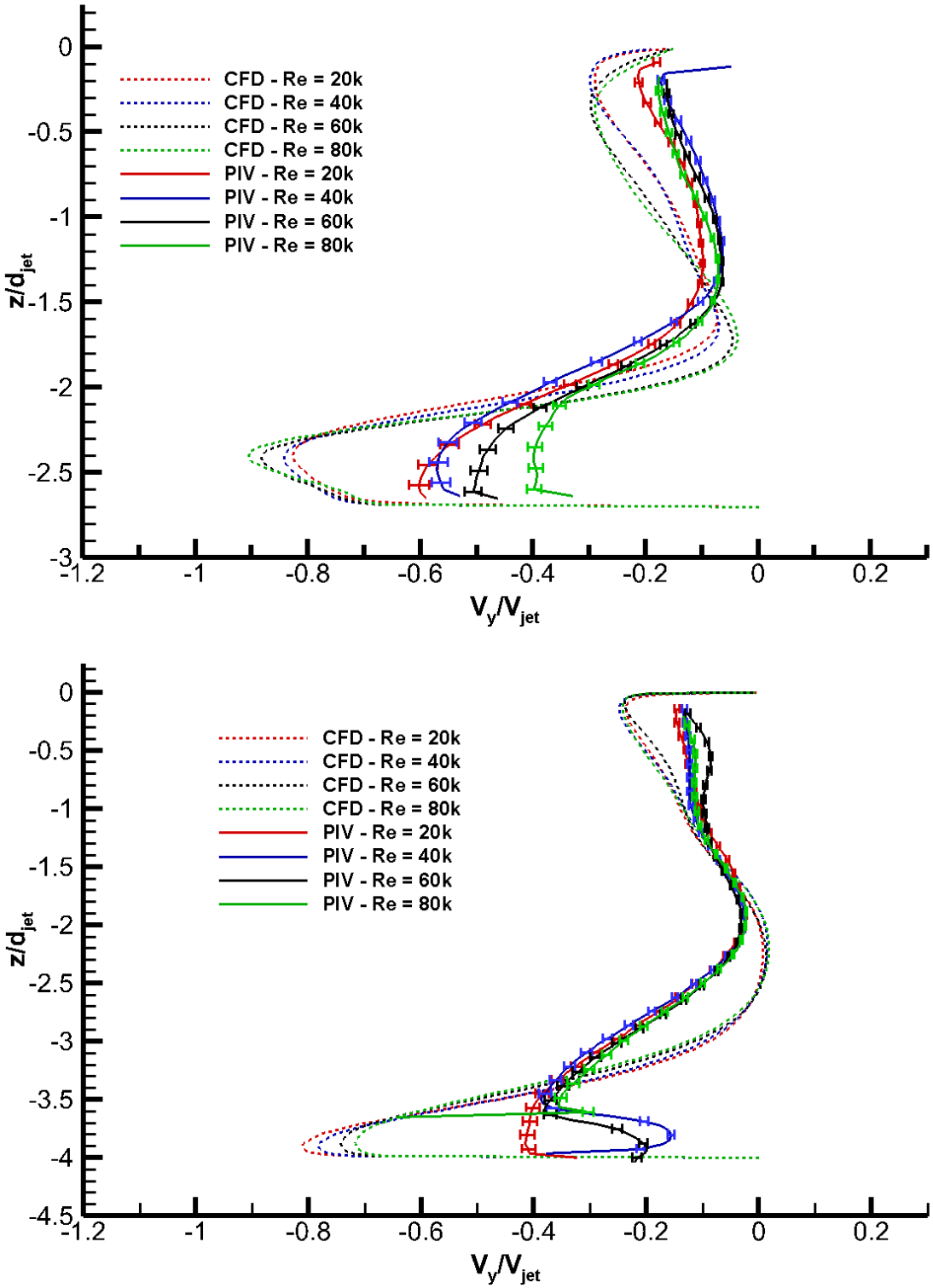

Figure 47: Streamwise velocity at y/d = -10:
H/d = 2.7 (top), H/d = 4 (bottom)

8.1.5 - Further Flow Field Investigation

Various vortices and flow structures were recognized previously, such as in the velocity contour plots. This section strives to further investigate these portions of the flow field as they cannot be easily quantified within a 2D coordinate system. To do so, the ability to generate 3D renderings within StarCCM+ is utilized to qualitatively look at these flow structures.

These vortices were first identified through their Q-criterion, and then also visualized with streamlines. The Q-criterion is a well-accepted method of vortex identification, as it compares the shear strain rate to the vorticity magnitude, and a Q-criterion >>0 represents a local vortex where the vorticity magnitude is greater than the rate of strain [Holmén, 2012]. The overall shape of the vortices can then be visualized with an isosurface of Q-criterion.

8.1.5.1 - Vortex at y/d = -4

The first vortex investigated was the one located behind the 2nd jet at y/d ≈ -4. This vortex appeared through the Q-Criterion isosurface, Figure 48, and spans across from the suction side to the pressure side of the leading edge.

In Figure 49 the vortex is visualized by seeding the local region with streamlines. The assumption previously that the 1st and 2nd jets contribution to the formation of this vortex is supported in both H/d configurations. However the direction of the vortices between the two configurations are different. In the H/d = 2.7 configuration the fluid within the vortex crosses from the pressure side to the suction side of the leading edge, this effect is visible in Figure 49 (left). At H/d = 4 the vortex doesn't have a definitive direction in which the fluid moves.

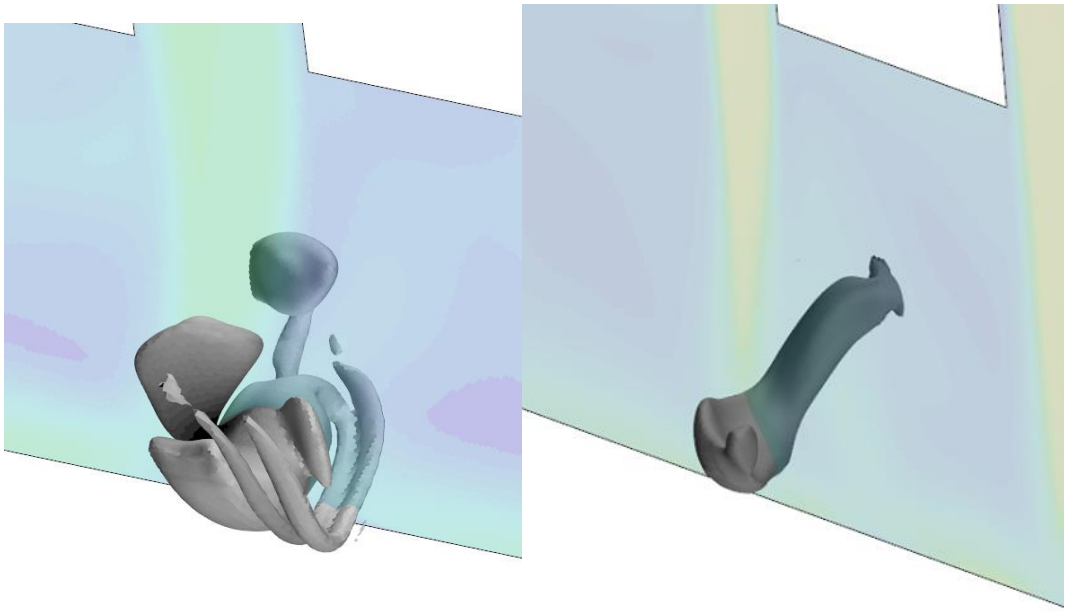

Figure 48: Isosurface of Q-criterion of the vortex at y/d = -4:
H/d = 2.7 (left) , H/d = 4 (right)

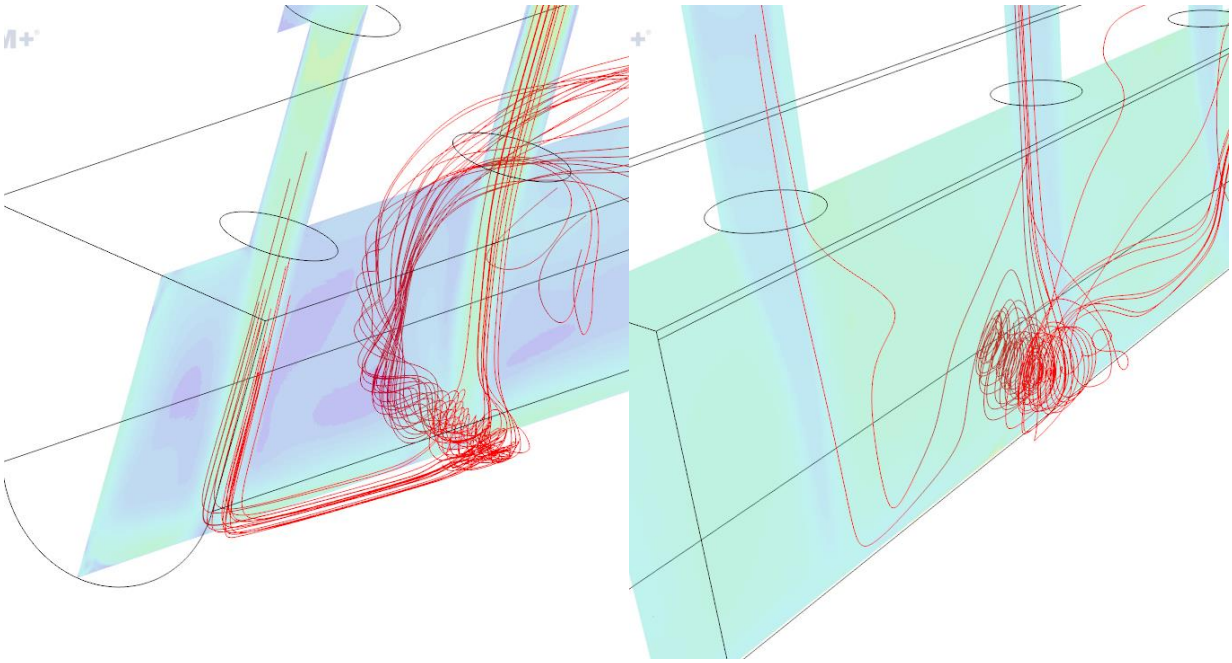

Figure 49: Streamlines of the vortex at y/d = -4:
H/d = 2.7 (left) , H/d = 4 (right)

8.1.5.2 - Vortex at y/d = 1

The vortex upstream of the 1st jet was also visualized, however it was too weak to appear through a Q-Criterion isosurface. This indicates that the vortex is relatively weak; it was still modeled with streamlines in Figure 50 below. This vortex is formed by the recirculation along the back wall at y/d = 2, and as noted previously the recirculation is strongest at H/d = 2.7. This is also the case in Figure 50. The recirculation at H/d = 4 is much more spread out across the entirety of the leading edge volume, while at H/d = 2.7 the recirculation is held to a tight centralized region.

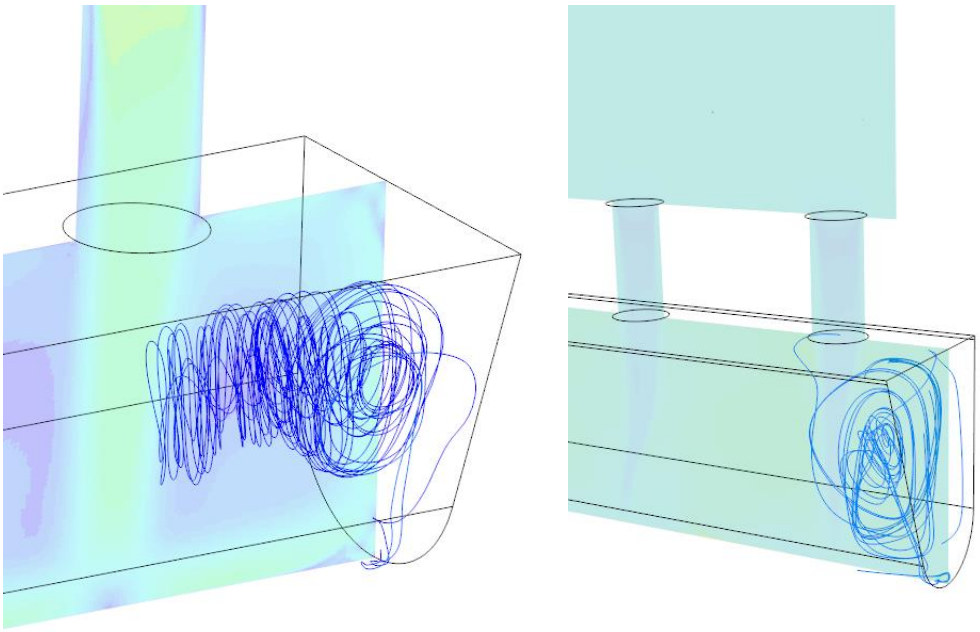

Figure 50: Streamlines of the vortex at y/d = 1:
H/d = 2.7 (left) , H/d = 4 (right)

8.2 – Heat Transfer Results

The following section will present and discuss the heat transfer portion of this investigation. The primary investigation of the area average heat transfer is presented first, examining both the experimental and numerical results. Following, contour plots of the local Nusselt number taken from numerical simulation help better highlight localized areas of high/low cooling, of which can be attributed to the larger area averaged cooling. Lastly the spanwise lateral average of the Nusselt number is presented. For the purpose of this study the Nusselt number was normalized by [Eq. 35]. The exponent '0.85' was chosen according to the statistical distribution of the exponent in the power law curve of Nusselt as a function of Reynolds number for each block experimentally. Further, this exponent was used to normalize the data in Brakmann (2017).

$$\frac{\mathrm{Nu}}{\mathrm{Re}^{0.85}} \qquad [35]$$

8.2.1 - Area Average Heat Transfer

The first method that was used to look at the heat transfer was through an area average of each block. This area averaged data shows the macro level heat transfer occurring at different parts of the leading edge along with overall trends of the heat transfer. One such trend that is expected is a gradually higher heat transfer at each subsequent jet due to the increases crossflow downstream.

8.2.1.1 – Brakmann (2017) Comparison

The heat transfer data was initially compared to that of Brakmann (2017) to help validate the results as the geometry in this study was designed after that of Brakmann (2017). This comparison was done at Re = 20,000 and H/d = 2.7 to match the dimensionless parameters exactly. To compare the results of Brakmann (2017), their lateral average data was interpolated in MATLAB to achieve an area average. This area average accounts for the pressure side, curved wall, and suction side of each jet. In this study, the area average of these three blocks were properly averaged to achieve this new 'section average' area average. Figure 52 below compares this section average Nusselt numbers of these two studies.

Upstream, at sections 1 and 2, the experimental data of Brakmann (2017) does not match at all; downstream at section 3, 4, and 5 the two datasets are in better agreement when the cross flow is dominant. This divergence in the results upstream is due to the differences in the overall geometry of the test section. The most apparent difference is the film cooling holes which are absent in this study. These film cooling holes reduce the amount of crossflow and cause less jet bending, especially for the 3rd jet. Another slight difference that has a big impact is that the fluid volume of Brakmann (2017) extends upstream from the 1st jet to y/d = 4, where as in this study it only extends to y/d = 2. This greatly reduces the recirculation effect seen upstream of the 1st jet and less cooling in this location overall.

The computational results of Brakmann (2017), along with those of this study, are in good agreement with the experimental results of this study.

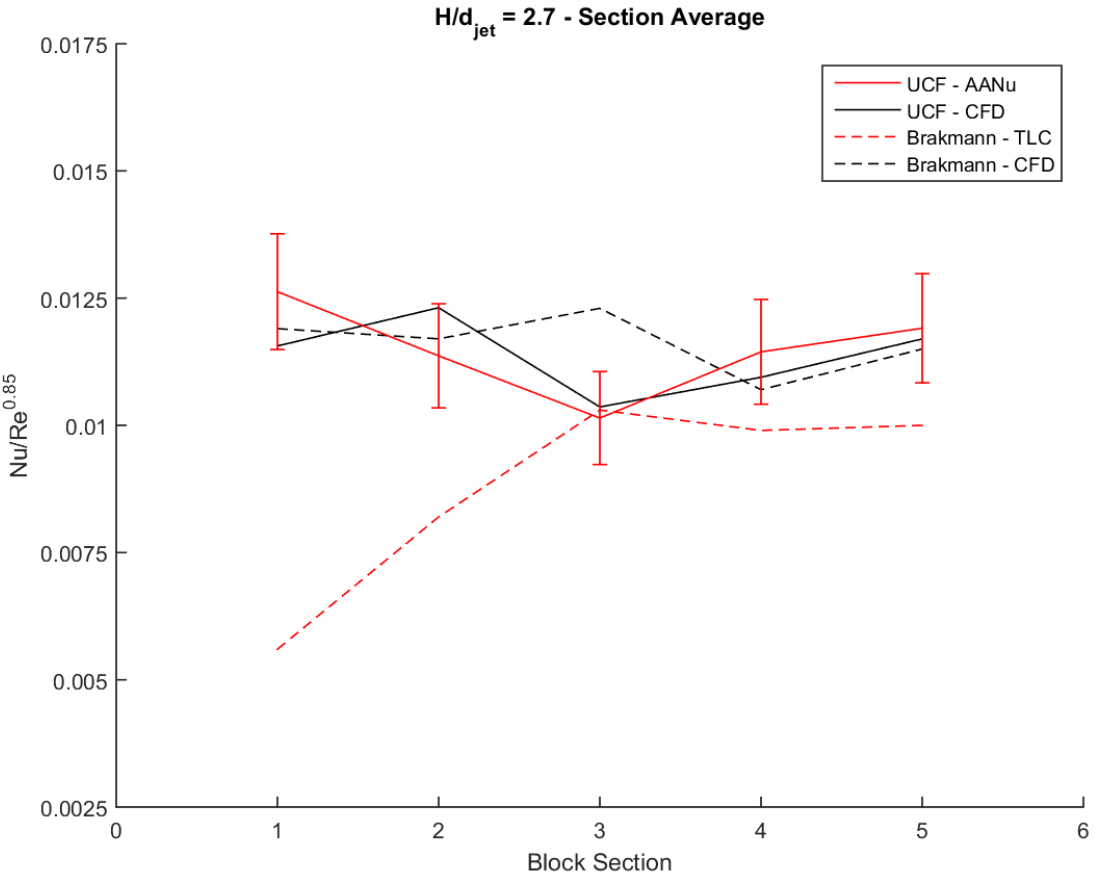

Figure 51: Comparison of area averaged Nusselt number results to Brakmann (2017)

8.2.1.2 - H/d = 2.7

In the H/d = 2.7 configuration there were three copper block walls open to flow: Suction Side Bottom (SS Bottom), Curved, and Pressure Side Bottom (PS Bottom). Figures 52 through 54 graph the block section versus the non-dimensional Nusselt number for both experimental and numerical data.

The experimental area average Nusselt number for the 'SS Bottom' wall, Figure 52, is in excellent agreement with the numerical results. The 1st jet has one of the highest Nusselt numbers which is expected as there is little jet bending; however, there is a large detriment at the following

block in section 2. This detriment is unexpected as the vortex located near y/d = -4 would be expected to increase the heat transfer, as seen in the numerical results. Following the 2nd block, there is a steady increase as the block sections proceed further downstream. This increase concludes with the final block's Nusselt number matching that of the 1st block. This gradual increase in Nusselt number infers that the heat transfer occurring at the downstream blocks shows that the 3rd, 4th, and 5th blocks are purely dominated by the crossflow. The 'PS Bottom' wall is the worst preforming block in terms of heat transfer by a large margin when compared to the other walls.

The 'Curved' wall area average heat transfer trend differs from the other walls in that as crossflow increases there is a degradation in heat transfer. The highest heat transfer is located at the 1st block, and then gradually declines until the lowest heat transfer occurs at the 4th block as seen in Figure 53. This is due to the lack of a stagnation region and the boundary layer flow as seen in the experimental PIV data. The jet bending downstream prevents this stagnation region heat transfer from occurring resulting in a lower Nusselt number compared to the 1st and 2nd blocks. The boundary layer also plays a role, as more heat is convecting from the surface there is no way for this hot air to escape due to the lack of mixing; causing the downstream curved blocks to experience a hotter fluid film temperature. The numerical data overpredicts the heat transfer by roughly 20-35%, with the larger differences occurring at the higher Reynolds numbers.

The heat transfer occurring along the 'PS Bottom' wall is plotted in Figure 54 below. While the CFD underpredicts the experimental data at each section, the overall trends match. This trend is similar to that of the 'SS Bottom' wall in that the area average heat transfer increases at each subsequent block section signaling that these blocks are also predominantly dominated by the crossflow. However unlike the other previous sections not all of the data collapses when

normalized. In both the experimental and numerical data there is a large difference in the Nusselt number at the 2nd section between Re = 20k/40k and Re = 60k/80k. The lower Reynolds number grouping outperforms that of the higher Reynolds number. This split in low and high Reynolds number is the same found in the velocities, and this higher heat transfer at the lower Reynolds numbers can thus be attributed to the different flow phenomena found at the lower Reynolds numbers; although this should be taken cautiously as the experimental values are within their uncertainty.

Overall, the area average heat transfer over the H/d = 2.7 configuration are explained extremely well by the jet characteristics. There is high heat transfer at the 1st section due to the potential core extending fully to the stagnation point and the recirculation of the 1st jet upstream, high heat transfer located at 2nd jet where the vortices forms, and the detriment/increase in heat transfer due to the crossflow.

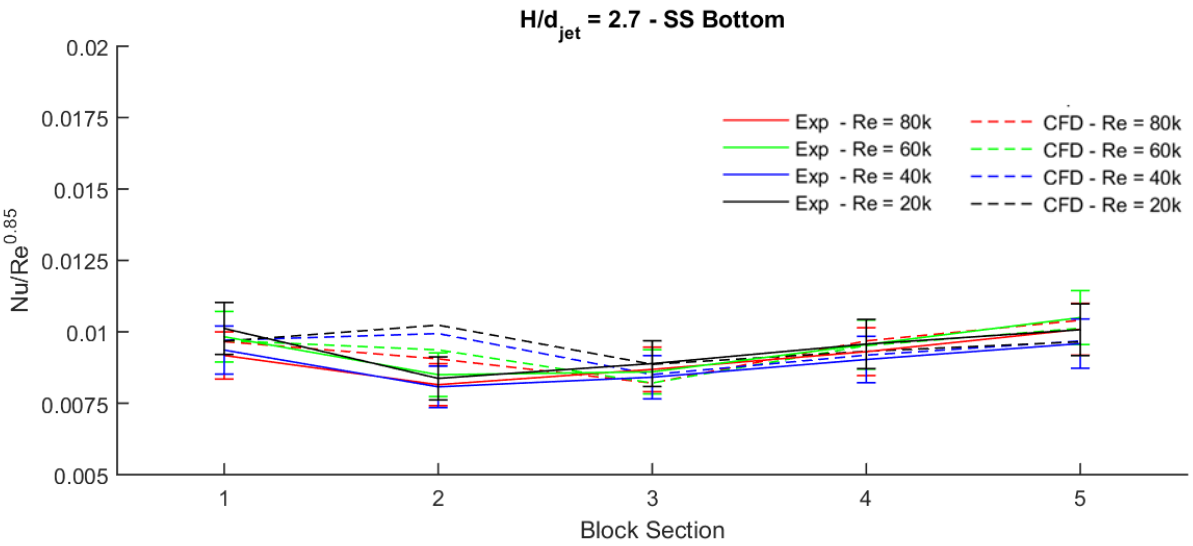

Figure 52: Area average Nusselt number: H/d = 2.7, SS bottom wall

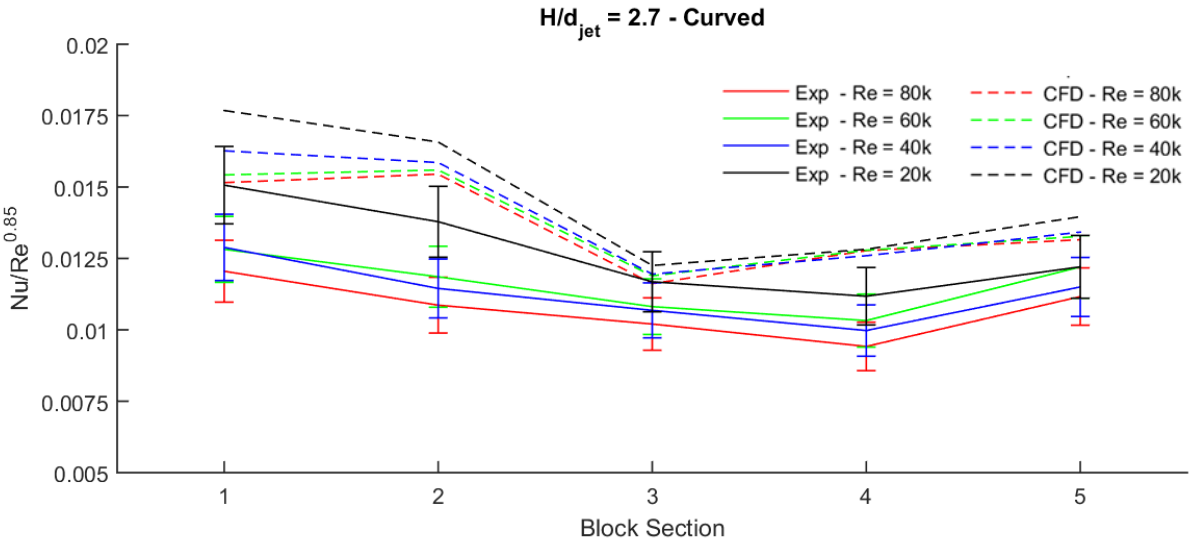

Figure 53: Area average Nusselt number: H/d = 2.7, curved wall

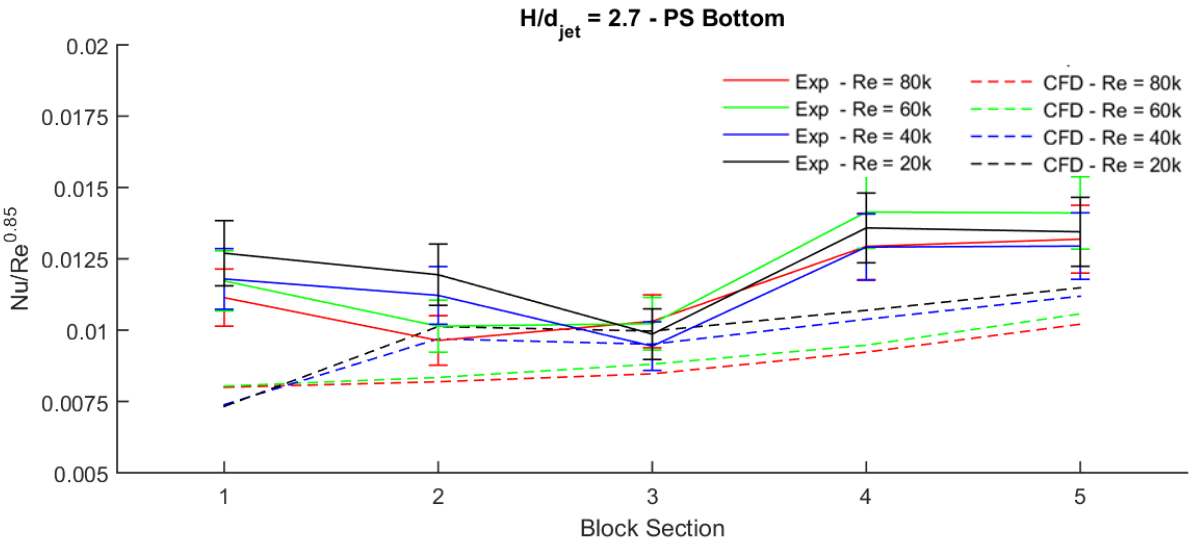

Figure 54: Area average Nusselt number: H/d = 2.7, PS bottom wall

8.2.1.3 - H/d = 4

The H/d = 4 configuration has five different walls open to the fluid flow: the three walls present in the H/d = 2.7 configuration and two extra walls denoted Suction Side Top (SS Top) and Pressure Side Top (PS Top). Figures 55 through 59 below show the normalized Nusselt numbers for each wall at the different block sections for both the experimental and numerical results. Overall both experimental and numerical data sets normalize well.

The suction side wall Nusselt numbers are depicted in Figures 55 and 56. The 'SS Top' and 'SS Bottom' walls both have their highest heat transfer occurring at the 1st jet due to the strong recirculation in the upstream cavity of the 1st jet. The downstream sections of these walls have very different trends present. The 'SS Top' wall sees a decreasing heat transfer rate up until the 3rd section before the trend then slopes back up as the crossflow becomes dominant in the region; while the 'SS Bottom' wall has a relatively constant Nusselt number subsequent location downstream. However, the 'SS Bottom' outperforms the 'SS Top' at every location. This detriment of heat transfer along the 'SS Top' wall is similar to that seen to the detriment found along the 'SS Bottom' wall in the H/d = 2.7 configuration and will be discussed later.

The numerical data for the 'SS Bottom' wall is in excellent agreement with the experimental data at all Reynolds numbers; while the numerical data for the 'SS Top' wall is in good agreement at the 1st jet but then greatly under predicts the heat transfer downstream.

As seen in the 'Curved' wall of the H/d =2.7 configuration, the 'Curved' wall of the H/d = 4 configuration also has a detriment to area averaged heat transfer downstream attributed to lac of stagnation heat transfer and the wall boundary flow as seen in Figure 57. Once again the numerical data overpredicts the stagnation region heat transfer.

The pressure side wall Nusselt numbers are depicted in Figures 58 and 59. Both walls see an increased Nusselt number at each subsequent downstream jet due to the increased crossflow velocity. However the increase in heat transfer due to the crossflow is much higher for the 'PS Top' wall than the 'PS Bottom' wall. The numerical Nusselt results on the pressure side wall is similar to that of the suction side wall. For the 'PS Top' wall the numerical results under predict the experimental, and for the 'PS Bottom' wall the numerical and experimental data are in very good agreement.

Overall the Nusselt number results in the H/d = 4 configuration follow what was expected. One noticeable result is that the suction side and pressure side walls, both top and bottom blocks, follow the same trends. The bottom blocks of each wall have a relatively minimal increase in Nusselt number at each subsequent jet while the top blocks are more effected by the crossflow downstream. This difference between the top and the bottom blocks, on both walls, is because the boundary layer flow thickness at H/d = 4 encompasses more of the bottom walls, as seen previously in the streamlines of Figures 32 and 34 in section 8.1.1.

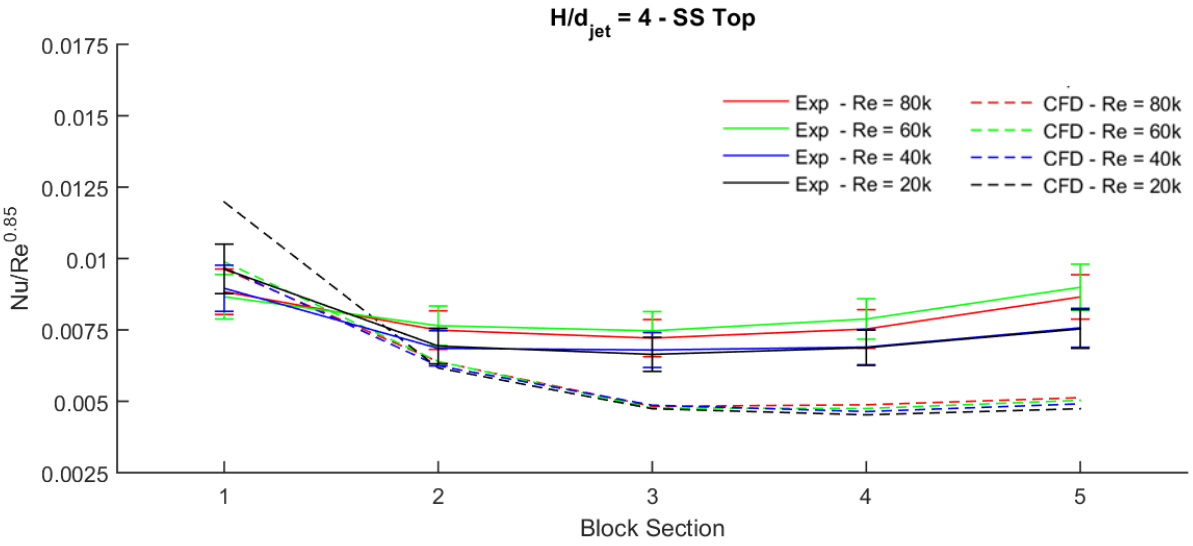

Figure 55: Area average Nusselt number: H/d = 4, SS top wall

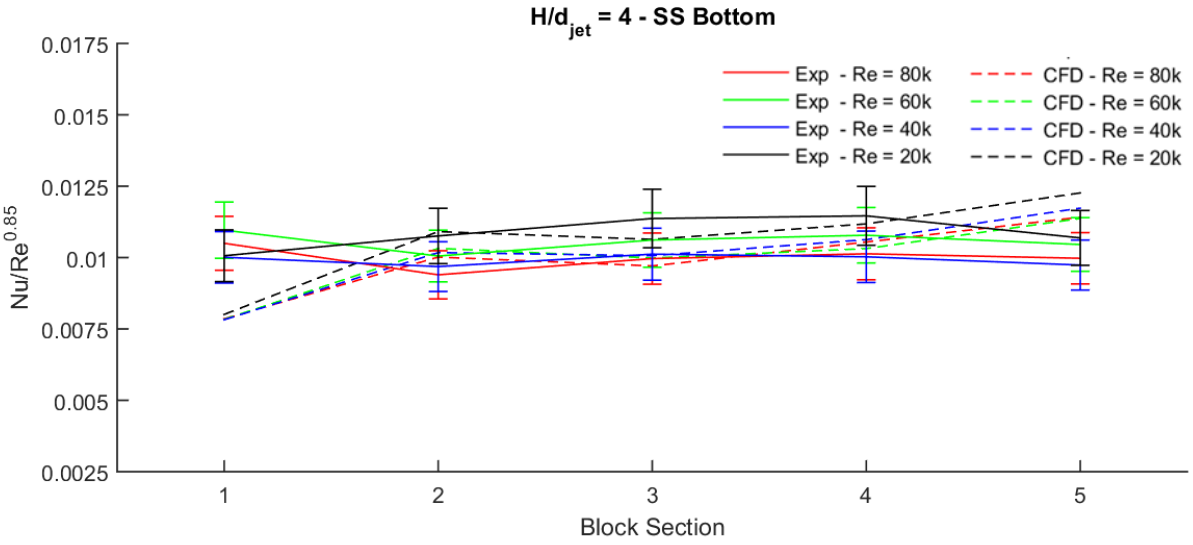

Figure 56: Area average Nusselt number: H/d = 4, SS bottom wall

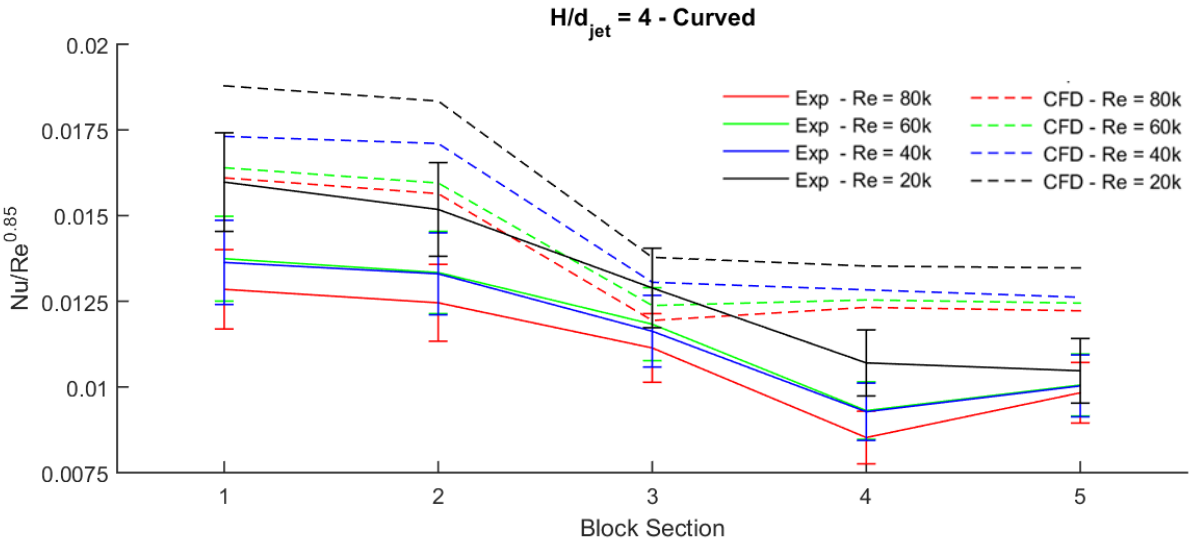

Figure 57: Area average Nusselt number: H/d = 4, curved wall

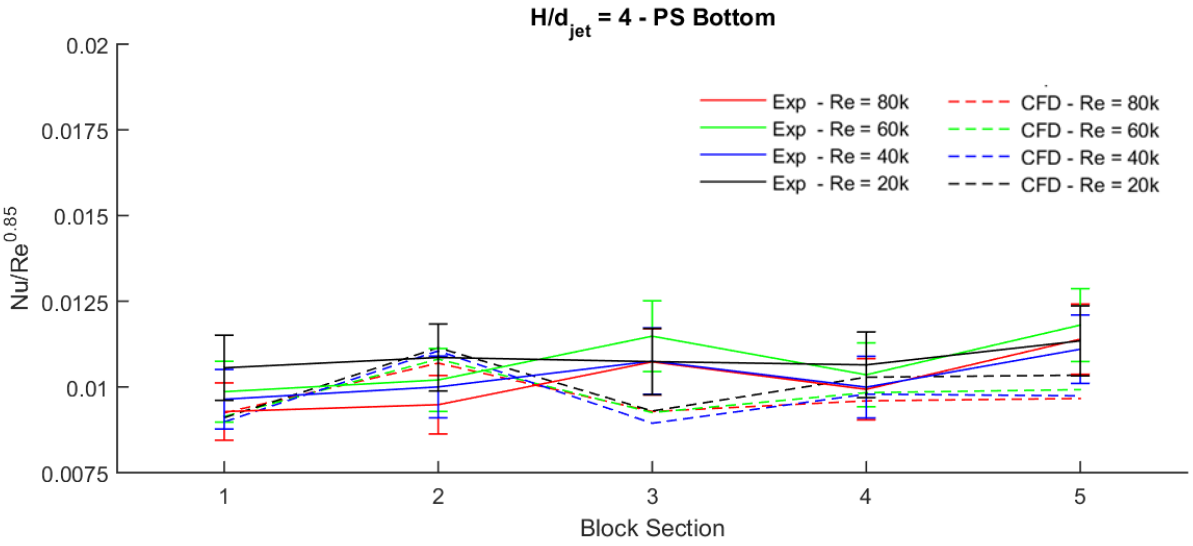

Figure 58: Area average Nusselt number: H/d = 4, PS bottom wall

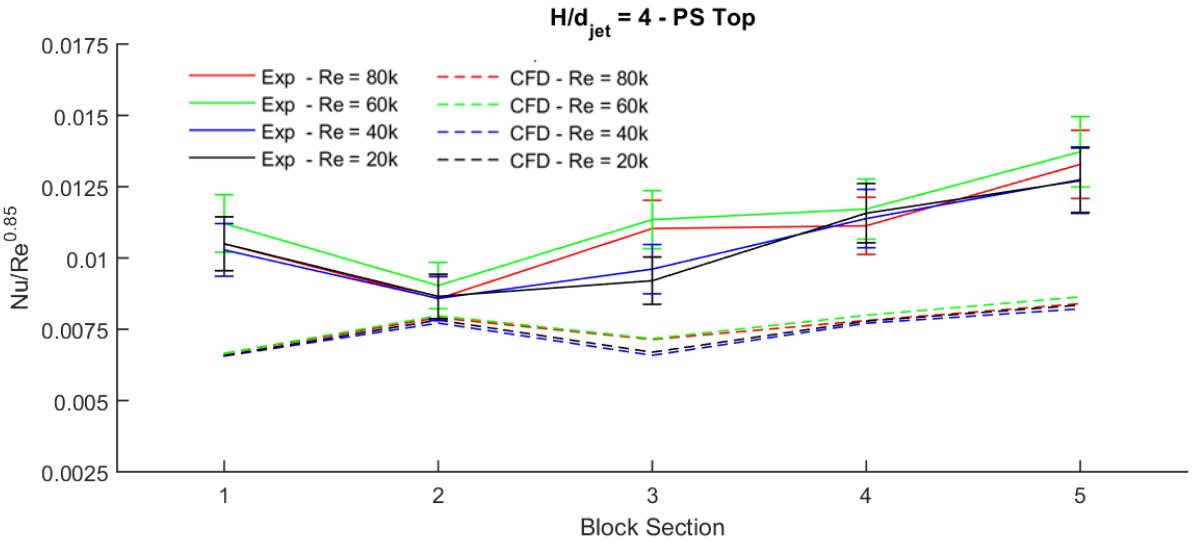

Figure 59: Area average Nusselt number: H/d = 4, PS top wall

8.2.1.4 - H/d Comparison

The difference in cross sectional geometries between the H/d = 2.7 and H/d = 4 configurations have a large effect on the jet characteristics as seen previously. This section will investigate the differences in area average Nusselt number of the shared walls ('SS Bottom', 'Curved', and 'PS Bottom') associated with the two configurations. For this comparison the test case of Re = 20,000 was isolated and compared for both numerical and experimental data.

The 'SS Bottom' wall for both configurations were fairly similar, Figure 60. They both followed the same trend of having a gradual increase in Nusselt number as the crossflow built up; however, the H/d = 4 configuration had a higher area average Nusselt number at each point. Overall the H/d has a slight effect on the area average heat transfer of this wall.

The 'Curved' wall also shows fairly similar results for each configuration, Figure 61. In both configurations the Nusselt number decreased at each subsequent block section until it reached its lowest at the 4th block section. The main difference between the two is that the H/d = 4

configuration has a much steeper, and overall larger, loss in heat transfer from the firth to the 4th block section. This is because the aforementioned boundary layer flow is thicker in this configuration, and there is less mixing of the fluid along the curved wall. Meanwhile, the numerical data of these two cases are also extremely similar, further implying that the heat transfer occurring at the leading edge of this geometry is independent of H/d between H/d = 2.7 and H/d = 4.

While the 'SS Bottom' and 'Curved' walls match fairly well between both H/d configurations, the 'PS Bottom' wall does not, Figure 62. At the upstream jets, block sections 1 and 2, the area average Nusselt numbers are similar; at the downstream blocks when the crossflow becomes dominant there is a large difference. To more accurately describe this difference, at the 3rd block the H/d =4 configuration has a larger area average heat transfer; then at the 4th and 5th block the H/d = 4 configuration has a much lower are average heat transfer. This is because in the H/d = 4 configuration the crossflow isn't as strong allowing the 3rd jet to have a stronger potential core, as seen previously in Figure 43, causing a stagnation region with slight circulation; meanwhile the lack of crossflow means the bulk velocity at the later jets is lower leading to the overall lower heat transfer.

The effect of the different crossflow velocity seen in the 'PS Bottom' wall is not present among the 'SS Bottom' wall. As mentioned before, the H/d = 4 configuration has a larger area average Nusselt number at every section of the 'SS Bottom' wall. This phenomena relates to the position of the block in respect to the H/d configuration. As previously mentioned, the 'SS Bottom' wall and the 'SS Top' wall both have a lower area average Nusselt number in reference to its peers in the H/d = 2.7 and H/d = 4 configuration respectively. These blocks are both in the corner of the suction side wall and H/d inlay of their respective configurations. This sharp corner, measuring at 70 degrees, is having an adverse effect on the heat transfer. By seeding the flow in the numerical

simulation in these locations, Figure 63, it is shown that a region of fluid becomes trapped in this corner and travels a majority of the spanwise distance of the rig. This trapped fluid causes the adverse effect on Nusselt number and its local effects can be seen in the following section 8.2.2.

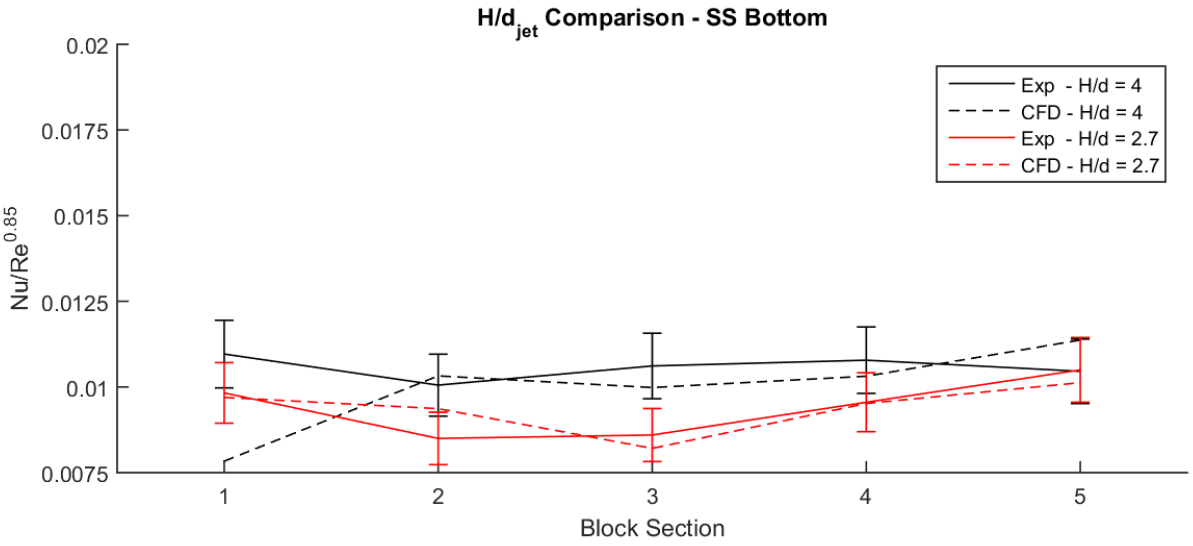

Figure 60: Area average Nusselt number vs H/d – SS bottom wall

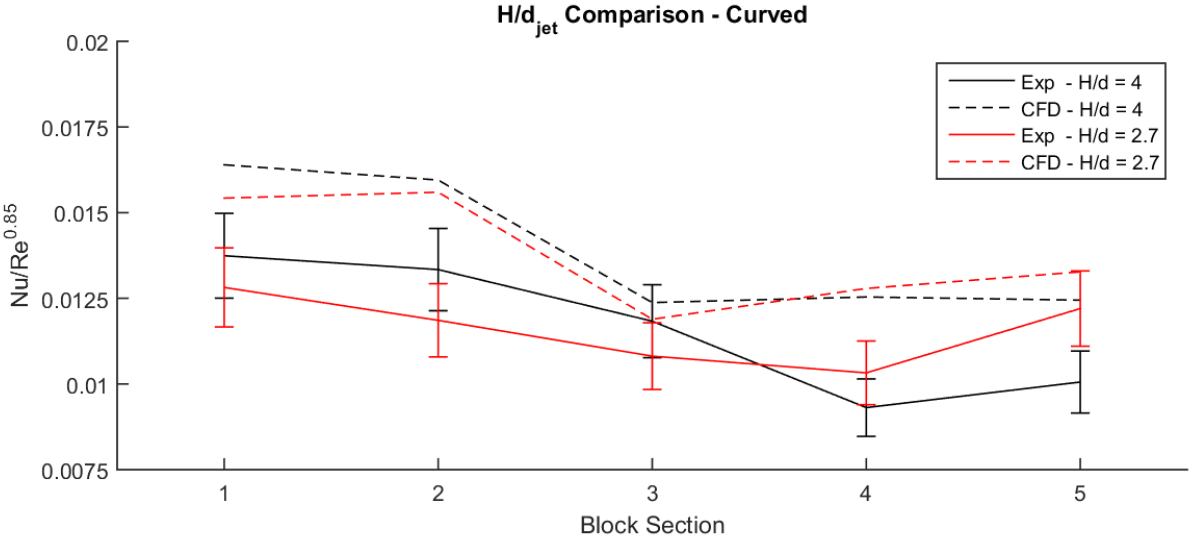

Figure 61: Area average Nusselt number vs H/d – curved wall

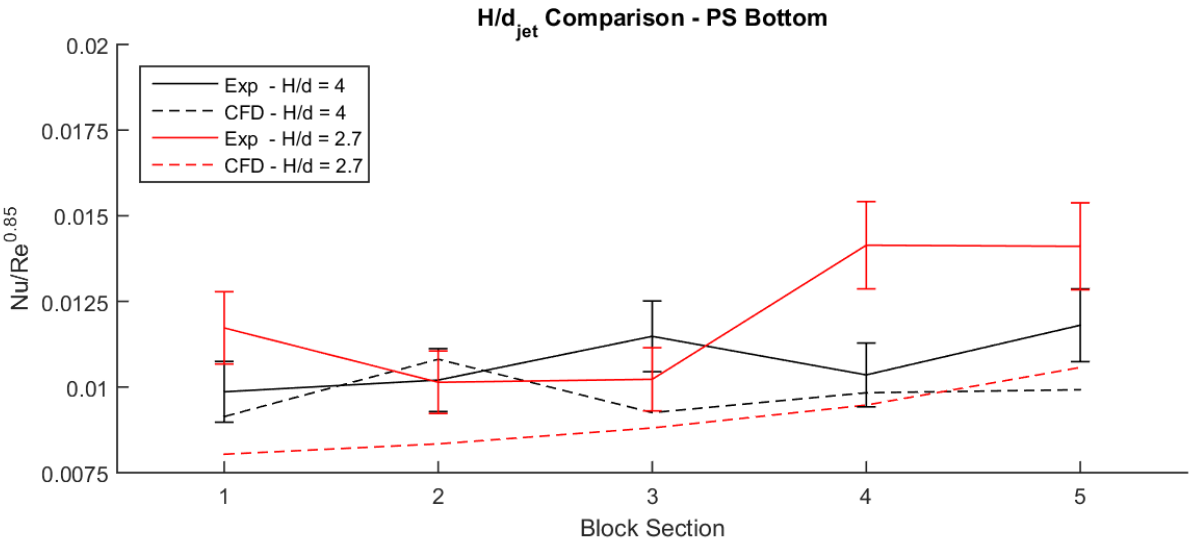

Figure 62: Area average Nusselt number vs H/d – PS bottom wall

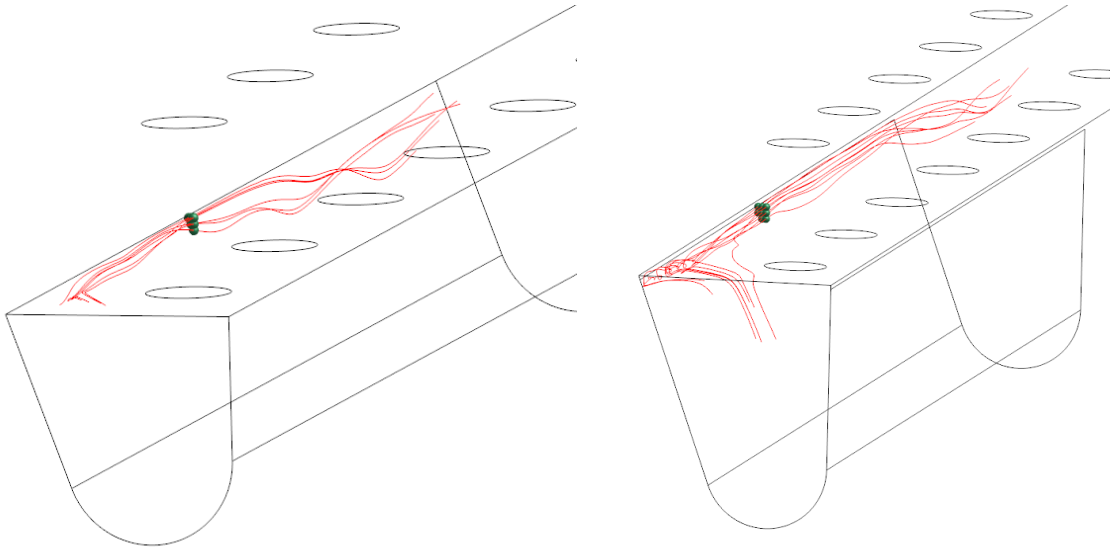

Figure 63: Streamlines of flow in suction side corner:
H/d = 2.7 (left), H/d = 4 (right)

8.2.2 - Contour Plots

The numerical simulation in Star CCM+ allowed for contour plots of the Nusselt number to be extracted. These contour plots show the local Nusselt number and give a better look into where the heat transfer is occurring.

This data was extracted from Star CCM+ and imported into TECPlot. An unwrap function was used to transform the coordinate system of the curved surface into a 2D mapping with axis y/d and S/d, where 'S' represents the arc length and S/d = 0 being the stagnation point directly below each jet. A coordinate transform was then applied to the suction side and pressure side walls to align them properly in the new S/d coordinate system.

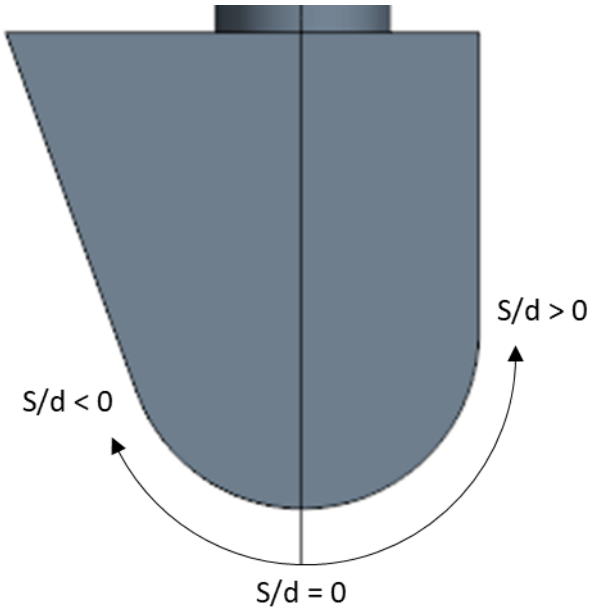

Figure 64: Coordinate transform to arc length coordinate system S/d

8.2.2.1 - H/d = 4

The H/d = 4 contour plots are shown in Figure 65 below. Looking at the effect of Reynolds number on local Nusselt number, an inverse correlation was found between the two parameters, particularly on the curved impingement region. This inverse correlation of normalized Nusselt number decreasing with Reynolds numbers means that the heat removal per mass flow rate is most efficient at the lowest Reynolds numbers, which in this case was Re = 20,000. This finding follows what was seen in the experimental area average Nusselt number plots of Figure 53 and Figure 57. This inverse correlation can also be seen in the spanwise Nusselt number plots discussed later in this thesis. Although the contour levels between the four Reynolds number cases are different, the contour patterns themselves are extremely similar.

Right away it is apparent that the highest location of heat transfer is occurring at the impingement point below the first two jets (y/d = 0 and y/d = -4), which relate to the curved wall sections which experienced the highest area averaged heat transfer. The increasing Nusselt number due to the crossflow on the sidewalls at each subsequent downstream jet can also be seen. This crossflow effect begins to take over near the 3rd jet as the contour plots begin to wash out and the local Nusselt number gradients become smaller. This is in conjunction with the experimental results in that the 3rd section typically has the lowest area average Nusselt number and then was outperformed by the 4th and 5th sections. Contrary to the sidewalls, the detriment to the Nusselt number on the curved wall can be seen at the high local Nusselt number upstream becomes washed out downstream. Lastly, the contour plots reveal a very low heat transfer occurring on the 'SS Top' wall (-4.70 < s/d < -3.39). This low localized heat transfer is located where the streamwise vortex nestled within the sharp corner in Figure 63. This low local heat transfer supports and further

explains why the ‘SS Top’ wall was the worst preforming walls in terms of heat transfer in the H/d = 4 configuration.

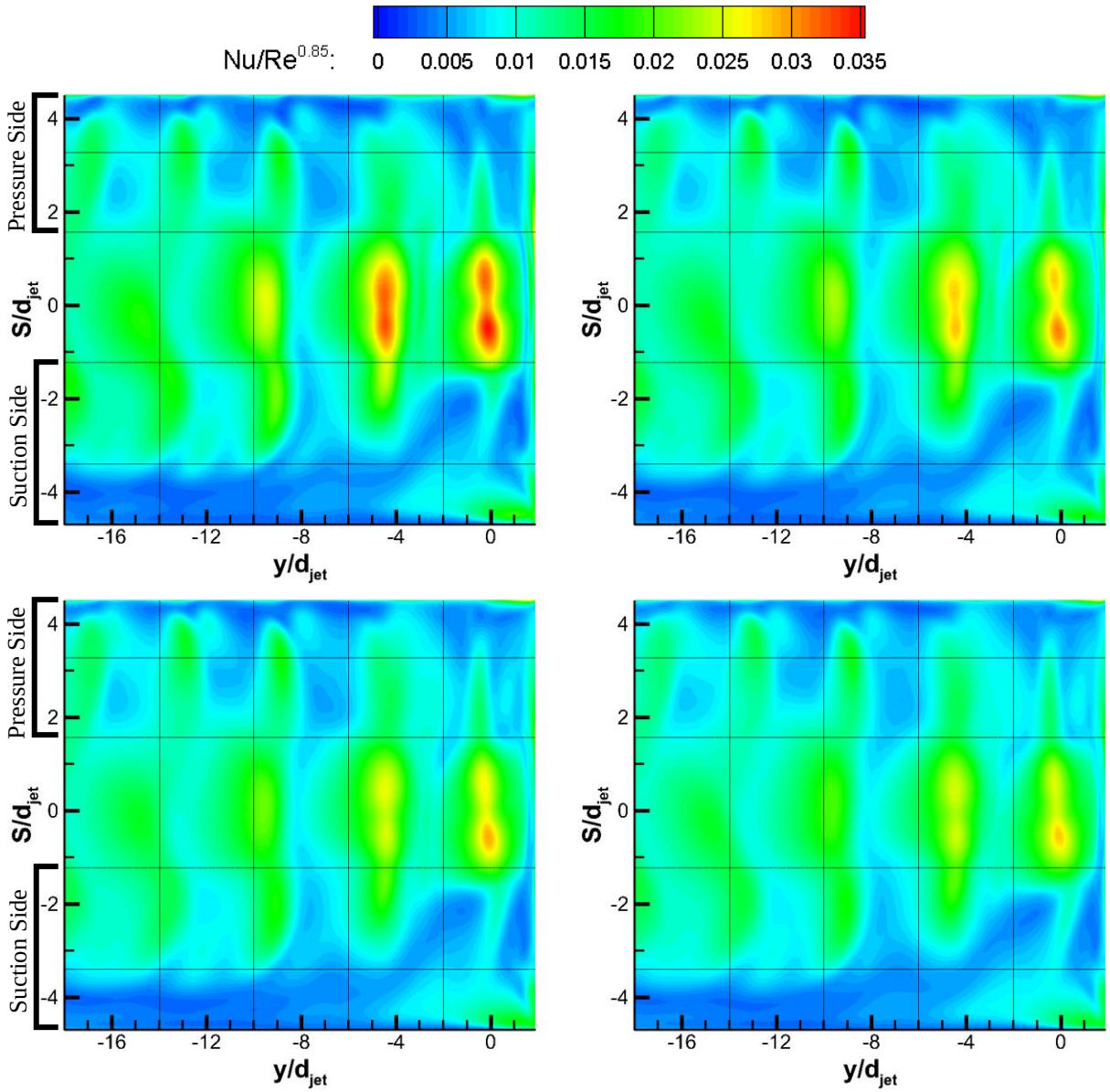

Figure 65: Nusselt contour plots of H/d = 4:
Re = 20k (top left), Re = 40k (top right), Re = 60k (bottom left), Re = 80k (bottom right)

8.2.2.2 - H/d = 2.7

The H/d = 2.7 configuration contour plots are shown in Figure 66 below. Many of the trends in the contour plots of H/d = 4 are also seen in the contour plots of H/d = 2.7. These similarities include the inverse relation between Nusselt number and Reynolds number, the high heat transfer of the stagnation regions for the 1st and 2nd jet, and the crossflow domination downstream.

At H/d = 2.7 the highest local Nusselt number once again occurs at the stagnation regions of the 1st and 2nd jet; however, the local heat transfer at the stagnation regions of these jets are significantly higher and extend over a larger area for the H/d = 4 configuration compared to the H/d = 2.7 configuration. This is due to the increased jet bending at the lower H/d preventing the jet from reaching the stagnation region at its fullest strength. Located upstream of the 1st jet is a large circular pattern on both sidewalls that isn't prevalent in the H/d = 4 configuration. This pattern is because of the stronger recirculation upstream occurring at the lower H/d seen previously.

At the downstream jets the crossflow begins to dominate the local heat transfer after the 2nd jet. From the 3rd jet onward the local Nusselt number gradients are extremely low. In comparison to the H/d = 4 geometry, this crossflow domination begins sooner for the H/d = 2.7 configuration. This is again because the overall smaller cross sectional area of the leading edge cavity results in a higher crossflow velocity and more jet bending. The low local heat transfer occurring on the 'SS Bottom' wall is also prevalent in this geometry and supports the results of the low experimental area average Nusselt number of the 'SS Bottom' wall being caused by the streamwise vortex in Figure 63.

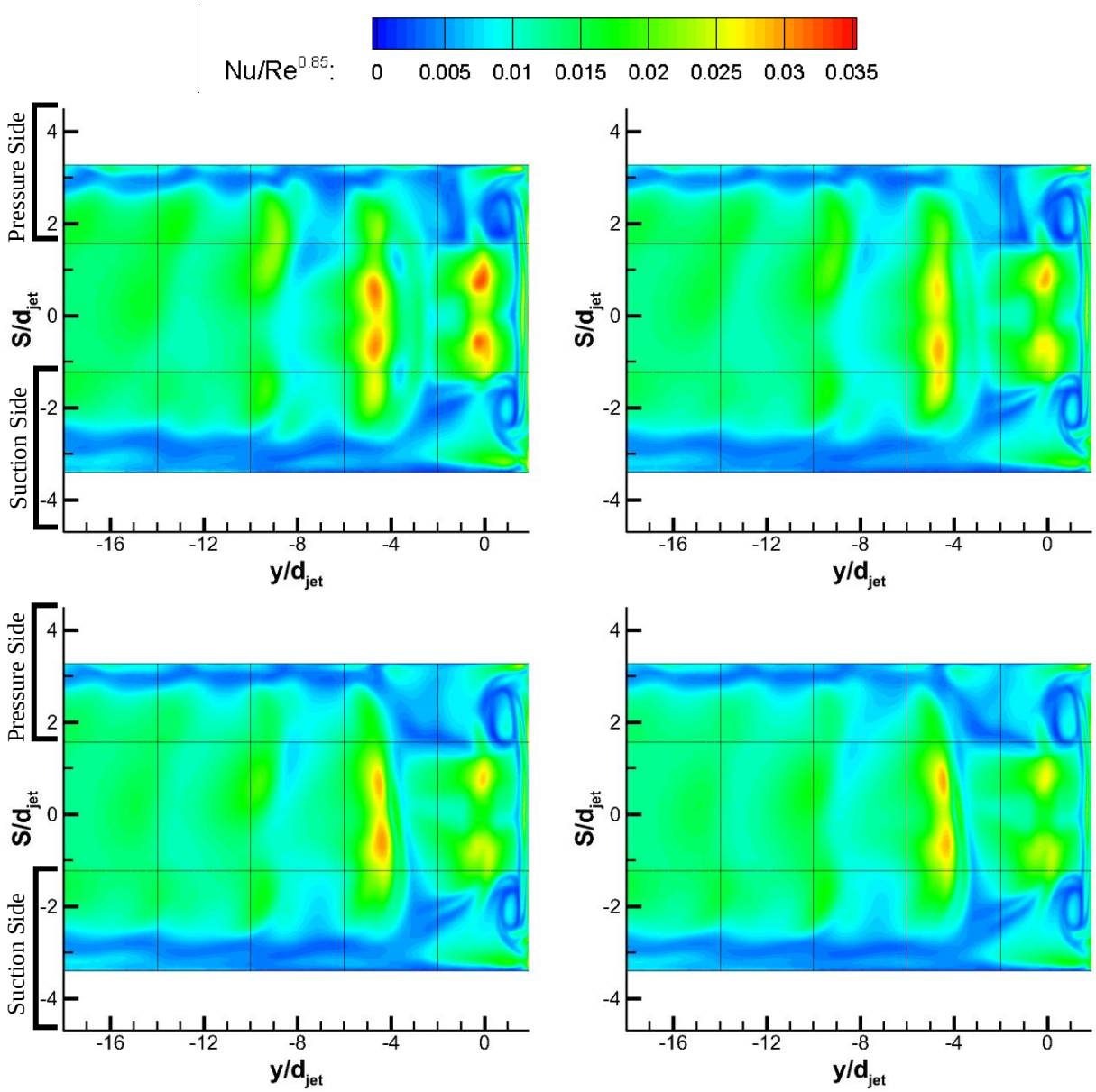

Figure 66: Nusselt contour plots for H/d = 2.7:
Re = 20k (top left), Re = 40k (top right), Re = 60k (bottom left), Re = 80k (bottom right)

8.2.3 - Lateral Average

By taking infinitesimal slices of the target surface in the y/d axis, and then averaging the Nusselt number along this line a lateral average is taken. Compiling these lateral averaged for an infinite number of slices between y/d = 2 and y/d = -16 yields the spanwise lateral average. This spanwise lateral average of Nusselt number gives insight to where the highest and lowest heat transfer is occurring in the streamwise direction.

8.2.3.1 - Reynold Number Effects

The spanwise lateral average was plotted for each geometry at the varying Reynolds numbers in Figure 67. Both geometries follow similar trends of oscillating about a mean and approach that mean at the downstream jets. These oscillations are larger upstream at the 1st and 2nd jet with the highest peak corresponding to the 2nd jet in both cases. Meanwhile downstream, the oscillations begin to dampen out and approach that said mean as the crossflow begins to dominate the heat transfer.

The effects of the jet bending on the location of the stagnation region and its associated heat transfer, the peaks, are very noticeable in the streamwise lateral average plots. The shift in the stagnation region first occurs at the 2nd jet where it is slightly downstream of the jet-centerline (y/d = -4). Between these peaks, the troughs also shift. This begins to become apparent at the 3rd jet; as the stagnation region is shifted to y/d = -9, some of the weakest cooling occurs at the jet-centerline y/d = -8. This shift, and lack of cooling at the jet-centerline, is also seen at the 4th jet where the impingement region is shifted even more.

Comparing the spanwise lateral average for different Reynolds numbers it can be seen that there are slight variations between the plots. In both configurations it can be seen that the lower Reynolds numbers have higher peaks, but equivalent troughs, compared to the higher Reynolds numbers. This agrees with what was seen in the contour plots and experimental averages in that there are diminishing returns in Nusselt number with increased Reynolds number.

Another effect that Reynolds number has on the spanwise lateral average is the spanwise locations of the peaks. This effect is only seen in the H/d = 2.7 configuration and effects the 2nd and 3rd jet. At the second peak in Figure 67 (top) the higher Reynolds numbers have the peak shifted further upstream, while the third peak is shifted further downstream. This shift in the peak associated with different Reynolds numbers is most likely due to higher velocity crossflow at the higher Reynolds numbers.

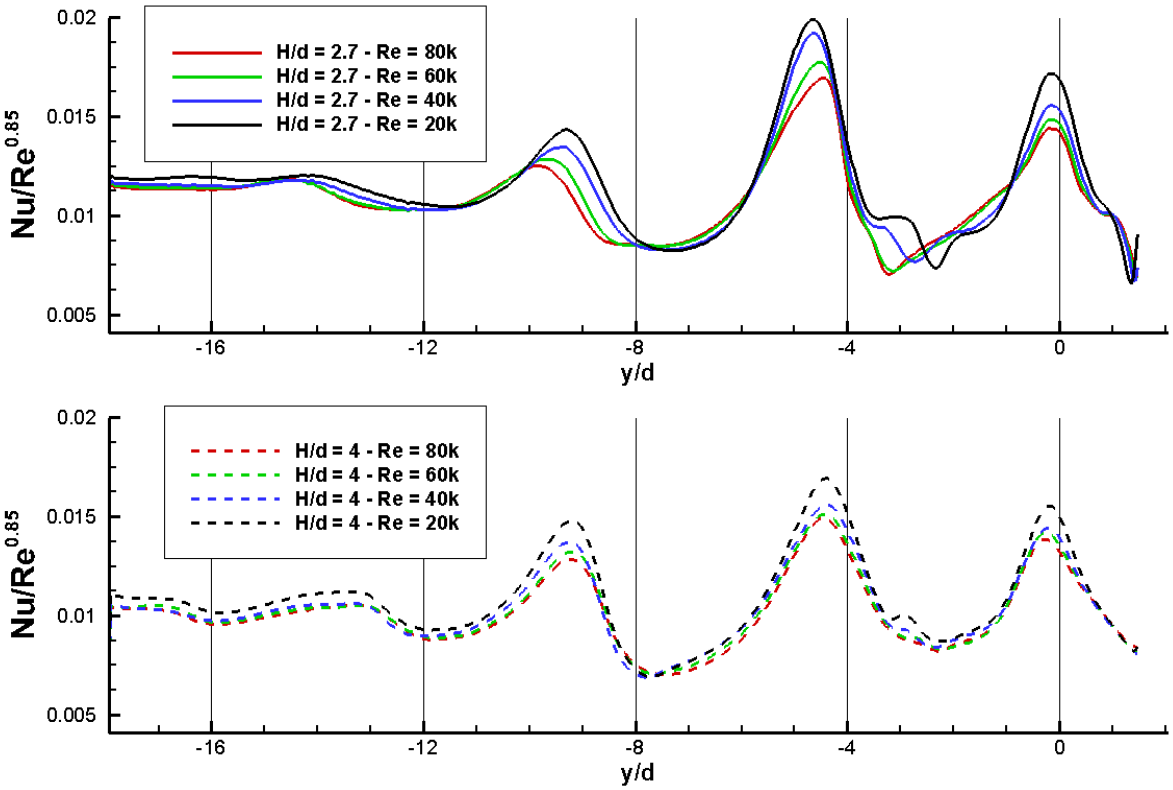

Figure 67: Spanwise lateral average of Nusselt number vs Reynolds numbers: H/d = 2.7 (top), H/d = 4 (bottom)

8.2.3.2 - H/d Comparison

Further looking at the spanwise lateral average Nusselt number, by comparing the two H/d configurations we can better understand how the H/d effects the heat transfer. In Figure 68 below the spanwise lateral average for each Reynolds number is compared between the two H/d's.

Both configuration follow the same trends with three large peaks representing the upstream jets which oscillate about a mean and then dampen out downstream, as seen in Figure 68. However, the H/d = 2.7 configuration has a higher Nusselt number for most lateral spanwise locations. This is shown by the higher peaks and by the mean Nusselt number at which these peaks oscillate about. This generally higher Nusselt number is caused by the lower heat transfer occurring on the 'SS Top' and 'PS Top' blocks present in the H/d = 4 configuration. When these blocks are omitted, Figure 69, lateral average of the H/d = 4 configuration outperforms the H/d = 2.7 configuration in both the stagnation and crossflow dominated regions, which is consistent with the previously discussed experimental and numerical data.

The H/d does have an effect on the location of these peaks. At the lower H/d the peaks tend to be shifted downstream. This shift in the peak location is larger at each subsequent jet, in that the second peak is shifted less than y/d = 1 away from one another while the fourth peak is shifted greater than y/d = 1. This shift is attributed to the increased crossflow and jet bending at the lower H/d configuration.

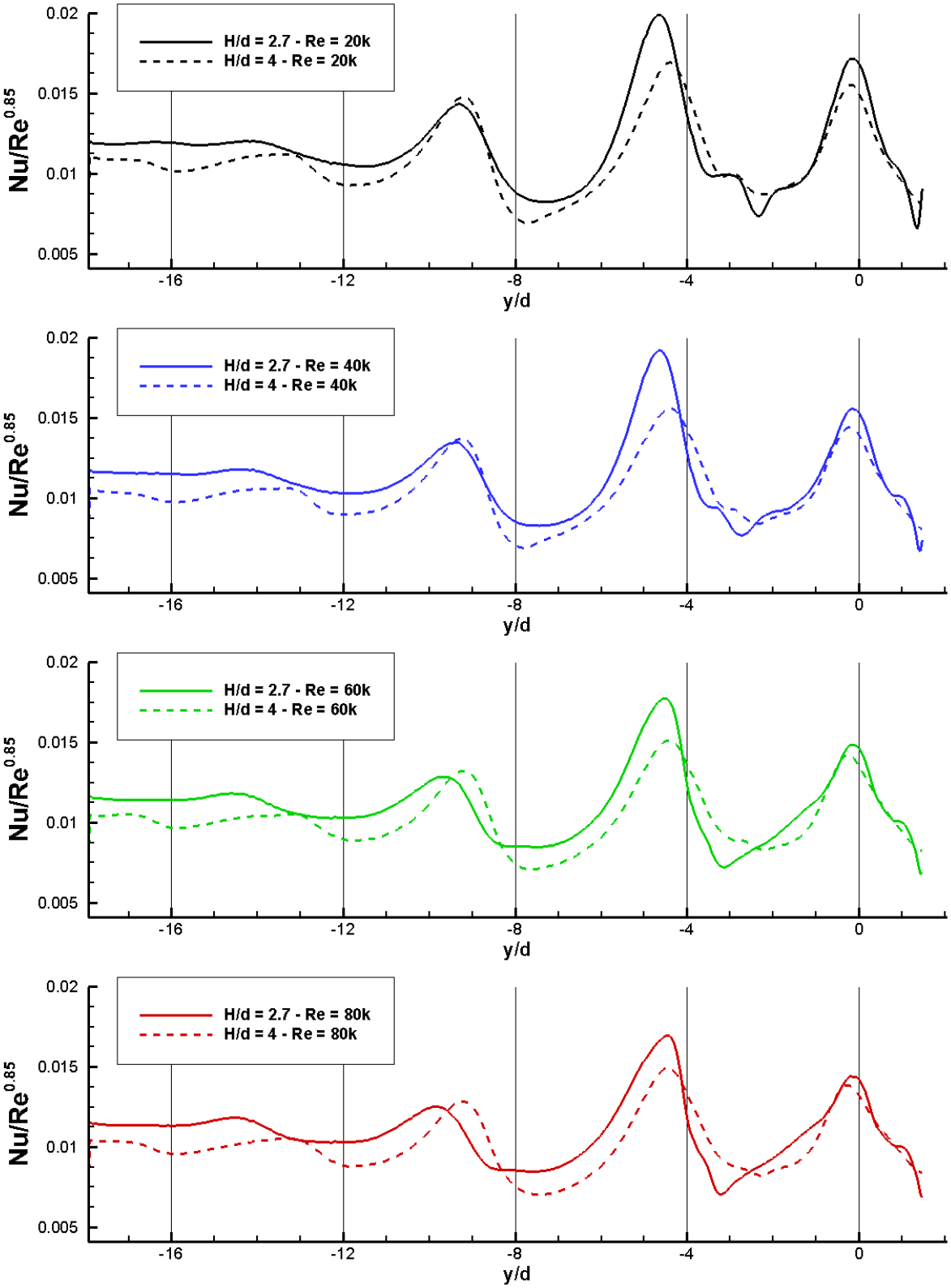

Figure 68: Spanwise lateral average of Nusselt number vs H/d:
Top to bottom: Re = 20k, Re = 40k, Re = 60k, Re = 80k

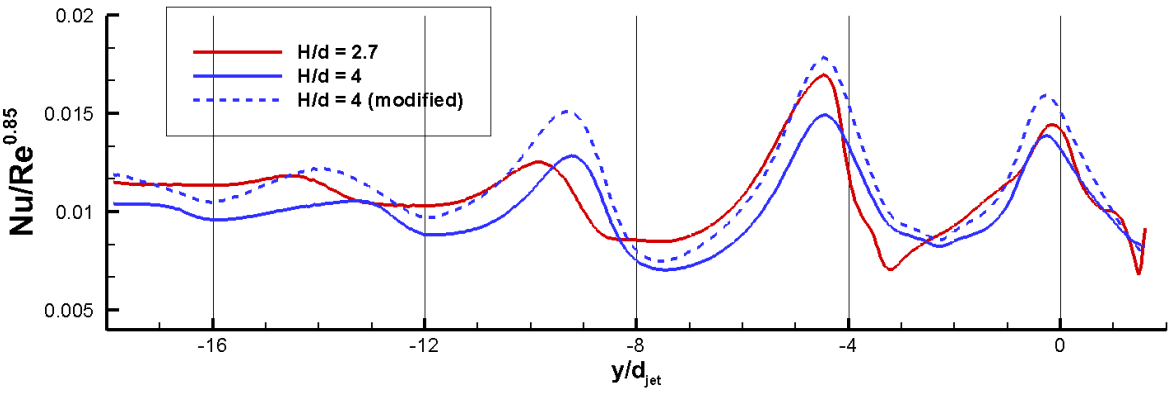

Figure 69: Spanwise lateral average of Nusselt number vs H/d (Re = 80k)

CHAPTER 9: CONCLUSION AND FUTURE WORK

9.1 - Conclusion

In the previous chapter, the mean flow field and the heat transfer within the leading edge cavity was quantified for two different geometries: H/d = 2.7 and H/d = 4. It was found that the H/d = 2.7 geometry had a much larger crossflow due to its reduced cross sectional area. This crossflow effect consisted of a faster crossflow velocity, the crossflow velocity increasing faster, and a drastically larger jet bending effect. These increased crossflow effects ultimately lead to decreased heat transfer occurring within the leading edge cavity when compared to the H/d = 4 geometry. In conclusion, the method of correlating the heat transfer to the flow field was found to be successful.

In both geometries the flow field within the leading edge cavity becomes dominated by the crossflow by y/d = -12. At this point there are very little flow features present and the spent air from each jet is bent downstream and transitioned directly into the crossflow. The effect is apparent in both the area averaged and local heat transfer. At the upstream jets, y/d > -6, there is a strong stagnation region heat transfer on the curved target surface. However this stagnation region heat transfer on the curved target surface dissipates as the y/d decreases. Vice versa, the heat transfer along the side walls tend to increase as y/d decreases due to the faster crossflow velocity.

The investigation was also successful in identifying several flow structures within the leading edge cavity. Of these, the two most interesting being the horse shoe type vortices behind the 2nd jet and the counter rotating vortices in the corner of the suction side wall and the jet orifice.

The latter were found to span the entirety of the leading edge cavity and entrap fluid within it, creating a detriment to heat transfer in that local area.

The numerical solution matched the overall salient features of the flow field fairly well when compared with the experimental results. The vortices present in the PIV were also seen in the CFD, and the heat transfer results were in good agreement. The numerical simulation was found to be comparable to that of the experimental allowing for further characteristics of the numerical solution to be investigated. However, finer flow features were inconsistent with experimental results and further refinement of the numerical simulation is needed to more accurately model the physics within the leading edge cavity. These differences stemmed from the RANS model's inability to properly capture the separation at the plenum side of the jet hole and thus propagating to an over predicted vena contracta effect. Resolving these flow physics in a spatial scale multiple orders of magnitude smaller, such as in LES, could better model the leading edge cavity and yield an extensive in depth look of much finer small scale fluid interactions.

9.2 - Future Work

This thesis investigated the flow field of the jet-centerline plane and the heat transfer associated. Throughout this investigation, various aspects regarding the further understandings of leading edge jet impingement and aspects complimentary to those present in this study came to fruition. Should these be further investigated they could contribute to the underlying knowledge in academia. These include but are not limited to:

- A numerical LES simulation for both H/d configurations, eliminating the vena contracta effect present in the RANS simulation and further spatially resolving the vortices.

- Stereo PIV at multiple planes to experimentally capture the 3rd velocity component, better quantifying the flow field.

- A numerical simulation comparing the 'ideal' geometry to the 'nominal' geometry of the PIV rig; achievable by CT scanning the PIV rig and importing the scanned model into StarCCM+. This would investigate how minor surface imperfections effect the overall flow field, as many turbine blades today are 3D printed and such imperfections are not uncommon.

- Adjusting the cross flow configuration to exit from both ends of the leading edge cavity. This serves to better model a real world case as some turbine blades are designed in this fashion. PIV, CFD, and heat transfer tests done in this crossflow configuration would further the knowledge of this topic and could be compared to the single direction crossflow configuration.

APPENDIX A: SUPPORTING FIGURES

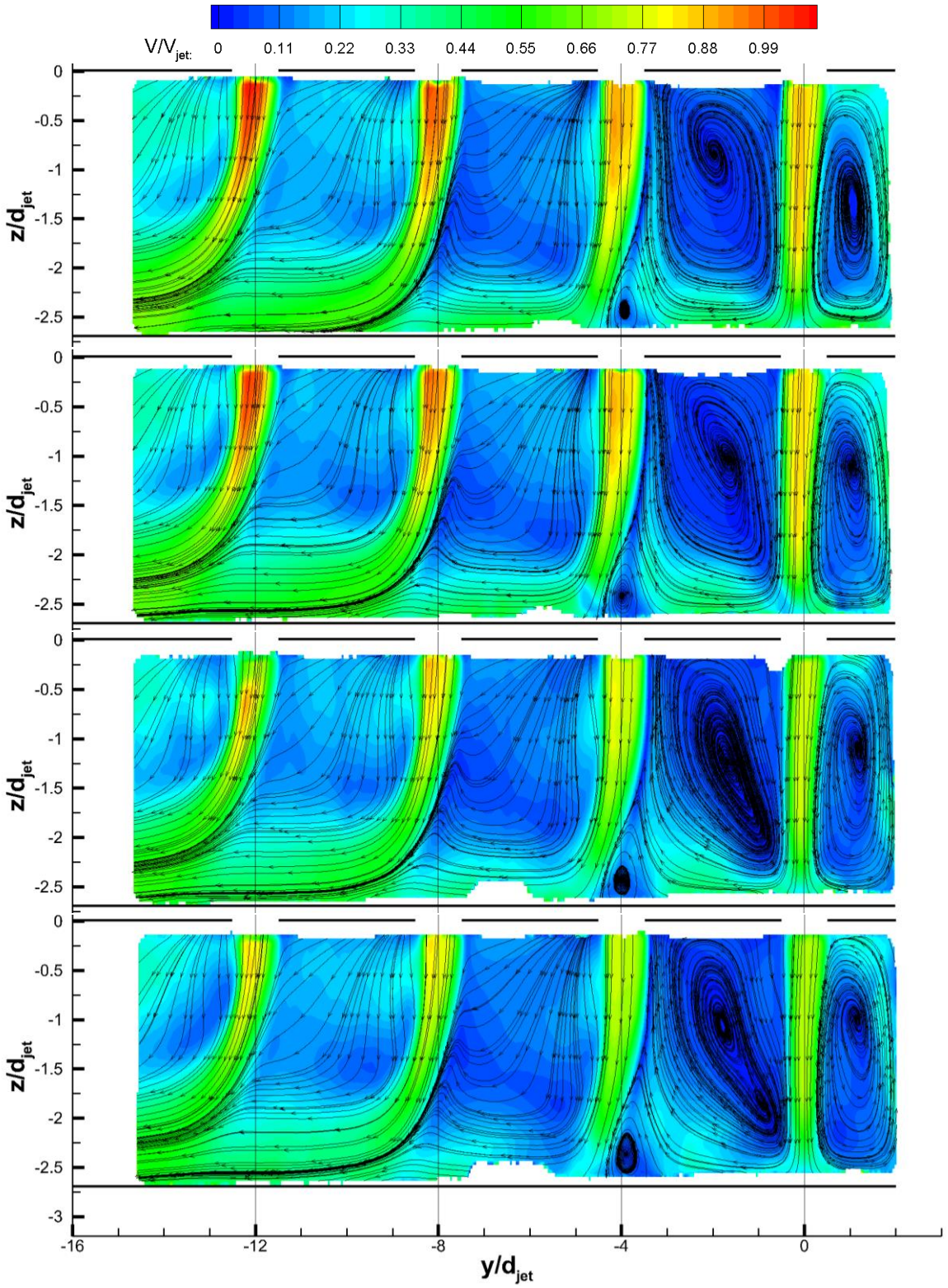

Figure 70: PIV velocity contour plots at H/d = 2.7, -16 < y/d < 2:
Top to bottom: Re = 20k, Re = 40k, Re = 60k, Re = 80k

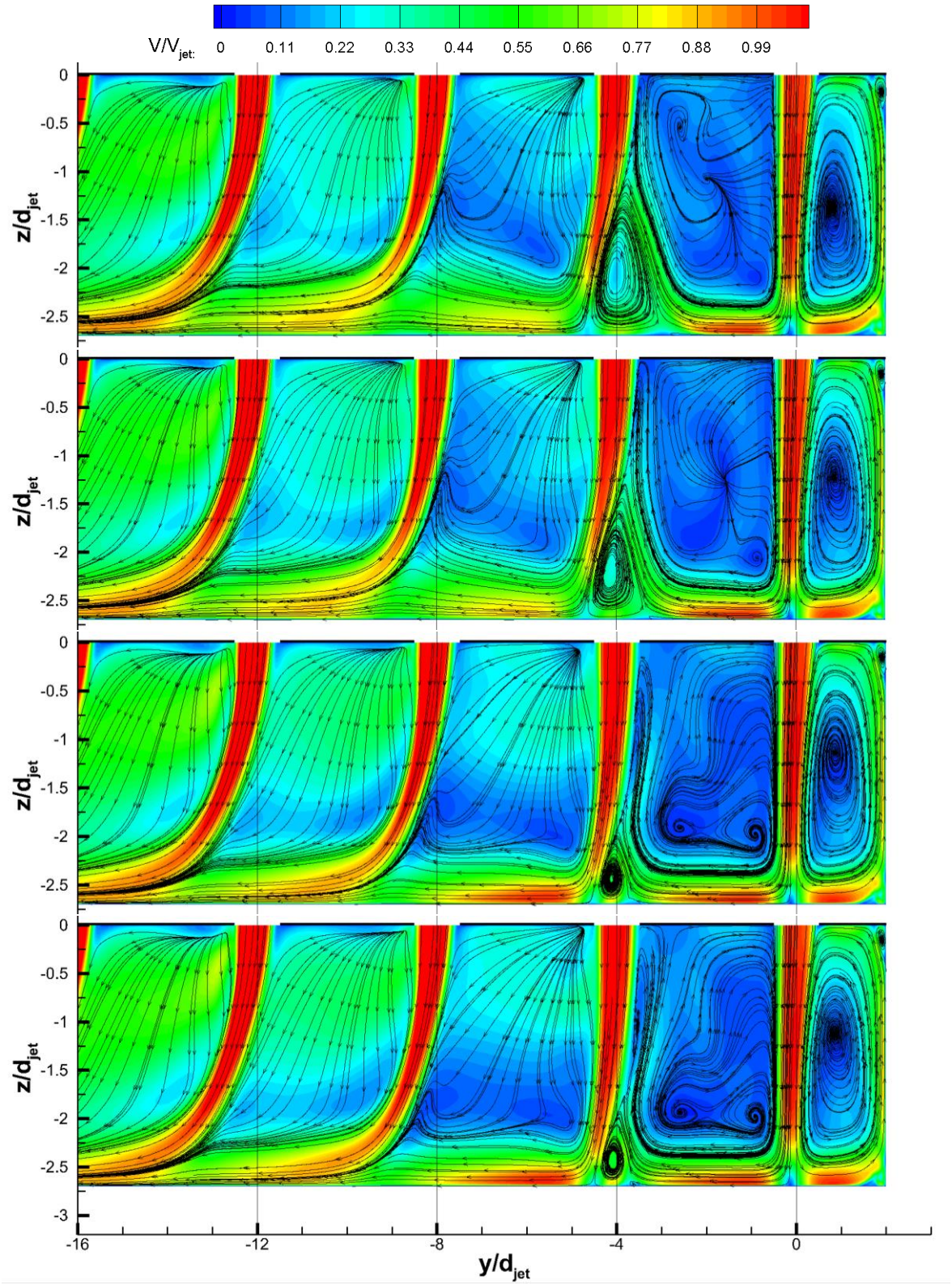

Figure 71: CFD velocity contour plots at H/d = 2.7, -16 < y/d < 2:
Top to bottom: Re = 20k, Re = 40k, Re = 60k, Re = 80k

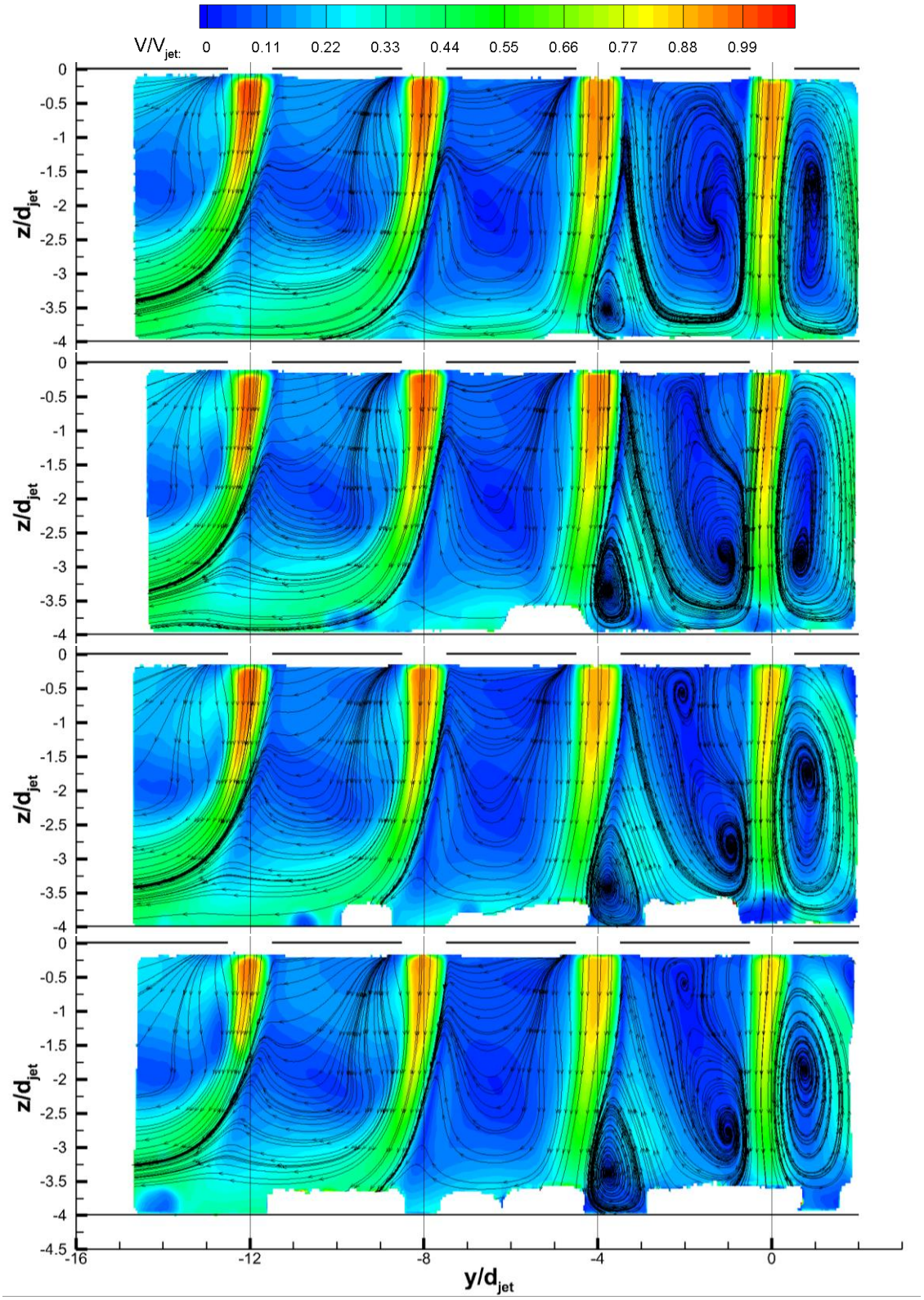

Figure 72: PIV velocity contour plots at H/d = 4, -16 < y/d < 2:
Top to bottom: Re = 20k, Re = 40k, Re = 60k, Re = 80k

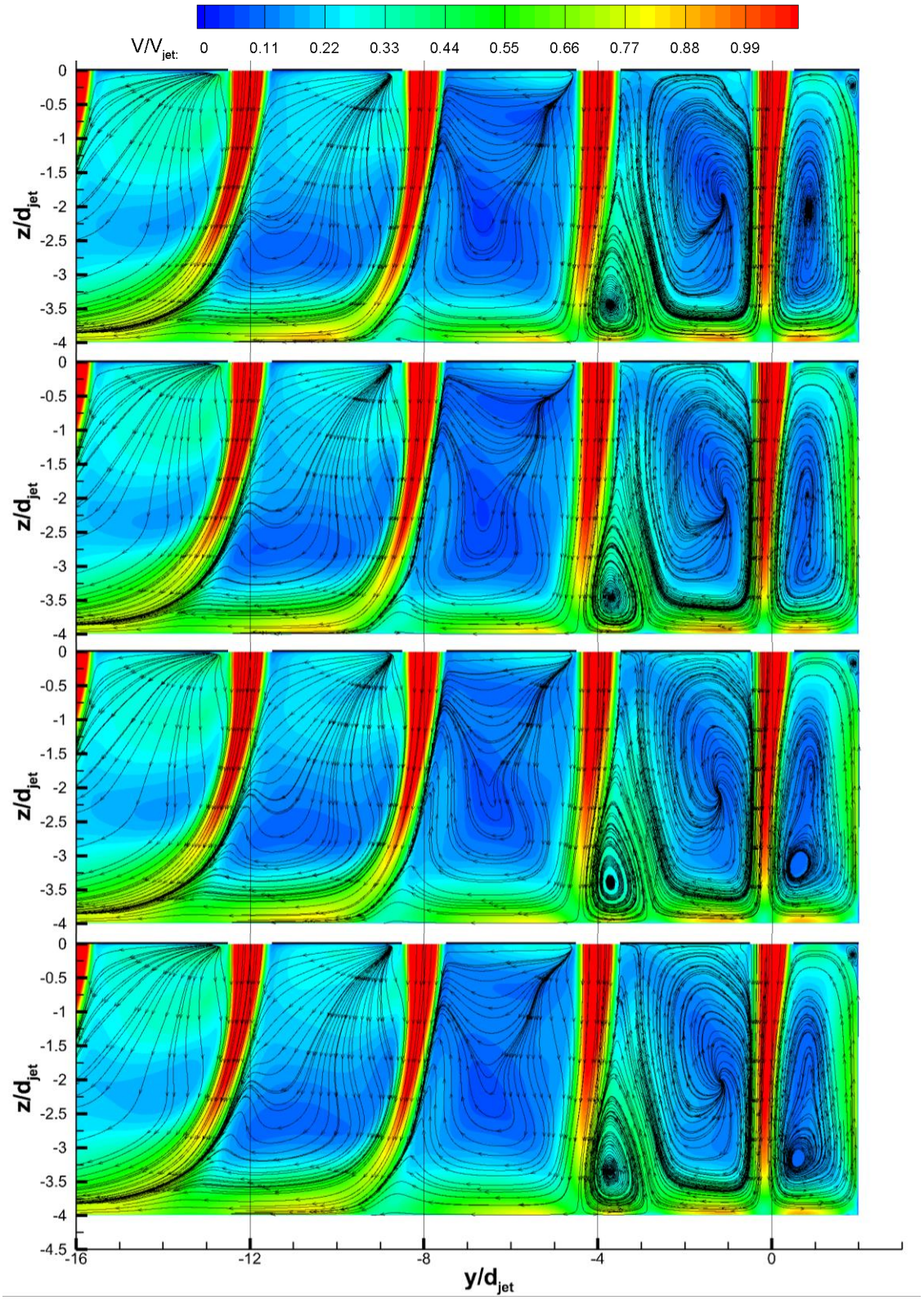

Figure 73: CFD velocity contour plots at H/d = 4, -16 < y/d < 2:
Top to bottom: Re = 20k, Re = 40k, Re = 60k, Re = 80k

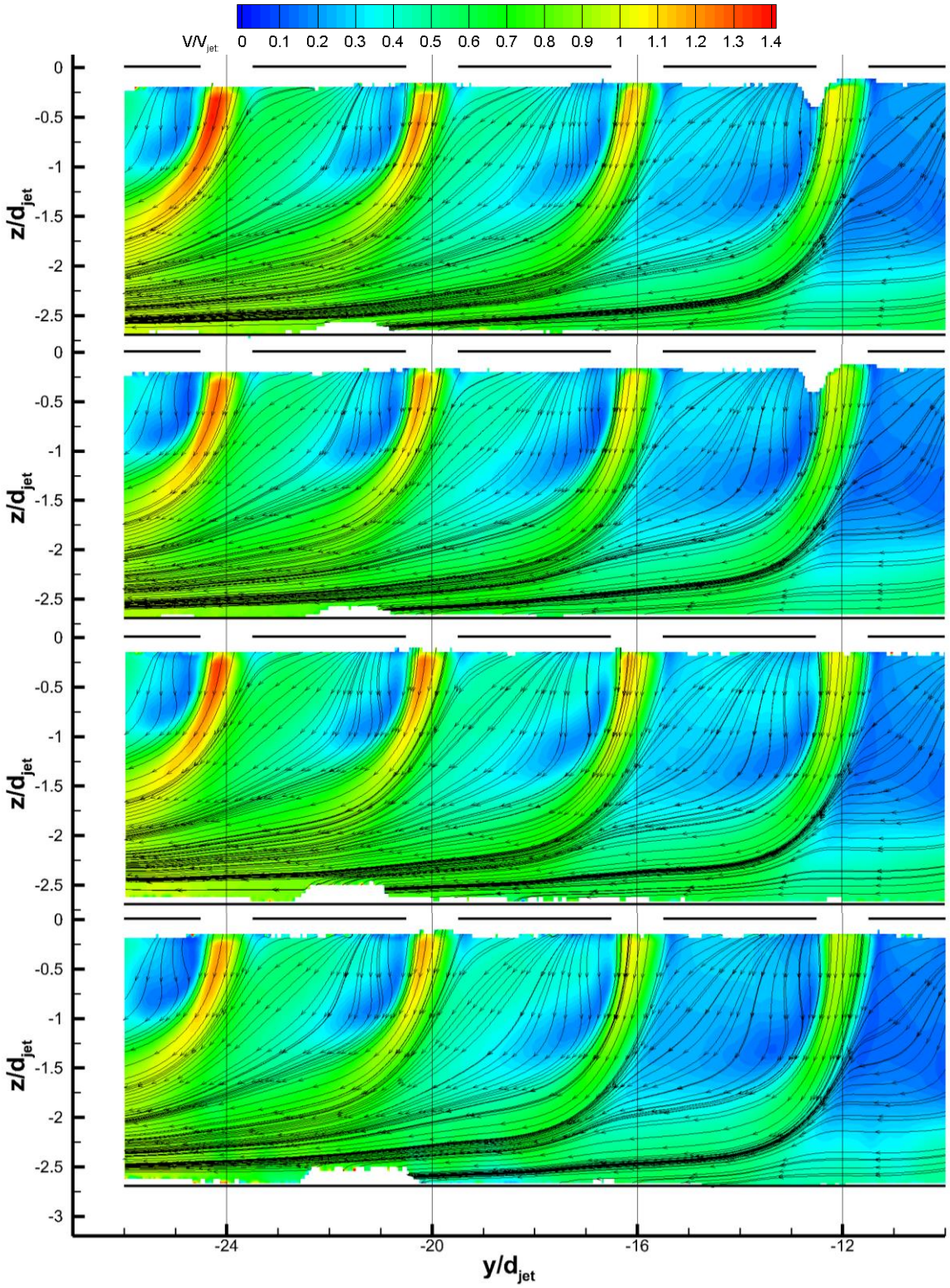

Figure 74: PIV velocity contour plots at H/d = 2.7, -26 < y/d < -10: Top to bottom: Re = 20k, Re = 40k, Re = 60k, Re = 80k

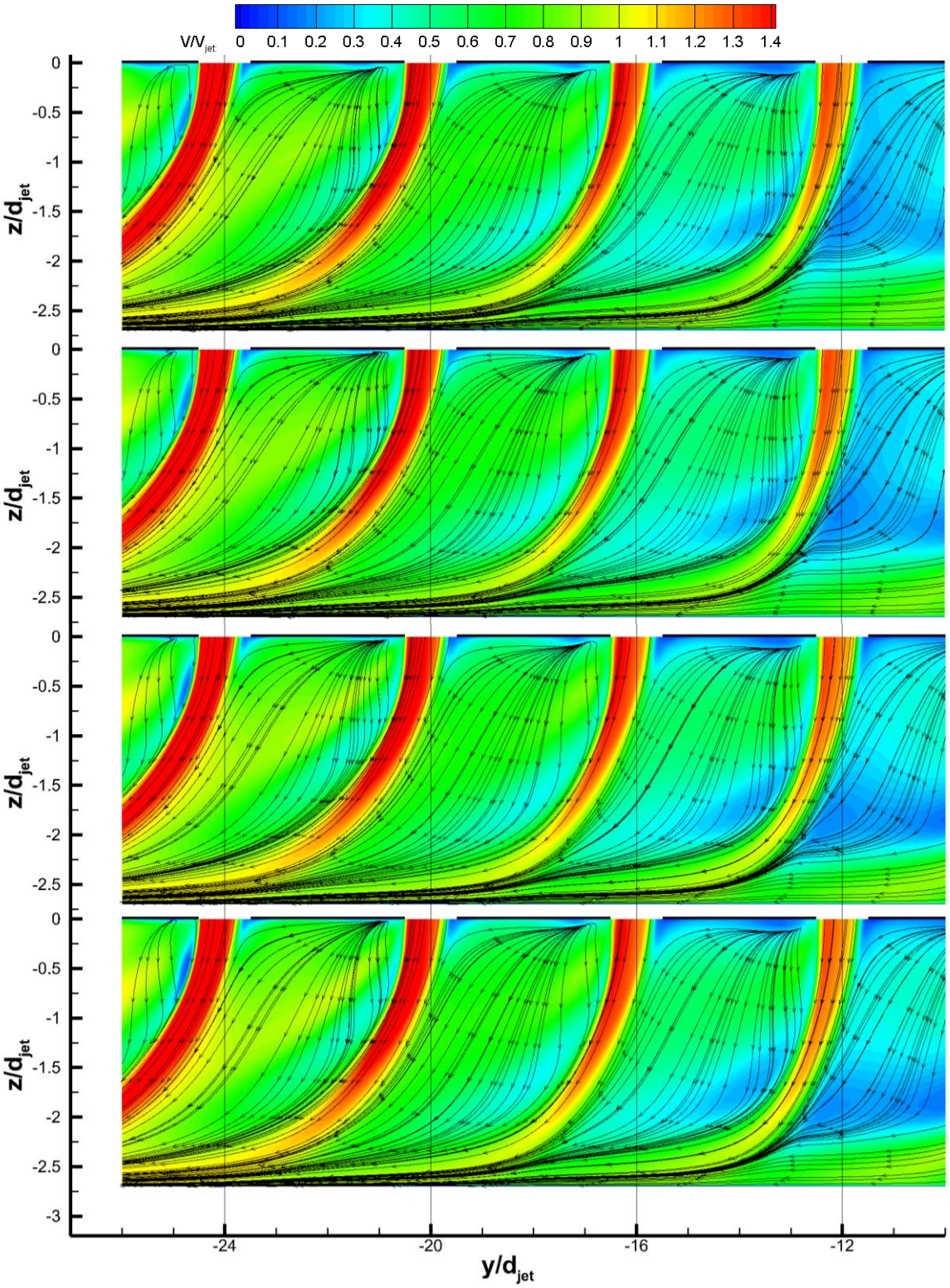

Figure 75: CFD velocity contour plots at H/d = 2.7, -26 < y/d < -10: Top to bottom: Re = 20k, Re = 40k, Re = 60k, Re = 80k

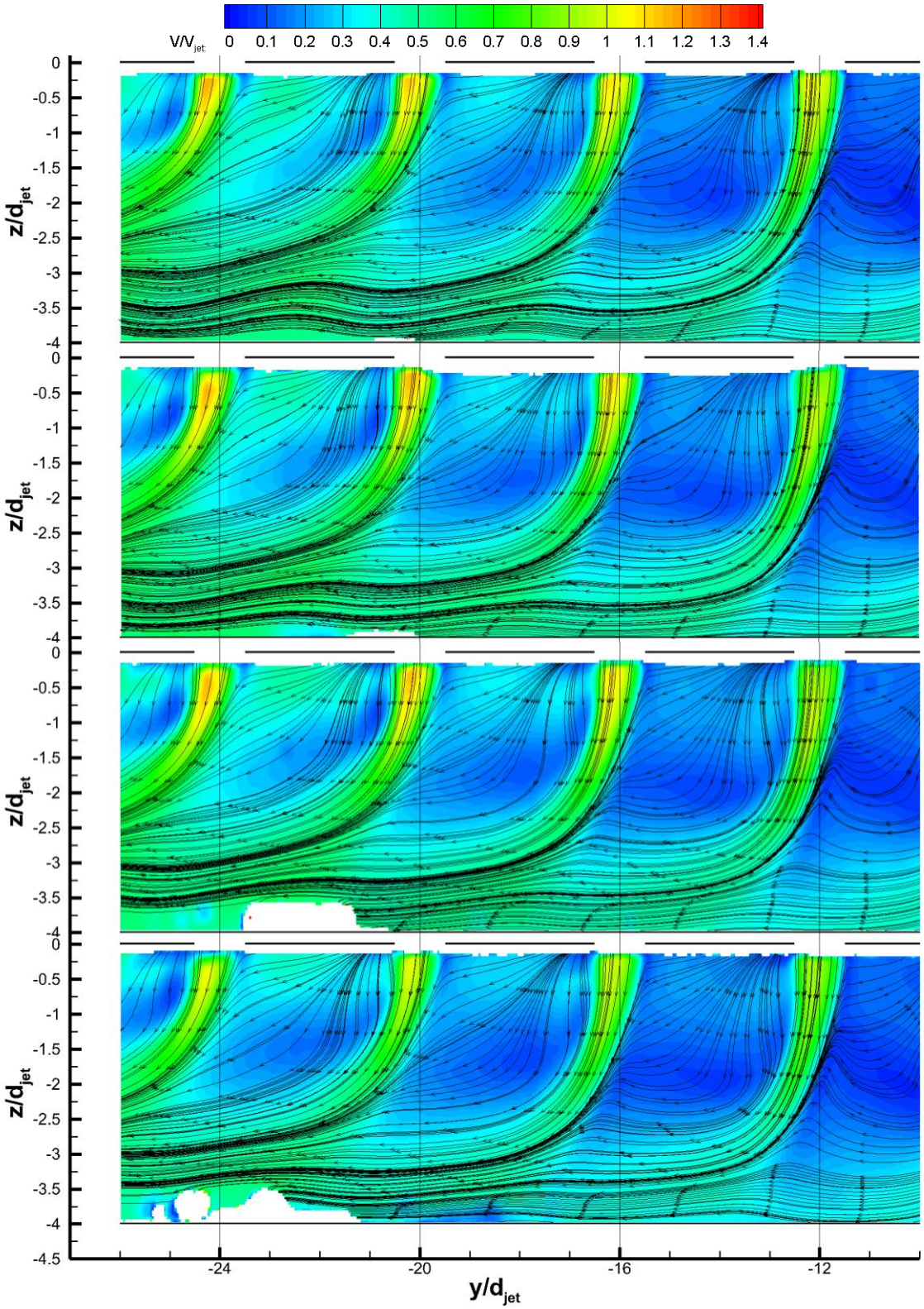

Figure 76: PIV velocity contour plots at H/d = 4, -26 < y/d < -10:
Top to bottom: Re = 20k, Re = 40k, Re = 60k, Re = 80k

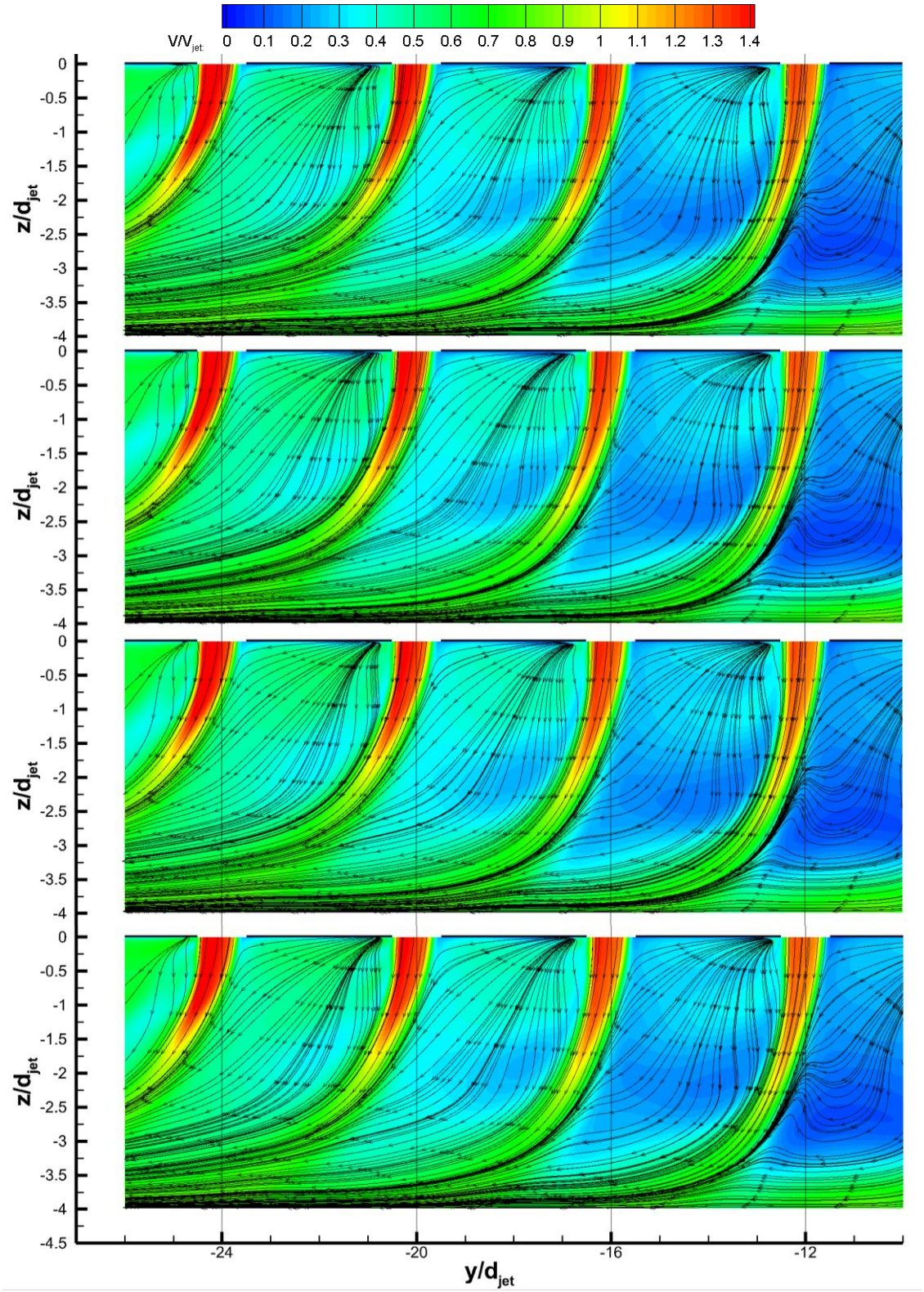

Figure 77: CFD velocity contour plots at H/d = 4, -26 < y/d < -10:
Top to bottom: Re = 20k, Re = 40k, Re = 60k, Re = 80k

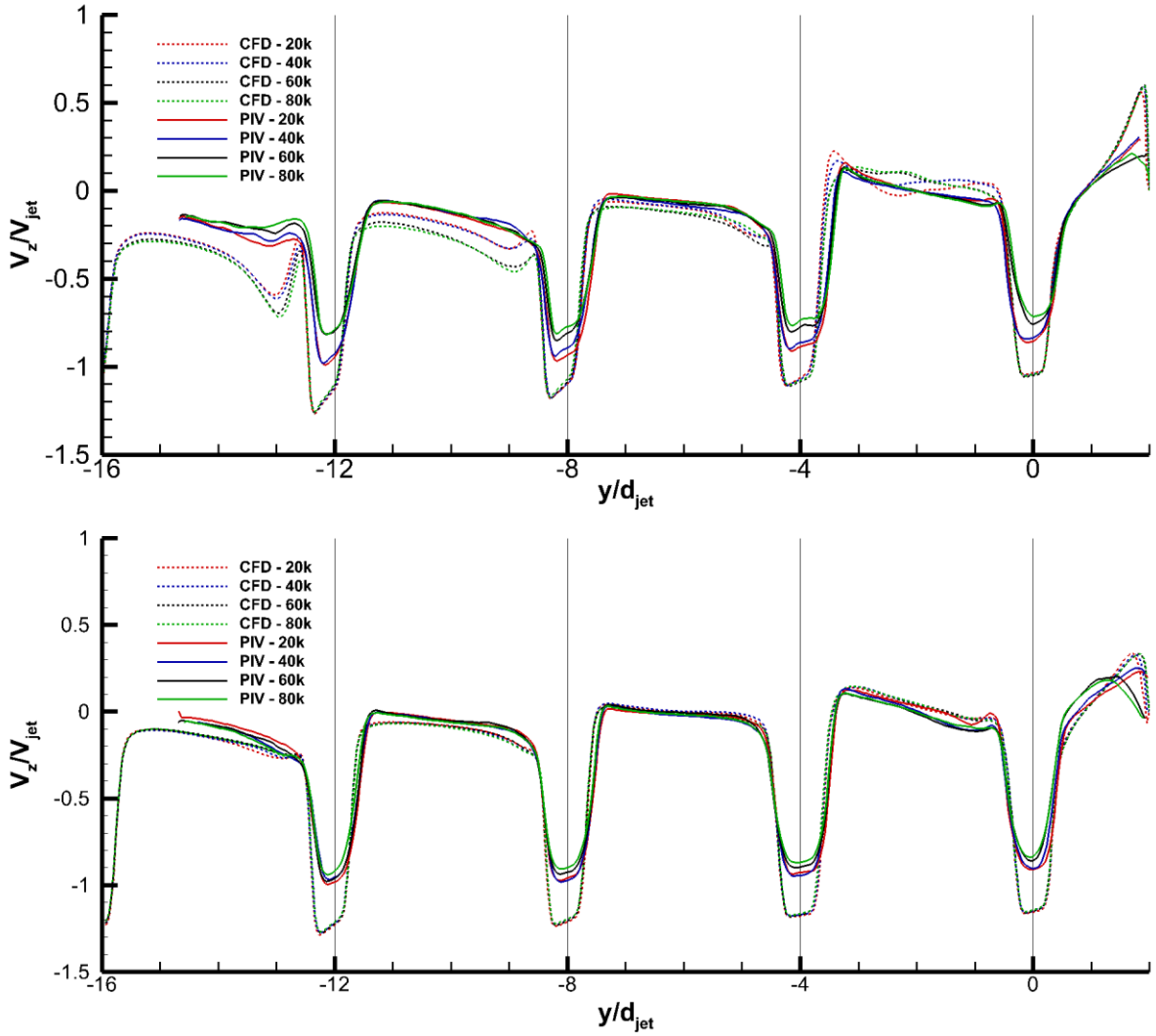

Figure 78: Axial velocity at wall normal distance z/d = 0.5:
H/d = 2.7 (top), H/d = 4 (bottom)

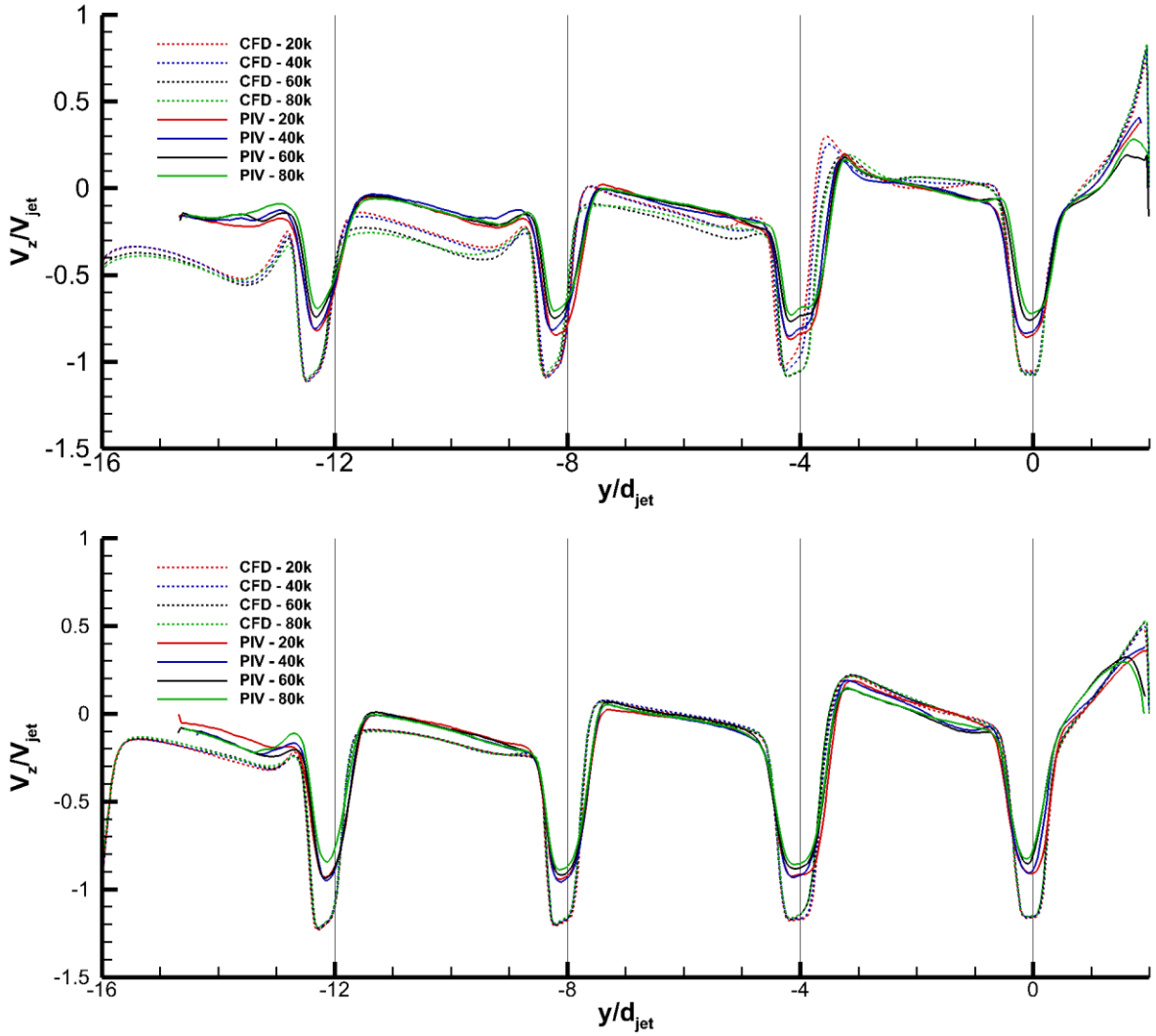

Figure 79: Axial velocity at wall normal distance z/d = 1:
H/d = 2.7 (top), H/d = 4 (botto

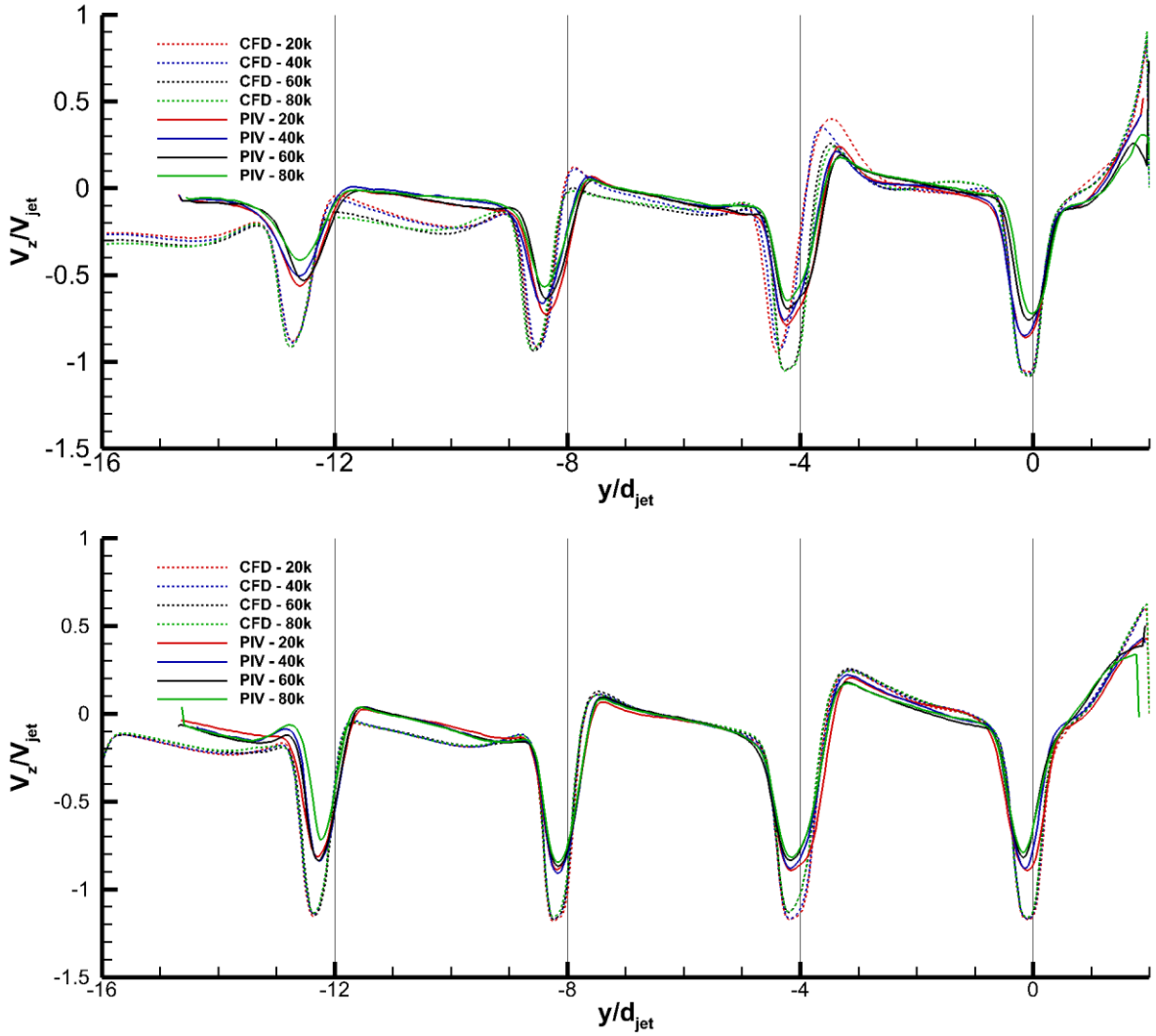

Figure 80: Axial velocity at wall normal distance z/d = 1.5:
H/d = 2.7 (top), H/d = 4 (bottom)

REFERENCES

Alvarez, J.; Calzada, P.; Krulic, G. (2008), "Heat Transfer and Flow Characteristics of a leading Edge Impingement Cooling System for Low Pressure Turbine Vanes", Proceedings of ASME Turbo Expo 2008: Power for Land, Sea and Air, GT2008-50142

ASME (2010), "Pressure Measurement, Instruments and Apparatus Supplement, Performance Test Codes", ASME PTC 19.2-2010

Brakmann, R. (2017), "Increasing Heat Transfer in Convective Cooling Systems with Optimized Surface Structures", University of Stuttgart, Dissertation

Bunker, R.; Metzger, D. (1990), "Local Heat Transfer in Internally Cooled Turbine Airfoil Leading Edge Regions: Part I – Impingement Cooling Without Film Coolant Extraction", Journal of Turbomachinery, Vol. 112, pp. 451-458

Calzada, P.; Alvarez, J. (2010), "Experimental Investigation on the Heat Transfer of a Leading Edge Impingement Cooling System for Low Pressure Turbine Vanes", Journal of Heat Transfer, Vol. 132, pp. 122202-1-8

Cengel, Y.; Boles, M. (2011), "Theromdaynamics An Engeineering Approach, Seventh Edition", Boston: McGraw-Hill

Coronaro, C; Fleischer, A.; Goldstein, R (1999), "Flow Visualization of a Round Jet Impinging on Cylindrical Surfaces", Experimental Thermal and Fluid Sciences, Vol. 20, pp. 66-78

Choi, M.; Yoo, H.; Yang, G.; Lee, J.; Sohn, D. (2000), "Measurement of Impingement Jet Flow and Heat Transfer on a Semi-Circular Concave Surface", International Journal of Heat and Mass Transfer, Vol. 43, pp. 1811-1822

Chupp, R.; Helms, H.; McFadden, P.; Brown, T (1969), "Evaluation of Internal Heat-Transfer Coefficients for Impingement-Cooled Turbine Airfoils", Journal of Aircrafts, Vol. 6, No. 3, pp. 203-208

Dano, B.; Liburdy, J.; Kanokjaruvijit, K. (2004), "Flow Characteristics and Heat Transfer Performances of a Semi-Confined Impinging Array of Jets: Effect of Nozzle Geometry", International Journal of Heat and Mass Transfer, Vol. 48, pp. 691-701

Elebiary, L.; Taslim, M. (2011), “Experimental/Numerical Crossover Jet Impingement in an Airfoil Leading-Edge Cooling Channel”, Proceedings of ASME Turbo Expo 2011, GT2011-46004

Elebiary, K.; Taslim, M. (2013), “Experimental/Numerical Crossover Jet Impingement in an Airfoil Leading-Edge Cooling Channel”, Journal of Turbomachinery, Vol. 135, pp. 011037-011037-12

Gau, C.; Chung, C. (1991), “Surface Curvature Effect on Slot-Air-Jet Impingement Cooling Flow and Heat Transfer Process”, Journal of Heat Transfer, Vol. 113, pp. 858-864

Gilard, V.; Brizzi, L. (2005), “Slot Jet Impingement on a Concave Curved Wall”, Journal of Fluids Engineering, Vol. 127, pp. 595-603

Han, B.; Goldstein, R. (2001), “Jet-Impingement Heat Transfer in Gas Turbine Systems”, Annals of the New York Academy of Sciences, Vol. 934, pp.147-161

Harmon, W.; Wright, L.; Crites, D.; Morris, M.; Riahi, A. (2015), “Combined Effects of Jet Plate Thickness and Fillet Radius on Leading Edge Jet Impingement with round and Racetrack Shaped Jets”, Proceedings of ASME Turbo Expo 2015: Turbine Technical Conference and Exposition, GT2015-43505

Holmén, V. (2012), “Methods of Vortex Identification”, Lund University, Thesis

Hossain, J.; Tran, L., Kapat, J. (2014), “An Experimental Study of Detailed Flow and heat Transfer Analysis in a Single Row Narrow impingement Channel”, Proceedings of ASME Turbo Expo 2014, GT2014-26498

Hryzak, P. (1978), “Heat Transfer from a Row of Jets Impinging on Concave Semi-Cylindrical Surface”, International Journal of Heat and Mass Transfer, Vol. 28, pp. 67-72

Hossain, J.; Fernandez, E.; Kapat, J. (2016), “A Detailed Experimental and Numerical Investigation of Flow Physics in a Single Row Narrow Impingement Channel Using PIV, LES, and RANS”, 52nd AIAA/SAE/ASEE Joint Propulsion Conference

Ibrahim, M.; Kochuparambil, B.; Ekkad, S.; Simon, T. (2005), “CFD for Jet Impingement Heat Transfer with Single Jets and Arrays”, Proceedings of ASME Turbo Expo 2005, GT2005-68341

Jia, R.; Rokni, M.; Sunden, B. (2002), “Numerical Assessment of Different Turbulence Models for Slot Jet Impingement on Flat and Concave Surfaces”, Proceedings of ASME Turbo Expo, DT-2002-30449

Jordan, C.; Wright, L.; Crites, D. (2012), “Effect of Impingement Supply Condition on Leading Edge Heat Transfer with Rounded Impinging Jets”, Proceedings of the ASME 2012 Summer Heat Transfer Conference, HT2012-58410

Jordan, C.; Wright, L.; Crites, D. (2013), “Impingement Heat Transfer Enhancement on a Cylindrical Leading Edge Model with Varying Jet Temperatures”, Journal of Turbomachinery, Vol. 135, pp. 031021-1-8

Jordan, C.; Wright, L.; Crites, D. (2016), “Impingement Heat Transfer on a Cylindrical, Concave Surface with Varying Jet Geometries”, Journal of Heat Transfer, Vol. 138, pp. 122202-1-10

Liu, Z.; Feng, Z.’ Song, L. (2010), “Numerical Study of Flow and Heat Transfer of Impingement Cooling on Model of Turbine Blade Leading Edge”, Proceedings of ASME Turbo Expo 2010: Power for Land, Sea and Air, GT2010-23711

Metzger, D.; Baltzer, R.; Jenkins, C. (1972), “Impingement Cooling Performance in Gas Turbine Airfoils Including Effects of Leading Edge Sharpness”, Journal of Engineering Power, Vol. 94, pp. 219-225

Metzger, D.; Bunker, R. (1990), “Local Heat Transfer in Internally Cooled Turbine Airfoil Leading Edge Regions: Part II – Impingement Cooling With Film Coolant Extraction”. Journal of Turbomachinery, Vol. 112, pp. 459-466

Penumadu, P.; Rao, A. (2017), “Numerical Investigations of Heat Transfer and Pressure Drop Characteristics in Multiple Jet Impingement System”, Applied Thermal Engineering, Vol. 110, pp.1511-1524

Ravelli, S.; Dobrowolski, L.; Bogard, D. (2010), “Evaluating the Effect of Internal Impingement Cooling on a Film Cooled Turbine Blade Leading Edge”, Proceedings of ASMER Turbo Expo 2010: Power for Land, Sea and Air, GT2010-23002

Sciacchitano, A.; Wieneke, B. (2016), “PIV Uncertainty Propogation”, Measurement Science and Technology, Vol. 27, 084006

Taslim, M.; Setayeshgar, L.; Spring, S. (2001), “An Experimental Evaluation of Advanced Leading Edge Impingement Cooling Concepts”, Journal of Turbomachinery, Vol. 123, pp. 147-153

Taslim, M.; Bakharto, K.; Liu, H. (2003), “Experimental and Numerical Investigation of Impingement on a Rib-Roughened Leading-Edge Wall”, Journal of Turbomachinery, Vol. 125, pp. 682-691

Taslim, M.; Bethka, D. (2009), “Experimental and Numerical Impingement Heat Transfer in an Airfoil Leading-Edge Cooling Channel with Cross-Flow”, Journal of Turbomachinery, Vol. 131, pp. 011021-1-7

Wang, N.; Chen, A.; Zhang, M.; Han, JC. (2018), “Turbine Blade Leading Edge Cooling with One Row of Normal or Tangential Impinging Jets”, Journal of Heat Transfer, Vol. 140, pp. 062201-1-10

Wieneke, B. (2017), “PIV Uncertainty Quantification and Beyond”, Delft University of Technology, Doctoral Thesis

Wright, L.; Han, JC. (2013), “Heat Transfer Enhancement for Turbine Blade Internal Cooling”, Proceedings of the ASME 2013 Heat Transfer Summer Conference, HT2013-17813

Yang, L.; Ren, J.; Jiang, H.; Ligrani, P. (2014), “Experimental and Numerical Investigation of Unsteady Impingement Cooling Within a Blade Leading Edge Passage”, International Journal of Heat and Mass Transfer, Vol. 71, pp. 54-68

Zhao, Q.; Chung, H.; Choi, S. Cho, H. (2016), “Effect of Guide Wall on Jet Impingement Cooling in Blade Leading Edge Channel”, Journal of Mechanical Science and Technology, Vol. 30, pp. 525-531